



universität  
wien

# MAGISTERARBEIT

Titel der Magisterarbeit

Structural analysis of galaxy clusters in X-rays

Verfasserin

Alexandra Weißmann Bakk. rer. nat.

angestrebter akademischer Grad

Magister der Naturwissenschaften (Mag. rer. nat.)

Wien, 2010

Studienkennzahl lt. Studienblatt: A 066 861

Studienrichtung lt. Studienblatt: Magisterstudium Astronomie

Betreuer: Univ.-Prof. Dipl.-Phys. Dr. Gerhard Hensler



# Contents

<b>1</b>	<b>Clusters of galaxies</b>	<b>5</b>
1.1	Introduction . . . . .	5
1.2	History . . . . .	7
1.3	Intracluster Medium (ICM) . . . . .	9
1.4	Mass estimates . . . . .	10
1.5	Substructure . . . . .	13
<b>2</b>	<b>XMM-Newton</b>	<b>15</b>
<b>3</b>	<b>Data</b>	<b>19</b>
3.1	Determining $r_{500}$ . . . . .	23
3.2	Luminosity . . . . .	23
3.3	Temperature . . . . .	24
3.4	Mass . . . . .	25
<b>4</b>	<b>X-ray Reduction and Analysis</b>	<b>27</b>
4.1	ODF preparation . . . . .	27
4.2	Cleaning . . . . .	28
4.3	Images and exposure maps . . . . .	28
4.4	Point Sources . . . . .	30
4.5	Background . . . . .	31
<b>5</b>	<b>Power ratios</b>	<b>33</b>
5.1	Error Estimation . . . . .	34
5.1.1	Simulated clusters . . . . .	35
5.1.2	Method of Böhringer et al. (2010) . . . . .	39
5.1.3	Bias . . . . .	41
5.1.4	Error estimation . . . . .	45
5.1.5	Method of Sanders (2006) - contbin . . . . .	48
5.1.6	Attempt to calibrate power ratios . . . . .	49
5.2	Dependence on aperture radius . . . . .	52
5.3	Dependence on total counts . . . . .	54
<b>6</b>	<b>Results</b>	<b>59</b>
6.1	Power ratios vs. cluster parameter . . . . .	59
6.2	Luminosity-Temperature and Luminosity-Mass relation . . . . .	64
6.3	Mean and $\sigma$ vs. cluster parameter . . . . .	69
6.4	Morphological classification . . . . .	72

6.4.1	Classification by Buote & Tsai (1996) - method . . . . .	72
6.4.2	Classification by Buote & Tsai (1996) - application to data . . . . .	74
6.4.3	Classification using mean and $\sigma$ . . . . .	76
6.5	Application for high-redshift cluster . . . . .	80
<b>Conclusions</b>		<b>81</b>
<b>Outlook</b>		<b>83</b>
<b>Bibliography</b>		<b>85</b>
<b>List of Figures</b>		<b>89</b>
<b>List of Tables</b>		<b>95</b>
<b>List of Abbreviations</b>		<b>97</b>
<b>Appendix</b>		<b>99</b>
<b>Abstract</b>		<b>111</b>
<b>Zusammenfassung</b>		<b>113</b>
<b>Acknowledgements</b>		<b>115</b>
<b>Curriculum Vitae</b>		<b>117</b>



# Chapter 1

## Clusters of galaxies

### 1.1 Introduction

The smallest gravitationally bound structures of galaxies are groups of galaxies. They have up to  $\sim 50$  members and a diameter of about 1 Mpc. The Milky Way itself belongs to a galaxy group called the Local group (Figure 1.1), which has about 35 members within the range of approx. 1 Mpc of the Milky Way. The most luminous galaxies in this group, which emit 90% of the total luminosity, are the Milky Way and M31. Other significant members are M33 and the Large and the Small Magellanic Clouds. In the Local group, but also in its neighbourhood, many smaller groups of galaxies can be found. It is believed that about 80% of all galaxies are part of smaller systems like groups or small clusters (Carroll & Ostlie 2006).

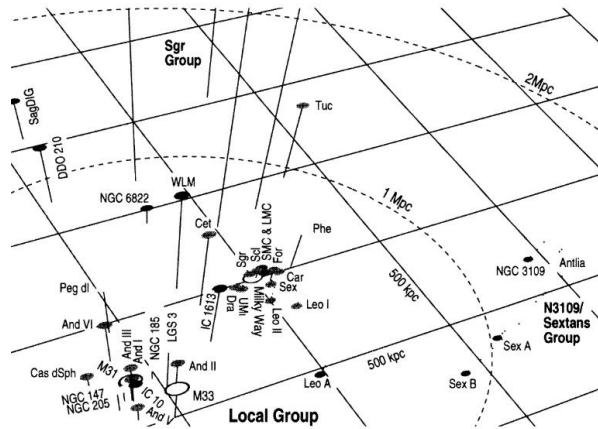


Figure 1.1: Local group of galaxies. Source: Grebel (2001).

The largest gravitationally bound structures in the Universe are clusters of galaxies. They contain all the building blocks of the Universe (baryonic and dark matter) and are key laboratories to study many astrophysical processes on large scales and to constrain cosmological parameters. The cluster mass ranges from  $10^{13}$  to  $10^{15} M_{\odot}$  and is dominated by dark matter (80-90% of total mass), while most of the baryons (80%) are found in a hot, fully ionized plasma, the intracluster medium (ICM). The optically visible part of a cluster, namely stars in galaxies, account only for a few % of its total mass (Schindler & Diaferio 2008).

Table 1.1: Characteristic parameters of a galaxy cluster

galaxy cluster	
size	$\sim \text{Mpc}$
total mass	$10^{13} - 10^{15} M_{\odot}$
mass fraction in DM	80-90%
mass fraction in ICM	10-20%
mass fraction in stars	few %
temperature	$10^7 - 10^8 \text{ K}$ (2-15 keV)
velocity dispersion	$\sim 1000 \text{ km/s}$
Intracluster Medium (ICM)	
luminosity $L_X$	$10^{43} - 10^{45} \text{ erg/s}$
density $n_e$	$10^{-4} - 10^{-1} \text{ cm}^{-3}$
metallicity $Z$	0.3

Galaxy clusters were first discovered through optical observations as concentrations of galaxies on the sky. Thus, they were named clusters of galaxies. However, in X-rays they have a different appearance (Figure 1.2), because the emission of thermal bremsstrahlung produced by the hot ICM is dominant.

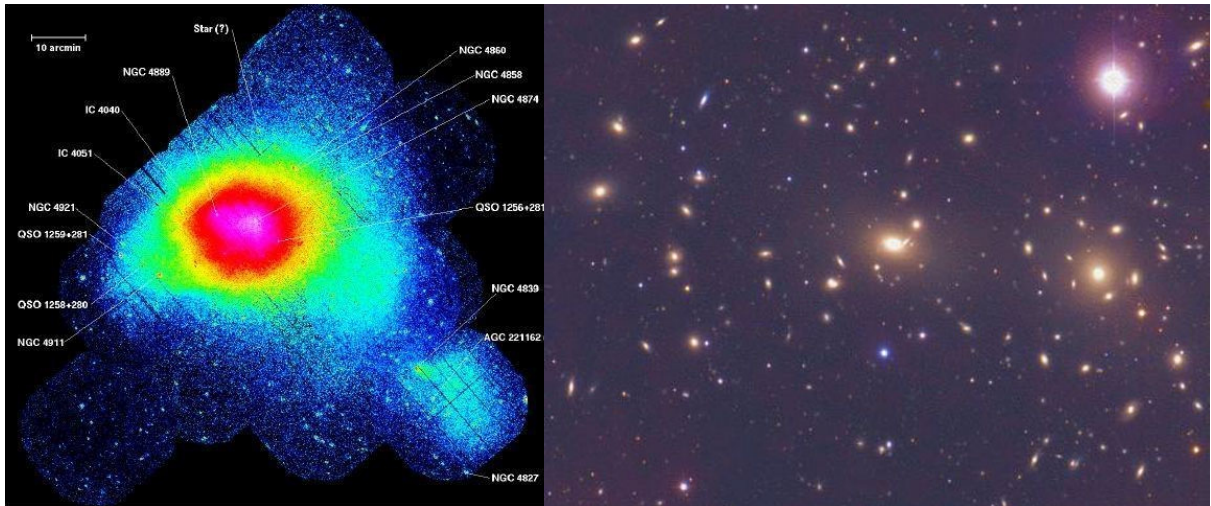


Figure 1.2: Optical (left) and XMM-Newton Image (right) of the Coma cluster of galaxies including point sources. Source: U. Briel/MPE (left); Snowden/MPE (right).

Clusters of galaxies are divided into poor and rich clusters, depending on their number of member galaxies. Poor clusters are systems of 50 to a few hundred galaxies, rich clusters contain thousand and more members. According to their morphology clusters are further classified as regular or irregular. Using optical observations a cluster with a peaked spherically symmetric galaxy distribution around its center is defined as regular. The Coma cluster (Figure 1.2) used to be the best example of a relaxed cluster. Recent studies however show significant structure on small and large scales. This rich cluster has a diameter of 6 Mpc and contains over thousand luminous and about 10 000 dwarf galaxies (small galaxies with up to several billion stars).

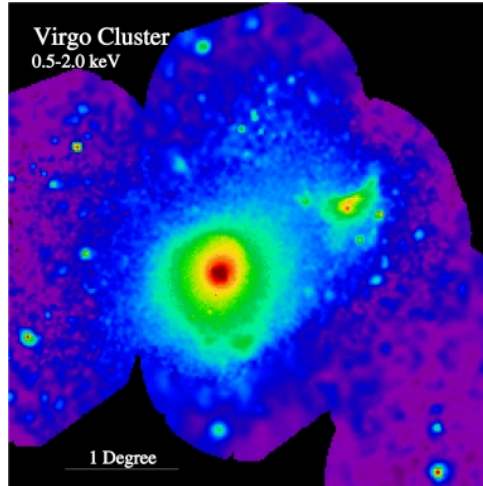


Figure 1.3: ROSAT Image of the Virgo cluster including point sources. Source: Snowden/MPE.

The Virgo cluster (Figure 1.3) is an irregular cluster. It hosts about 250 large and more than 2 000 small galaxies and thus can be classified as a poor cluster. The diameter is estimated to be around 3 Mpc. M87, a very large elliptical cD galaxy, is the largest and most luminous member of the Virgo Cluster.

### Dark matter

As already mentioned, the total mass of a galaxy cluster is dominated by dark matter. Dark matter is invisible, only gravitationally interacting matter, whose nature is not fully known yet. Navarro et al. (1995, 1996, 1997) introduce the most commonly used dark matter halo profile, the Navarro-Frenk-White (NFW) profile. This profile represents a universal density profile of dark matter halos and can be written as

$$\frac{\rho(r)}{\rho_{\text{crit}}} = \frac{\delta_c}{(r/r_s)(1 + r/r_s)^2} \quad (1.1)$$

$\rho_{\text{crit}} = 3H^2(z)/8\pi G$  is the critical density of the universe at redshift  $z$ ,  $H(z)$  the Hubble constant at this redshift and  $G$  the gravitational constant.  $r_s$  is the scale radius and  $\delta_c$  the characteristic density.

## 1.2 History

Clustering of galaxies is already known for a long time from optical observations. Already in 1784 Charles Messier mentioned the Virgo cluster in his work *Connaissance des Temps*. The first detailed studies of clusters of galaxies were performed by Wolf in the early 1900s. An outstanding discovery was made by Zwicky in the 1930s. Assuming that clusters are virialised and isolated systems, he calculated the total cluster mass, which was needed for the system to be gravitationally bound. The required mass was about 100 times the mass observed in galaxies. It is assumed now that the gravitational potential is dominated by dark matter and the ICM. Zwicky further suggested that the cluster mass could be measured through gravitational lensing - a method which did not become practical for the next few decades. Abell made extensive

observations and produced a catalogue of rich clusters of galaxies (Abell 1958). This catalogue was an important source of information for a long time.

Another interesting aspect of clusters of galaxies was found in 1966. X-ray emission was detected in the region of the galaxy M87, which is located close to the center of the Virgo cluster. Soon more X-ray sources around central galaxies of clusters were found. This suggested that all galaxy clusters are X-ray sources, but could only be confirmed after the first X-ray satellite was launched. Early observations were made with balloon- or rocket-borne detectors, but there was a need for sky surveys, which were impossible at that time. This changed with the launch of the Uhuru X-ray satellite in 1970 (Figure 1.4). An extensive sky survey was performed and the theory of clusters as X-ray sources was proven. Felten et al. (1966) correctly described the emission as thermal bremsstrahlung before Uhuru took off. After the launch, X-ray spectra were studied and many mechanisms of X-ray emission proposed and tested. In the end, the model of thermal bremsstrahlung indeed fitted the data the best.

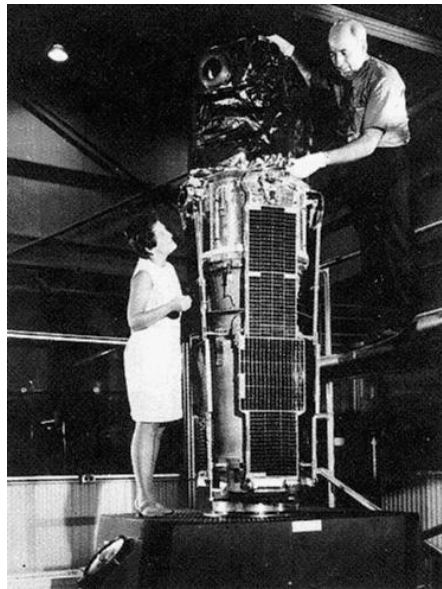


Figure 1.4: Uhuru satellite in preflight checks. Source: NASA.

Mitchell et al. (1976) found an emission line of highly ionised iron (7 keV) in the X-ray spectrum of the Perseus cluster. Later, emission lines of iron but also other heavy elements (so-called metals) were found in the spectra of many galaxy clusters.

The next steps in X-ray observations were made in the late 1970s and early 1980s with the launch of HEAO-1 (1977) and later with the EINSTEIN or HEAO-2 satellite (1978). EINSTEIN was the first fully imaging X-ray telescope in space. The detectors on-board those satellite observatories were more sensitive than all others before. Therefore, many new clusters and many new types of clusters, like poor compact clusters, were discovered. In the 1990s, with the launch of ROSAT (1990), CHANDRA (1999) and XMM-Newton (1999) satellites, the spectral resolution improved tremendously. While EINSTEIN had a maximum angular resolution of 5 arcseconds, with CHANDRA it became better than 1 arcsecond (Shore 2002). Thus structure within the clusters could now be detected and analysed.

### 1.3 Intracluster Medium (ICM)

Zwicky (1933, 1937) concluded that the optically visible mass was by far not enough to gravitationally bind the galaxies in a cluster (see section 1.4). Some of the missing mass was found by the first X-ray satellites and called intracluster medium. The rest is believed to be dark matter.

The X-ray band allows us to study the hot, fully ionized plasma, which is heated in the gravitational well of the cluster to temperatures between  $10^7$  and  $10^8$  K (about 2-15 keV). This plasma, which makes up 10-20% of the total mass, is located between the galaxies in a cluster and the source of the observed X-ray emission. The ICM is not concentrated around the individual cluster galaxies, but traces the gravitational potential of the cluster and provides valuable information about it. Typically, individual galaxies are not visible in an X-ray image of a cluster because the emission of the hot intracluster gas is dominant. This gas is heated to those high temperatures when the cluster forms, mostly through shock heating due to accretion. It has cooling times larger than the Hubble time. Only in the central regions, where the gas density is very high, the cooling time is short enough for the ICM to cool. Furthermore, it is an optically thin plasma, which makes it possible to study the entire cluster volume. The gas density distribution of the ICM can be described using a so-called isothermal  $\beta$  model (Cavaliere & Fusco-Femiano 1976, 1978)

$$\rho_g = \rho_{g,0} \left( 1 + \left( \frac{r}{r_c} \right)^2 \right)^{-3/2\beta} \quad (1.2)$$

where  $\rho_{g,0}$  is the central gas density,  $r_c$  the core radius and  $\beta$  a fitting parameter.  $\beta$  is  $\sim \frac{2}{3}$  and seems to decrease for poorer cluster (e.g. Finoguenov et al. 2001). The  $\beta$  model is based on a King profile (King 1962) and assumes that the ICM is isothermal and in hydrostatic equilibrium. The gas density distribution is characterized by equation 1.2, the X-ray emission is proportional to  $\rho_g(r)^2$ , which implies higher emission at higher gas densities. The X-ray surface brightness (Jones & Forman 1984) is then characterized by the following  $\beta$  profile

$$S \propto \left( 1 + \left( \frac{r}{r_c} \right)^2 \right)^{-3\beta + \frac{1}{2}} \quad (1.3)$$

The King profile overestimates the surface brightness of clusters in the outer parts. In addition, the  $\beta$  model underestimates the central surface brightness for cool-core clusters because of non-isothermality.

The main mechanism of this emission is thermal bremsstrahlung. At temperatures  $kT < 2$  keV line emission becomes dominant and provides valuable information about the hot gas. Thermal bremsstrahlung is a free-free emission process. It occurs when charged particles, like free electrons or ions, collide, are accelerated by the coulomb field and produce thermal continuum radiation (photons with different energies) in the X-ray wavelength range. On the other hand, line emission is a bound-bound emission process and produces lines in the spectrum. How the radiative cooling rate coefficient (emission) depends on temperature is shown in Figure 1.5 (left) for an optically thin plasma. In addition, the contributions of different elements to the cooling coefficient are indicated. Figure 1.5 (right) shows the combined RGS 1<sup>st</sup>- and 2<sup>nd</sup>-order spectrum of the core of the galaxy cluster Hydra A (Simionescu et al. 2009). The continuum due to thermal bremsstrahlung and the emission due to line emission of metals (e.g. Fe) is shown.

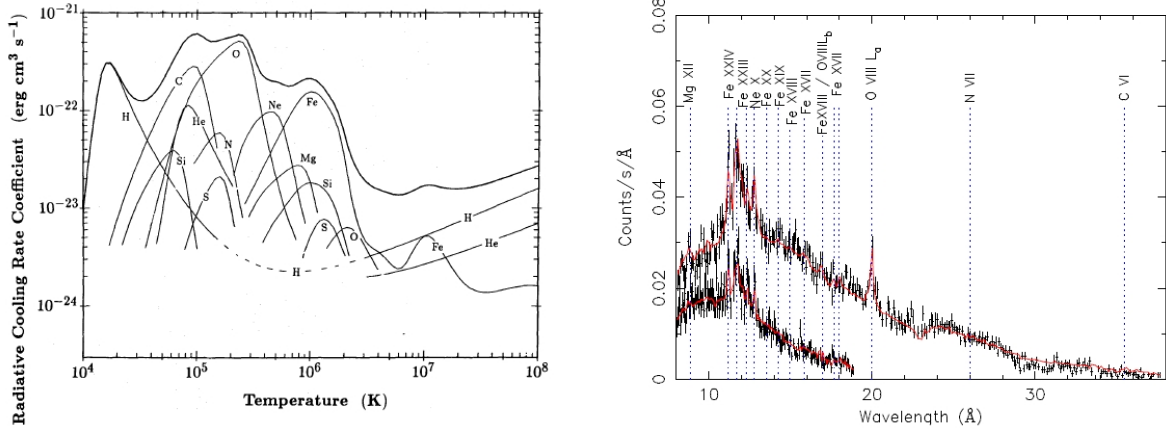


Figure 1.5: Radiative cooling rate coefficient as a function of temperature. Contribution of different elements to the radiative cooling coefficient (left). Combined RGS 1<sup>st</sup>- and 2<sup>nd</sup>-order spectrum of the core of the galaxy cluster Hydra A (right). Source: Böhringer & Hensler (1989) (left), Simionescu et al. (2009) (right).

The ICM contains 70-90% of the visible baryonic mass of clusters, including a certain amount of metals. Metals are produced in stars and released by supernovae ejecta to the interstellar medium (ISM). How they are transported from the ISM into the ICM is still not fully understood, however ram-pressure stripping and galactic winds are believed to play an important role in the enrichment of the ICM (Schindler & Diaferio 2008). Currently the metallicity is estimated to be on average 0.3 solar abundances. This abundance is measured by the strength of emission lines of metals, like e.g. Fe. As mentioned in section 1.2, the 7 keV emission line was the first to be found in the X-ray spectrum of clusters. From O up to Fe (7 keV complex) most elements are produced and transported by supernova explosions into the ISM and through other mechanisms into the ICM. During the explosion of a type Ia supernova large amounts of Fe, Ni, Si, S, Ar and Ca and only little of O, Ne and Mg are produced. Supernovae type II create predominantly O, Ne and Mg but also other  $\alpha$ -elements like Si, S, Fe or Ni (Werner et al. 2008).

## 1.4 Mass estimates

Estimating the mass of clusters of galaxies is very important for constraining cosmological parameters on the basis of the abundance of clusters above a certain mass limit. For clusters in hydrostatic equilibrium, the total mass is closely related to the temperature of the ICM and the depth of the potential well. In order to derive the mass, the gas density distribution  $\rho_g(r)$  and the temperature profile  $T(r)$  are needed. In this - ideal - case, equation 1.4 or 1.5 can be solved directly and the mass profile  $M(r)$  obtained

$$\frac{d \ln \rho_g}{d \ln r} + \frac{d \ln T}{d \ln r} = -2 \frac{T_\Phi(r)}{T} \quad (1.4)$$

$$M(r) = \frac{k_B T r}{G \mu m_p} \left( \frac{d \ln \rho_g}{d \ln r} + \frac{d \ln T}{d \ln r} \right) \quad (1.5)$$

where  $\rho_g(r)$  is the gas density distribution and  $k_B T_\Phi(r) = GM(r) \mu m_p / 2r$  the virial temperature of an isothermal sphere.

Unlike measuring luminosities, temperature profiles require high-quality data, because the counts (photons) are not just integrated over a specific radius, but they are distributed into different energy bins. In addition, X-ray surface brightness (in order to obtain the density profile (e.g. Croston et al. 2006)) and temperature profiles need to be deprojected, which requires assumptions like spherical symmetry. In cases, where it is not possible to measure temperature gradients accurate enough (e.g. high-redshift cluster), X-ray scaling relations are used. These relations connect X-ray properties with each other (e.g. Luminosity-Temperature, Temperature-Mass) and are calibrated using simulations or high-quality data (e.g. Pratt et al. 2009). Cluster masses cannot be measured directly for many objects but are often obtained using such relations. Therefore it is very important that the calibration is accurate. In the context of this work, we are especially interested whether substructure modifies scaling relations and their scatter. This can be due to merging, AGN interaction or shocks, which modify the temperature, luminosity or mass of a cluster. It is however not fully understood yet how important such effects are.

Another method uses the Sunyaev-Zeldovich (SZ) effect (Sunyaev & Zeldovich 1970, 1972), which quantifies the effect of the ICM on the cosmic microwave background (CMB). CMB photons are Compton-scattered by free electrons of the ICM, shifted to slightly higher energies and distort the CMB spectrum. The shape of the spectrum is characterized by the Compton parameter  $y$ ,

$$y = \int \frac{k_B T}{m_e c^2} n_e \sigma_T dl \quad (1.6)$$

where  $m_e$  is the electron mass,  $\sigma_T$  the Thomson cross-section and  $dl$  the integration over the line of sight.  $y$  is proportional to the probability that a photon which passes through the ICM will be Compton scattered and the typical amount of energy gain of a scattered photon. For cosmological purposes, the integrated Compton parameter  $Y$  is used

$$Y = \int y dA \propto \int n_e T dV \quad (1.7)$$

where  $A$  is the projected surface area,  $n_e$  the electron density of the ICM and  $V$  the cluster volume. The integrated distortion parameter  $Y$  gives the total thermal energy of the electrons which is the gas Mass  $M_g$  times the mass-weighted gas temperature. Therefore the total mass can be estimated from the calibrated  $Y - M$  relation (e.g. Zhang et al. 2008). This method is closely related to the method used in X-rays. The SZ-effect however uses the pressure directly, while in X-rays the temperature and density profiles needs to be deprojected first.

In optical observations, the cluster mass is derived using velocity dispersions. Radial velocities of the member galaxies are measured and a gaussian fitted to the distribution, obtaining a 1D-velocity dispersion of the cluster. The accuracy of this dispersion depends strongly on the number of galaxies measured. Zwicky (1933, 1937) found  $\sigma_{1D} \sim 700 \text{ km s}^{-1}$  for the Coma cluster and was the first to use this method to estimate the total mass. Assuming that clusters are isolated and virialised spherical systems, he used equation 1.8 to estimate the mass from the dispersion,

$$M = 3\sigma_{1D}^2 r_G / G \quad (1.8)$$

where  $\sigma_{1D}$  is the 1D velocity dispersion,  $r_G$  the cluster radius (“gravitational radius”) and  $G$  the gravitational constant. He concluded that the mass observed in galaxies is by far not enough to gravitationally bind the galaxies and found that the required mass is about 100 greater. This was the first indication of dark matter.

However most clusters are not in equilibrium and their shape differs from spherical symmetry. In such cases, mass estimation methods like X-ray scaling relations, based on velocity dispersions or the SZ effect are not always accurate. Methods which are not biased by this assumption, such as mass estimates using gravitational lensing or the caustic technique (Diaferio & Geller 1997) suffer from other problems. Intercalibration of all methods is therefore important.

Diaferio & Geller (1997) introduced a method called caustic technique. It is based on the redshift distribution of the member galaxies and uses the galaxy escape velocity from the potential well of the cluster. The cluster galaxies populate a very specific region in the redshift-radius diagram (velocity along the line of sight vs. projected distance from the cluster center). This region is enclosed by two lines called caustics. Half the distance of the two caustics,  $A(r)$ , is proportional to the escape velocity. Assuming spherical symmetry, the mass within a certain radius can be estimated by

$$M(< r) = \frac{1}{2G} \int_0^r A^2(x) dx \quad (1.9)$$

Using clusters as gravitational lenses of background galaxies for mass estimates of a cluster was first mentioned by Zwicky (1937). However, it was technically not possible to measure the small effects for a long time. Light from background sources is bent by the clusters' gravitational potential along the line of sight, revealing the distribution of dark matter. The deflection angle depends on the depth of the potential, hence on the cluster mass. For an axially symmetric cluster, the mass can be estimated by

$$M(< r) = \frac{rc^2}{4G} \alpha \quad (1.10)$$

where  $c$  is the speed of light and  $\alpha$  the deflection angle. Two main approaches are used to determine the dark matter distribution: strong and weak gravitational lensing. If the object acting as a lense is massive and close enough, multiple images of a single background source can be observed. More massive lenses produce more features like multiple images or arcs. In most cases the lensing object is not massive enough. The background sources are distorted and magnified, but the signal is weak and hard to measure. This is called weak lensing and provides a powerful tool to probe the distribution of mass and to constrain cosmological parameters. Measuring the weak-lensing distortion of an individual background galaxy is not possible, because the initial shape of the galaxy is not known. Therefore, the shear distortion of a field of background galaxies is measured. However, assumptions like the way the mass is distributed are required. In addition, gravitational lensing is sensitive to all the mass along the line of sight.

In order to get accurate mass estimates, different methods are combined. Scaling relations can be refined by comparing mass estimates based on weak lensing, X-ray and optical data. In addition, the dynamical state and the shape of the cluster should be known as accurate as possible to correct for the assumptions of equilibrium or spherical symmetry.



## 1.5 Substructure

Substructure is defined as multiple peaks in the surface density of the galaxy distribution in the optical and X-ray surface brightness. According to the current structure formation scenario, clusters form from density fluctuations and grow through merging and interaction with other clusters and groups of galaxies. Such an event is seen as substructure in an X-ray image, as multiple peaks in the surface brightness distribution (e.g. bullet cluster, Figure 1.6), disturbed clusters (e.g. Figure 1.7 left, middle) or through AGN interaction (Figure 1.7 right). At earlier stages of the universe, merging events of clusters were more common, because the environment was denser. At the present epoch, clusters should be - on average - more relaxed and dynamically more evolved than at earlier times. Therefore the amount of substructure should increase with redshift and clusters in the local universe should appear as relaxed. The increase of substructure with redshift was indeed observed in the sample of Jeltema et al. (2008). However, even at lower redshifts ongoing merging events in some clusters are observed. The number of such disturbed clusters depends on the detection method, the threshold for the degree of substructure and the wavelength, but is estimated to be about 40-70% for X-ray observations (Mohr et al. 1995; Jones & Forman 1999; Schuecker et al. 2001; Kolokotronis et al. 2001). X-ray observations are less sensitive to foreground and background objects, because X-ray luminosity is proportional to  $\rho^2$ . In addition, X-ray surveys are only limited by the effective area of the detector and the integration time. Optical studies depend on the number of galaxies observed and the method by which galaxies are classified as members.



Figure 1.6: Composite Image of galaxy cluster 1E 0657-56, also known as the "bullet cluster". In the optical wavelength individual galaxies and stars are seen (white). The ICM of the merging clusters can be seen as two red clouds, while the dark matter distribution is displayed in blue. While the ICM clouds are interacting, the dark matter halos pass by undisturbed. Source: X-ray: NASA/CXC/CfA/M.Markevitch et al.; Optical: NASA/STScI, Magellan/U.Arizona/D.Clowe et al.; Lensing Map: NASA/STScI, ESO WFI, Magellan/U.Arizona/D.Clowe et al.

Numerous methods are known to parametrise substructure, including center shifts, ellipticity and the method which is used in this work, power ratios (section 5). Measuring a clusters ellipticity is very common (e.g. McMillan et al. 1989; Plionis 2002), but not a good indicator for a clusters dynamical state, because relaxed and disturbed clusters can have significant ellipticities. Mohr et al. (1993) introduced the center shift method. It is based on the displacement of the

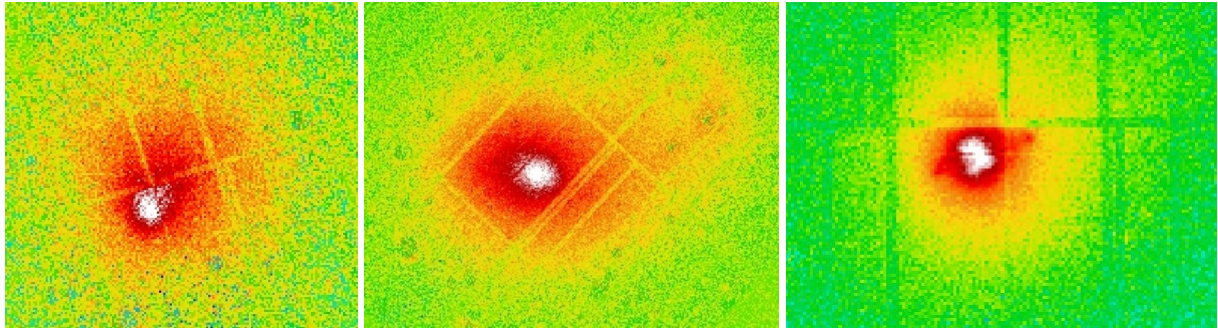


Figure 1.7: Examples of disturbed cluster morphologies. A665 (left), A3921 (middle), Cygnus A (right).

centroid in different radii. The shift of the centroid is sensitive to asymmetries and increases with increasing amount of substructure. It is however not clear yet, if and how center shifts relate to the dynamical state of the cluster. Our modified power ratio method is more suitable for this task and will be described in more detail in section 5.

Jones & Forman (1991) used EINSTEIN data and defined several morphologies: e.g. single symmetric peak, complex (multiple structure), double and primary with small secondary. Those four morphologies were later used by Buote & Tsai (1996), which will be discussed in section 6.4.2. In the 1990s using ROSAT observations, quantitative analysis of X-ray images was possible and it was established that clusters show substructure. The resolution was limited, but clusters which were thought to be relaxed, suddenly appeared to have substructure e.g. infalling subclusters. Abell 2256 is such a cluster. Fabricant et al. (1989) performed an optical and X-ray (IPC EINSTEIN) study on this cluster. They concluded that this cluster could experience the infall of a smaller cluster using galaxy velocities. This was not visible in the galaxy distribution or the X-ray images taken by Einstein. Two years later, Briel et al. (1991) confirmed the existence of a merger event using ROSAT PSPC observations. In the next few years, numerous thought to be relaxed clusters were identified as disturbed using ROSAT observations. This was an important cornerstone in the understanding of structure formation, because it showed that the formation and evolution of clusters is not finished yet.

The presence of substructure indicates deviation from hydrostatic equilibrium and dynamical youth. As discussed in section 1.4, the assumption of equilibrium is crucial for many mass estimation methods. Therefore it is very important to estimate the deviation from hydrostatic equilibrium by measuring the amount of substructure. The final goal resides in a relation of one or a number of parameters describing the substructure and the deviation from equilibrium. Such a relation needs to be calibrated, which is not trivial to accomplish and needs accurate knowledge of the dynamical state of the cluster. The aim of this study is to describe substructure in a quantitative way without a calibrated relation. Most interesting in this context is the distribution of the amount and the kind of substructure in a statistical representative sample. During the whole study, the standard  $\Lambda$ CDM cosmology was used:  $H_0=70$ ,  $\Omega_\Lambda=0.73$ ,  $\Omega_M=0.27$ .

## Chapter 2

# XMM-Newton

All observations used in this work were conducted using instruments on-board the XMM-Newton satellite. In order to be able to reduce the obtained data, it is important to know the characteristics of these instruments. They will be discussed in this section.

XMM-Newton (X-ray Multi-Mirror) was launched on 10<sup>th</sup> December 1999 by ESA from Kourou, French Guinea. With its 3.8 tons XMM-Newton is the biggest X-ray observatory built by ESA and hosts three X-ray telescopes with 58 high-precision concentric mirrors each. With such a large collecting area, XMM-Newton can make deeper spectro-imaging observations than any X-ray observatory before. It contains six advanced scientific instruments: three EPIC Cameras (EPIC pn and two EPIC MOS), two RGS (Reflection Grating Spectrometer) and an Optical Monitor. EPIC stands for European Photon Imaging Camera and is available as MOS and as pn CCD, which operate in the range 1-120 Å (about 12-0.1 keV). Apart from imaging, the EPICs can also be used for moderate resolution spectroscopy.

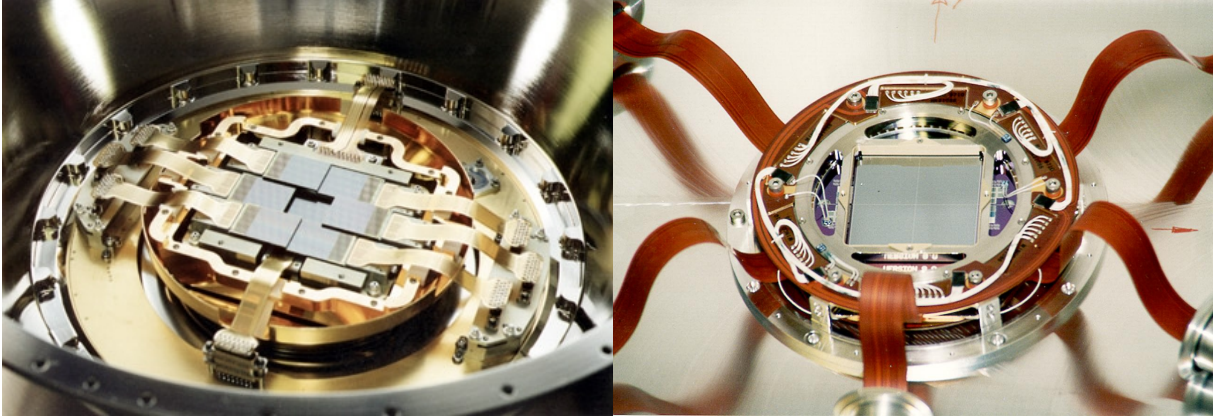


Figure 2.1: CCDs of the MOS (left) and pn camera (right). Source: ESA.

The two MOS detectors are metal oxide semi-conductor CCD arrays (Figure 2.1) and can be found behind the X-ray telescopes which are connected to the RGS. Thus, the incoming flux of each telescope is divided between the MOS detector (about 44%) and RGS (Figure 2.2 left). Each MOS detector consists of seven mosaic CCDs, while the one in the center is the Tracking CCD (Figure 2.3 left and middle). This Tracking CCD is located in the focal point of the X-ray telescope while the other six are found approximately on the curved focal plane of the MOS



camera. The imaging area of all seven CCDs is 28.4 arcminutes or 600 x 600 pixel. Each pixel is 40 x 40 micron wide and covers 1.1 x 1.1 arcseconds on the FOV. In order to correct for chip gaps, the two MOS detectors are rotated by 90° to each other. After March 2005, CCD6 on MOS1 cannot be operated anymore, because of an impact of a micrometeorite on the focal plane. This CCD was switched off and does not deliver scientific information anymore (Figure 2.3 left).

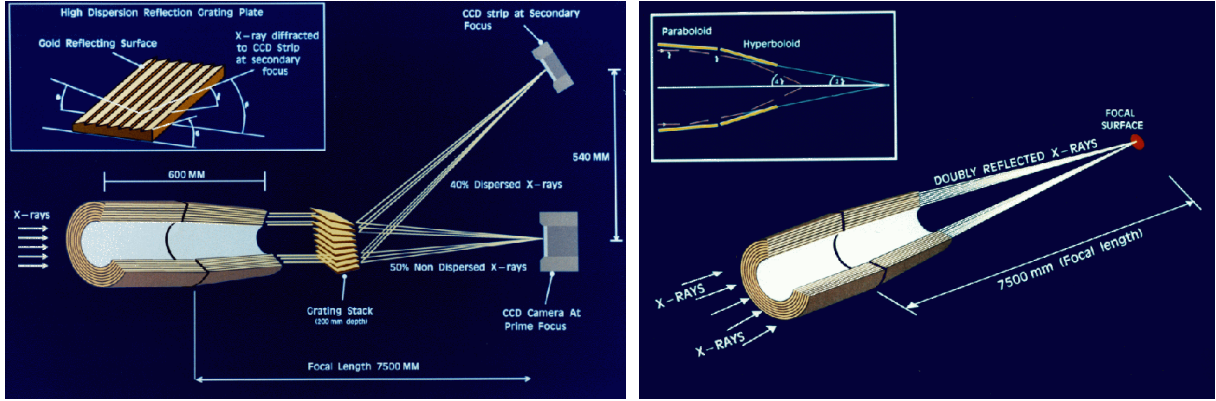


Figure 2.2: Light path with the MOS (left) and pn (right) camera in focus (not to scale). Source: XMM-Newton Users Handbook V2.7.

The pn camera is located behind the third X-ray telescope and receives all of the incoming flux (Figure 2.2 right). The detector consists of 12 pn-CCDs on one wafer (Figure 2.1), which are divided in four Quadrants with three CCDs with 200 x 64 pixels each (Figure 2.3 right). The pixel size is 150 x 150 micron and covers about 4.1 arcseconds. The total imaging area is 6 x 6 cm which is about 97% of the telescopes field of view.

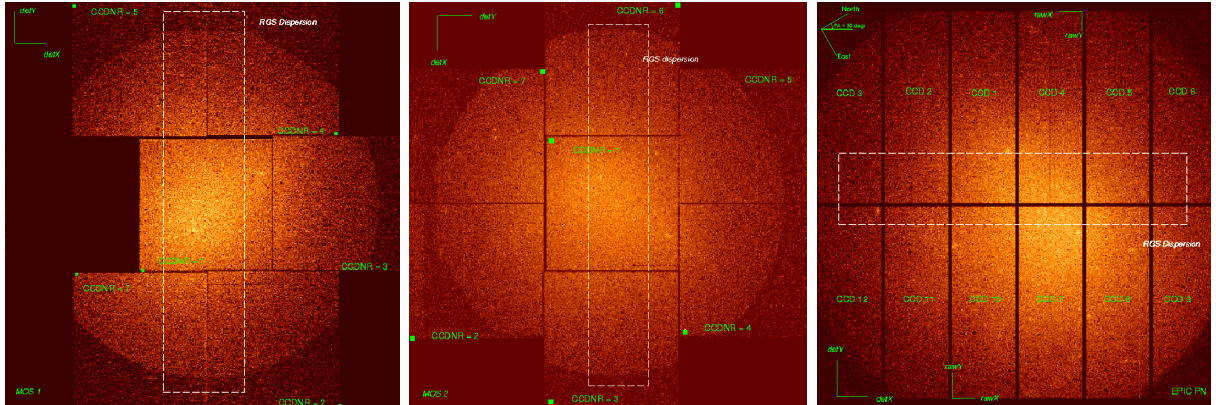


Figure 2.3: Geometry of the MOS1 (left), MOS2 (middle) and pn (right) CCDs. Source: XMM-Newton Users Handbook V2.7.

Apart from the arrangement of the CCDs (Figure 2.3) and the light path (Figure 2.2), EPIC MOS and pn differ in the quantum efficiency, the sensitivity and the read-out time. Each pixel column in the pn camera has its own read-out node, which reduces the read-out time compared to MOS. The difference in the quantum efficiencies is due to the fact that the MOS CCDs are front-illuminated while those of pn are back-illuminated. The MOS has a limited energy trans-

mission at the high energy band (0.2-10 keV), while the pn can measure photons up to 15 keV (Figure 2.4). When using the EPIC cameras, one can choose between three operation modes: full frame (FF)/extended full frame (EFF), partial window and timing mode. For this work all observation were made in the FF or EFF mode. In this mode all pixels and therefore the full FOV is read-out. The two EPIC MOS can only be operated in the full frame mode, while pn can also be operated in EFF mode (longer integration time). An overview of the characteristics of the EPIC MOS and pn instruments is provided in Table 2.1.

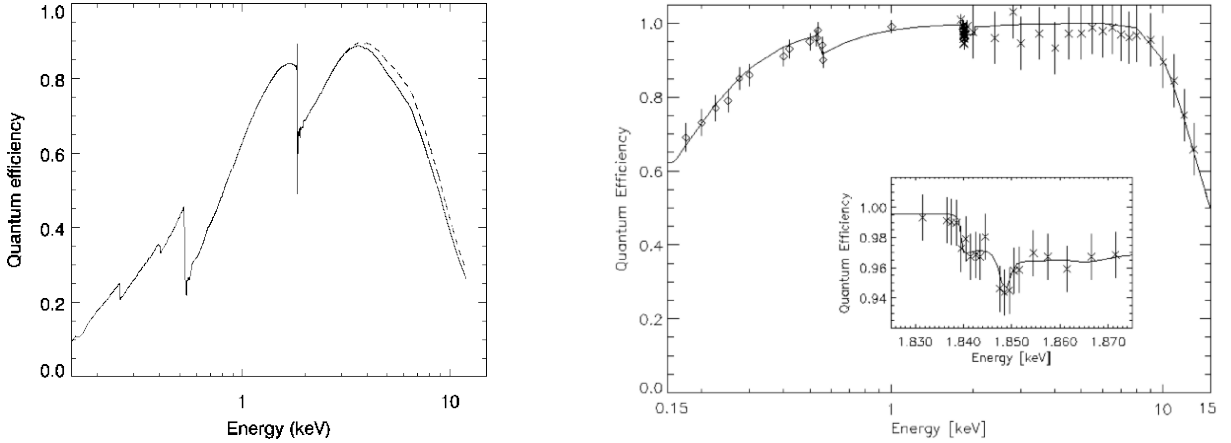


Figure 2.4: Quantum efficiency of the MOS CCDs (left) and pn detector (right). Source: ESA (left) and Strüder et al. (2001) (right).

Table 2.1: Characteristics of the EPIC Instruments EPIC MOS (column 1) and EPIC pn (column 2). Source: XMM-Newton Users Handbook V2.7.

	EPIC MOS (1)	EPIC pn (2)
Bandpass	0.15-12 keV	0.15-15 keV
Orbital target vis.	5-135 ks	5-135 ks
Sensitivity	$\sim 10\text{-}14 \text{ erg s}^{-1} \text{ cm}^{-2}$	$\sim 10\text{-}14 \text{ erg s}^{-1} \text{ cm}^{-2}$
Field of view (FOV)	30'	30'
PSF (FWHM/HEW)(8)	5"/14"	6"/15"
Pixel size	40 $\mu\text{m}$ (1.1")	150 $\mu\text{m}$ (4.1")
Timing resolution	1.75 ms	0.03 ms
Spectral resolution	$\sim 70 \text{ eV}$	$\sim 80 \text{ eV}$

In addition to the imaging X-ray detectors the observatory is equipped with two Reflection Grating Spectrometers (RGS) and an Optical Monitor which is co-aligned with the X-ray telescope. All six instruments can be operated simultaneously. Information and images are taken from the XMM-Newton homepage<sup>1</sup>.

<sup>1</sup>XMM-Newton Documentation EPIC (ESA), [http://xmm.esac.esa.int/external/xmm\\_user\\_support/documentation/technical/EPIC/index.shtml](http://xmm.esac.esa.int/external/xmm_user_support/documentation/technical/EPIC/index.shtml)



## Chapter 3

# Data

The 80 clusters chosen for this analysis are picked from different catalogues and contain all 31 REXCESS (Böhringer et al. 2007) and many LoCuSS clusters (Zhang et al. 2008). All other clusters are taken from the following sources: Buote & Tsai (1996); Arnaud et al. (2005); Zhang et al. (2006); Snowden et al. (2008). All REXCESS clusters are used, but not all clusters from the other subsamples. Most clusters are excluded because their  $r_{500}$  is too big and does not fit on the detector. Thus it is not possible to obtain accurate results within apertures of  $r_{500}$  for these clusters.

The REXCESS sample was created as a morphologically unbiased sample (more details are discussed below). These 31 clusters were studied before in detail (e.g. Böhringer et al. 2010; Pratt et al. 2009; Croston et al. 2006). We use the REXCESS clusters to test our methods and increase the number to yield better statistics. It now spans a wide range in redshift, temperature and luminosity, which can be seen in Figure 3.1 and 3.2. The overlaid filled histogram represents the REXCESS subsample. Some clusters appear in more than one subsample, which allows us to check the consistency of the data analysis by different authors. The observations were obtained with EPIC MOS1, EPIC MOS2 and EPIC pn on-board the XMM-Newton satellite and taken from the XMM-Newton Archive. We take different temperature and  $r_{500}$  determination methods into account and favour REXCESS and LoCuSS information. More detailed information about the sample including power ratios can be found in Tables 6.5-6.10 in the Appendix. In the following sections we outline how  $r_{500}$ , luminosities, temperatures and masses are obtained.

In order to display the high quality of this sample, we provide a histogram showing the total number of counts after soft-proton cleaning (see section 4.2) and combination of all three detectors in Figure 3.3 (left). The mean of the sample is indicated by the solid line. Figure 3.3 (right) shows the total exposure time after cleaning and combination of all three detectors. Again, the mean of the sample is indicated by the solid line. The high total number of counts and the long exposure times show that this sample consists of observations with high signal-to-noise ratios. In addition, the sample of 80 clusters is comparable to the REXCESS subsample regarding the data quality (counts and exposure time). All observations used are single-exposures. For most clusters however multiple exposures are available. A combination of several observations would increase the total counts and total exposure times even more and thus the quality of the sample.

The cumulative histogram in Figure 3.4 shows that 90% of all clusters have more than  $10^4$  counts. The REXCESS cut is at 30 000 counts and includes more than 65% of the full sample. This again underlines the consistency of the two samples regarding total counts.

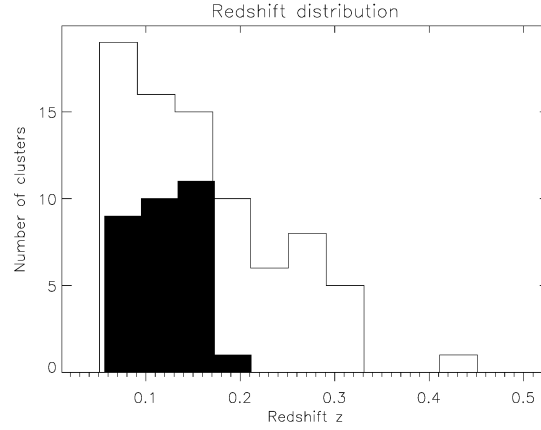


Figure 3.1: Redshift distribution of the sample. The overlaid filled histogram represents the REXCESS subsample.

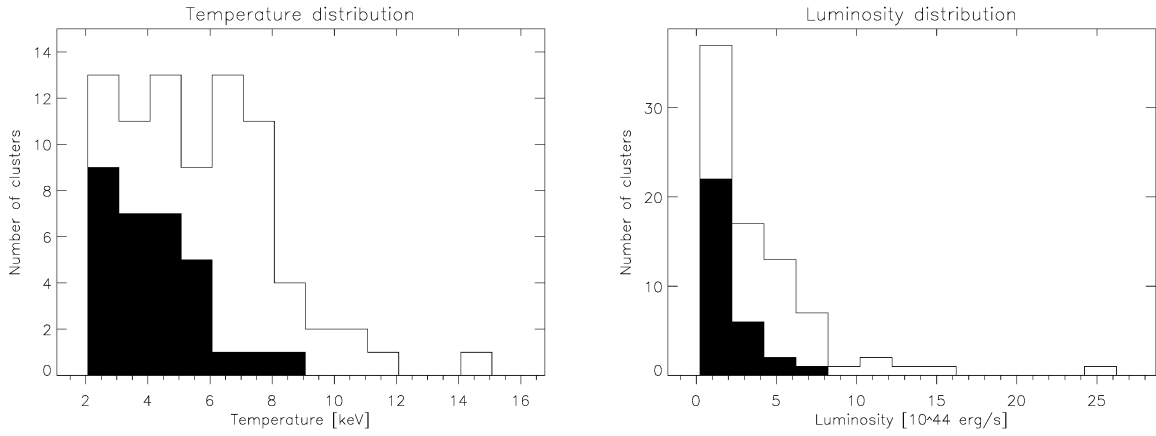


Figure 3.2: Temperature (left) and luminosity (right) distribution of the sample. The overlaid filled polygons represent the REXCESS subsample.

Images and exposure maps are obtained using EPIC pn and MOS data from XMM-Newton, which we reduced ourselves (details in section 4) with the XMM-Newton SAS Software version 9.0.0. Temperatures are taken from the literature for all sub-samples, mass (within  $r_{500}$ ) just for three subsamples (Arnaud et al. 2005; Zhang et al. 2006, 2008). The radius  $r_{500}$  is not available for all subsamples, but can be estimated from  $T_X$  (Details see section 3.1). We obtain luminosities for the energy band 0.5-2 keV using XSPEC 11.3.2. Details can be found in section 3.2. An overview of the references for each cluster can be found in Table 2.1.



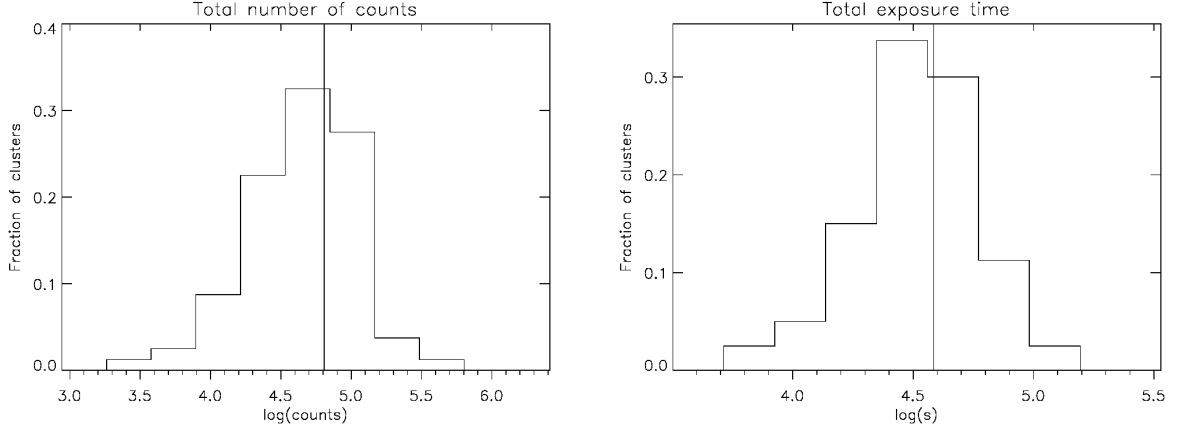


Figure 3.3: Histogram of counts (left), Histogram of total exposure time (right). The solid line indicates the mean values of the sample of 80 clusters.

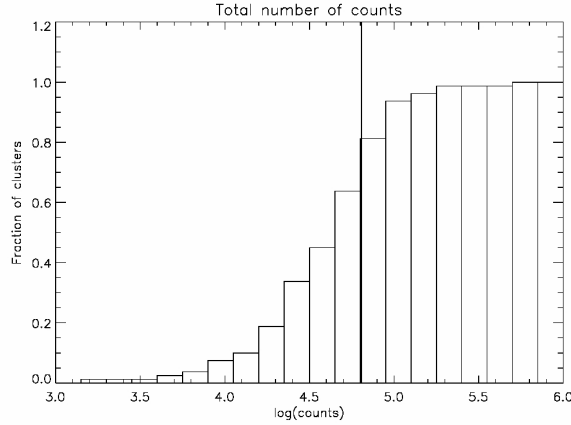


Figure 3.4: Cumulative histogram of the total number of counts after cleaning and combination of all three detectors. The solid line indicates the mean of the sample.

### Consistency of the sample

As mentioned above, several small samples are merged into our final sample of 80 cluster. When doing so, the consistency of the obtained sample needs to be investigated. Otherwise results can be biased by e.g. the different methods to obtain temperatures, which are presented in the literature. Figure 3.5 shows that the subsamples extend the REXCESS sample to higher mass, temperature and luminosity.

In addition, some clusters are part of more than one subsample. This allows us to compare e.g. temperatures obtained by different authors in different ways for the same cluster. Figure 3.6 shows the comparison between REXCESS and LoCuSS temperatures. They match very well.

### REXCESS

REXCESS is the Representative X-ray Cluster Substructure Survey. Böhringer et al. (2007) selected 31 clusters from the REFLEX Cluster Survey (updated catalogue: Böhringer et al. 2004) between redshifts  $z=0.055$  and  $z=0.183$  with X-ray luminosities  $L_X \geq 0.4 \cdot 10^{44} h_{70}^{-2} \text{ erg s}^{-1}$  in

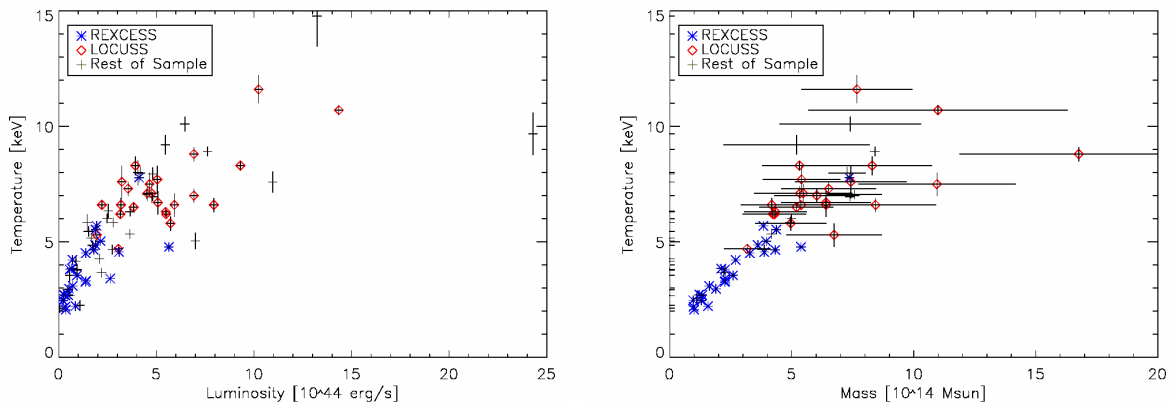


Figure 3.5: Comparison of different subsamples. blue asterisk: REXCESS, red diamonds: LoCuSS, black crosses: Rest of the sample. L-T relation (left), L-M relation (right).

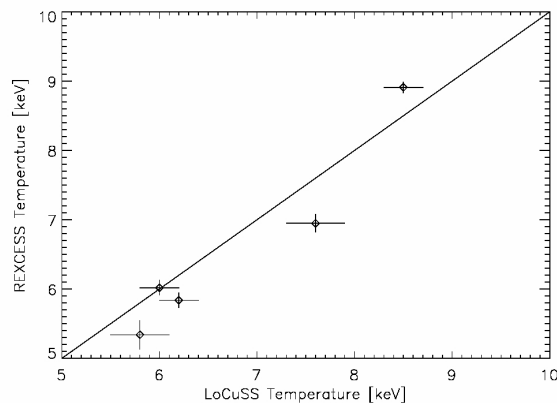


Figure 3.6: Comparison between REXCESS and LoCuSS temperatures

the 0.1-2.4 keV energy band and obtained high-quality observations for them. The aim of this survey was to create a morphologically and dynamically unbiased sample, which was selected mainly by X-ray luminosity and restricted to redshifts  $z \leq 2$ . In addition, the  $L_X$  distribution fully probes the luminosity function. With this sample statistical cluster studies (e.g. substructure, mass) are possible. For this study it is an ideal reference sample to find out whether the sample of 80 clusters is morphologically biased or not. In Figure 3.1 and 3.2, the REXCESS sample is represented by the overplotted filled polygons.

Pratt et al. (2009) studied and calibrated X-ray luminosity scaling relations for REXCESS. The gas entropy and its relation to the gas mass fraction were examined by Pratt et al. (2010). Arnaud et al. (2009) published a universal galaxy cluster pressure profile and a newly calibrated  $Y_{SZ} - M_{500}$  relation. The relationship between the brightest cluster galaxies (BCGs) and their host clusters, including cool core properties, was examined by Haarsma et al. (2010). And most recently, Böhringer et al. (2010) investigated the statistics of substructure in clusters and compared their results to numerical simulations.

### 3.1 Determining $r_{500}$

The radius  $r_{500}$  marks the radius where the cluster density is 500 times the mean density of the universe. The power ratio method picks up large-scale fluctuations in the gravitational potential of a cluster, which means that only large-scale structure within a certain radius can be measured by power ratios. In addition, high quality data is needed to obtain accurate results, which can only be done for radii like  $r_{500}$  or smaller for which highly significant X-ray emission is observed. The radius  $r_{500}$  is thus the best compromise between high quality data and a radius which characterises the cluster in a global way. The values of  $r_{500}$  are provided for the following subsamples: REXCESS (Pratt et al. 2009) and LoCuSS (Zhang et al. 2008). For all other clusters we use the relation presented by Arnaud et al. (2005):

$$r_{500} [\text{Mpc}] = 1.104 \cdot h_{70}^{-1} (kT/5\text{keV})^{0.57} [\Omega_M(1+z)^3 + \Omega_\Lambda]^{-1/2} \quad (3.1)$$

During the whole study, we use the standard  $\Lambda$ CDM cosmology:  $H_0=70$ ,  $\Omega_\Lambda=0.73$ ,  $\Omega_M=0.27$ .

In order to use these values as aperture radii, they need to be transformed from Mpc into arcminutes. Therefore a factor which relates kpc and arcseconds (kpc/“) for each redshift is calculated using Ned Wright’s Javascript Cosmological Calculator<sup>1</sup> and the appropriate cosmology. The desired result in arcminutes is obtained using

$$r_{500} ['] = \frac{r_{500} [\text{Mpc}]}{\text{kpc}/'' \cdot 60/1000} \quad (3.2)$$

### 3.2 Luminosity

For most subsamples X-ray luminosities are provided by the original authors. However, they were obtained in different energy bands, aperture sizes and by different methods. We therefore derive X-ray luminosities for the 0.5-2 keV band ourselves. This is done using the following procedure.

First, surface brightness profiles are extracted from the exposure corrected images. For simplicity we use only the pn detector, because this detector is the most sensitive. We compare the obtained luminosities with those given by the literature (e.g. for REXCESS) and find a good agreement. A model background which is obtained during the data reduction (section 4.5) is subtracted and background-corrected surface brightness profiles are obtained. In addition, a growth curve is created by integrating the count rate (number of counts per second) over radial bins of the image, yielding count rates at different radii from the cluster center (e.g.  $r_{500}$ ). Selecting the appropriate outer radius, the total source counts of the image are obtained. In order to derive luminosities, we extract the integrated count rate within  $r_{500}$  of the pn growth curve. This radius is chosen to be consistent with the aperture radius  $r_{500}$  used in the power ratios analysis and  $M_{500}$  masses given in the literature.

In the next step, the X-ray spectral fitting package XSPEC<sup>2</sup> v11.3.2 is used. A simulated cluster spectrum is created using the MEKAL (Mewe-Kaastra-Liedahl) model provided by the XSPEC. This model calculates an emission spectrum (including thermal bremsstrahlung and line emission) of hot diffuse gas with given parameters. In our case, we provide the cluster temperature,

<sup>1</sup><http://www.astro.ucla.edu/~wright/CosmoCalc.html>

<sup>2</sup><http://heasarc.nasa.gov/docs/xanadu/xspec/index.html>

redshift, hydrogen column density ( $N_{\text{H}}$ , taken from the literature) and metallicity and simulate a spectrum. Count rates and luminosities in the 0.5-2 keV energy band are calculated from the model. We obtain a scaling factor luminosity/count rate using the simulated count rate and luminosity. We use this factor to scale the real count rate and to generate a luminosity for the observation itself. Obtained luminosities can be found in Table 6.8 in the Appendix. The listed errors are propagated from the errors on the count rates.

### 3.3 Temperature

X-ray temperatures are obtained by fitting a model (e.g. MEKAL) to the observed spectrum and thus spectroscopic temperatures. Global cluster temperatures can be defined in different ways. Various authors use different conventions and sometimes propose more than one kind of temperature. The sample consists of six subsamples and temperatures were obtained in different ways. An overview is given in Table 3.1, where the flag "used" indicates which of the provided temperatures is used for the analysis.

Table 3.1: Overview of methods to obtain temperatures. Columns: (1) Cluster name; (2) Extraction area in which temperature is obtained; (3) "used" indicates which of the provided temperatures is used for the analysis.

Sample (1)	Extraction area (2)	Flag (3)
Zhang et al. (2008)	T [0.2-0.5 $r_{500}$ ]	used
Zhang et al. (2006)	T [0.1-0.5 $r_{500}$ ]	used
Snowden et al. (2008)	profiles provided - T [ $r_{500}$ ]	used
Arnaud et al. (2005)	T [0.1-0.5 $r_{200}$ ]	used
Buote & Tsai (1996)	individual publications - T [ $r_{500}$ ]	used
Pratt et al. (2009)	T [ $r < r_{500}$ ]	used
Pratt et al. (2009)	T [0.15-1 $r_{500}$ ]	
Pratt et al. (2009)	T [0.15-0.75 $r_{500}$ ]	

Figure 3.7 shows a comparison of the three spectroscopic temperatures provided by Pratt et al. (2009). The two histograms display the difference in temperature with respect to the used temperature  $r < r_{500}$ :  $(T - T_{\text{used}})/T_{\text{used}} \cdot 100$ . The difference in the values are mostly less than 10%, except for four cases: RXCJ2014.8-2430 ( $\sim 20\%$ ), RXCJ0958.3-1103 ( $\sim 18\%$ ), RXCJ1311.4-0120 ( $\sim 8\%$ ) and RXCJ2234.5-3744 ( $\sim 11\%$ ).

Since the different ways to define global cluster temperatures are inhomogeneous, we want to make sure that they do not introduce any bias in our results. Therefore, we compare temperatures of clusters which are present in more than one subsample. The mean difference between the three temperatures provided by Pratt et al. (2009) is less than 5%.

No single temperature values but profiles are provided for the Snowden et al. (2008) subsample. For those clusters we perform a fit with a sixth-order polynomial and extract the temperature at  $r_{500}$ . Errors are propagated from the errors of the data points and the fitting parameters. We cross-check this for clusters which appear in different subsamples and find consistent results.

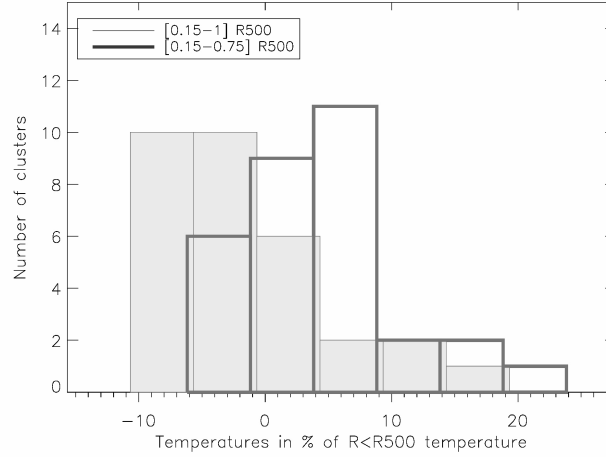


Figure 3.7: Comparison between the three temperature provided by Pratt et al. (2009). The histograms show  $(T - T_{\text{used}})/T_{\text{used}} \cdot 100$ . Filled histogram (thin line):  $[0.15-1] r_{500}$ . Thick line:  $[0.15-0.75] r_{500}$ .

### 3.4 Mass

$M_{500}$  masses are provided only for four subsamples: Zhang et al. (2008, 2006); Arnaud et al. (2005) and Pratt et al. (2010).  $M_{500}$  is the total mass within the radius  $r_{500}$ . As with temperatures, different mass estimation methods were used. We compare the given masses for 14 clusters which appear in several subsamples and find a mean difference of 5% to the used values.



## Chapter 4

# X-ray Reduction and Analysis

This section describes the main steps in the reduction and analysis of X-ray data taken with XMM-Newton using the XMM-Newton Science Analysis Software (SAS) version 9.0.0. This includes the preparation and cleaning of raw data files from flares, the creation of images and exposure maps and the source detection process. After the exclusion of point sources, the images and exposure maps are used to derive power ratios and luminosities in the different energy bands.

The SAS tasks are implemented in a data reduction pipeline created and provided by Hans Böhringer and Rene Fassbender, MPE (Fassbender 2008). We modify some modules (e.g. improve point source cutting) and adjust them to the energy bands used for this work. More detailed information on the SAS tasks can be found in the XMM-SAS Documentation<sup>1</sup> or the XMM-Newton SAS Cookbook<sup>2</sup>.

### 4.1 ODF preparation

Information from each XMM-Newton observation is stored in a so-called ODF (Observation Data File). Each observation and therefore each ODF has its own unique Observation ID (OB-SID). An ODF contains raw and uncalibrated data of all instruments used, information about the calibration and satellite attitude files.

ODFs for each cluster of the sample are downloaded from the XMM-Newton Science Archive<sup>3</sup> and stored in unique directories (Clustername/ODF/) for further use. Each directory contains a few 100 MB of raw and uncalibrated data. Calibration information about the instruments (e.g. EPIC response files) is available online<sup>4</sup> and called Current Calibration Files (CCF). The SAS task *cifbuild* creates a CIF (CCF Index File) from the ODF data and the calibration files (CCF), which contain all calibration information needed. *odfingest* extracts all information from the instruments' housekeeping files and from the calibration database and creates a summary of the observation which is appended to an ODF summary file. The tasks *emchain* for MOS and *epchain* for pn generate e.g. calibrated photon event lists, bad pixel lists or background light curves. The generated files are distributed into different directories (pn, MOS, AUX - auxiliary), their headers read and information (Object, Coordinates, Instrument, Filters, Submode etc.) extracted for further use.

---

<sup>1</sup>[http://xmm.esa.int/external/xmm\\_user\\_support/documentation/sas\\_usg/USG/](http://xmm.esa.int/external/xmm_user_support/documentation/sas_usg/USG/)

<sup>2</sup>XMM-SAS Cookbook, <http://heasarc.gsfc.nasa.gov/docs/xmm/abc/>

<sup>3</sup>XMM-Newton Science Archive, <http://xmm.esac.esa.int/xsa/index.shtml>

<sup>4</sup>XMM-Newton Calibration Information, [http://xmm2.esac.esa.int/external/xmm\\_sw\\_cal/calib/index.shtml](http://xmm2.esac.esa.int/external/xmm_sw_cal/calib/index.shtml)

## 4.2 Cleaning

The EPIC background consists of three main components which are due to photons (Cosmic X-ray Background), particles (soft proton flares and interaction with the detector) and electronic detector noise and will be discussed in 4.5. Electronic detector noise is corrected on-board the X-ray satellite and does not appear in the science data.

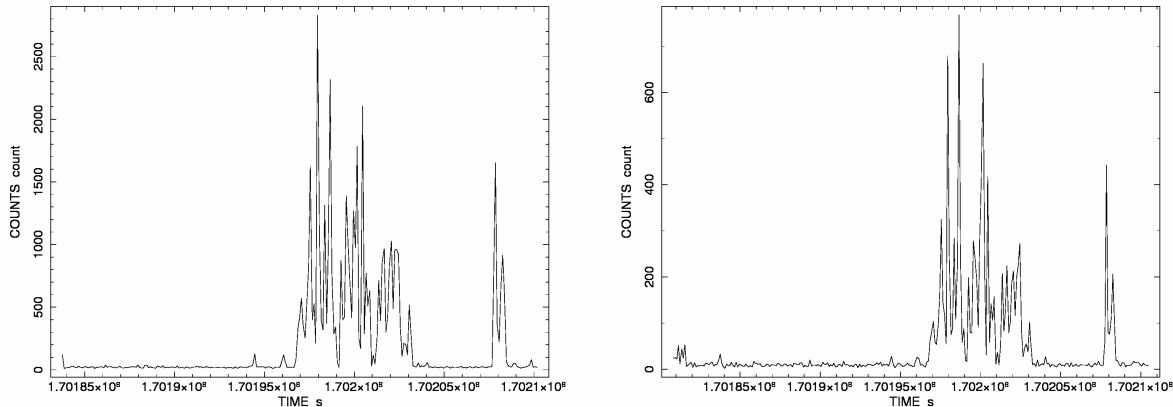


Figure 4.1: 100 second-binned pn (left) and MOS1 (right) light curve in the hard X-ray band at 12-14 keV.

Observation periods containing soft proton flares are removed from the event lists during two cleaning stages. In order to identify flares, light curves in the hard (12-14 keV for pn, 10-12 keV for MOS) and soft (0.3-10 keV) energy band are created using the task *evselect*. In the hard band light curve flare periods are easily visible above the flat quiescent background (Figure 4.1), which is determined using count-level histograms. Flaring periods are removed (Figure 4.3 left) and Good time intervals (GTI) determined. GTIs are defined as observation periods with background levels less than three standard deviations above the quiescent level. In the second cleaning stage, the remaining flares are identified and removed using the soft band light curve. The applied method is the same as for the hard band. After both flare cleaning stages, the light curve consists of GTIs and periods which were removed (Figure 4.3 right). The decrease in effective exposure time needs to be taken into account for further analysis.

The flare cleaning needs to be done for each observation and detector independently because of the different sensitivity of MOS and pn. However, the sensitivity throughout one CCD detector is not constant either. The brightness of an image decreases towards the edge of the chip. The mirrors are not as efficient at focusing off-axis photons as on-axis photons and the sensitivity decreases with increasing off-axis angle. To correct for this so-called vignetting, a weight column is added to each event list using the SAS task *evigweight*.

## 4.3 Images and exposure maps

From cleaned event lists, images and exposure maps can be created using the tasks *evselect* and *eeexpmap*. These tasks allow to generate science products (images and exposure maps) in customized energy bands. In addition, keywords for e.g. corrections for vignetting can be set. For this work we choose the 0.5-2 keV: It is the standard band for cluster X-ray analysis because it yields the highest signal-to-noise ratio.



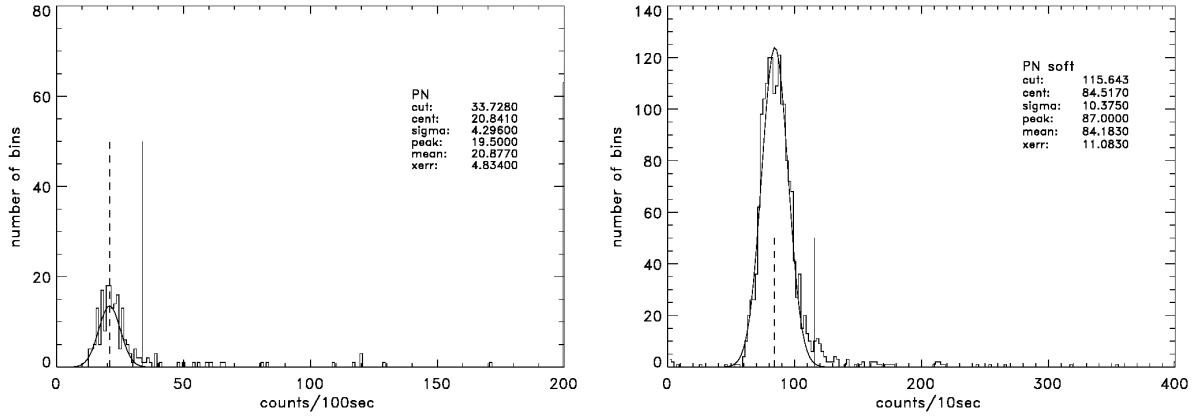


Figure 4.2: Count-level histograms after the first (left) and second (right) cleaning stage in the hard (left) and soft (right) X-ray band.

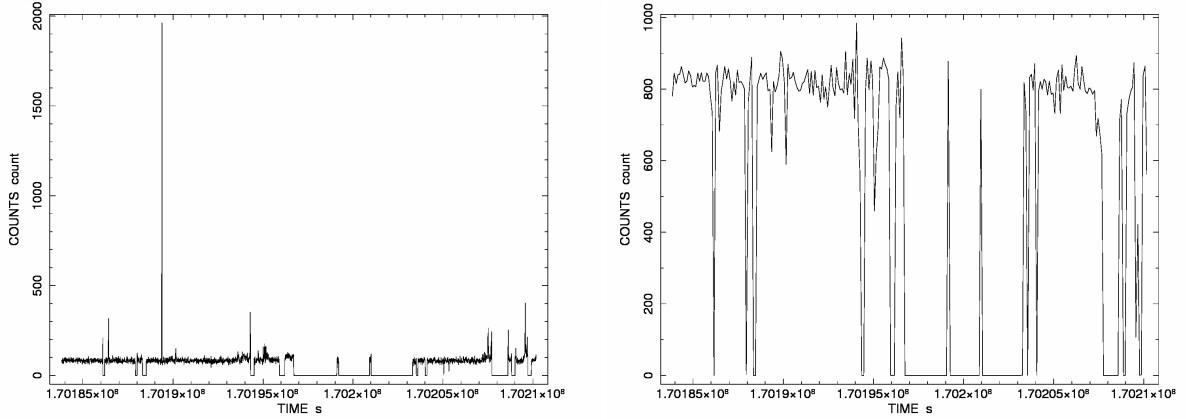


Figure 4.3: Result of the first cleaning stage: 10 second-binned pn light curve (left). Final result after both cleaning stages: 100 second-binned pn light curve (right).

Exposure maps are used to convert a raw count image into an sensitivity-corrected image in flux units. It can be compared to a flat-field used in optical observations. An exposure map contains the effective exposure time for each pixel and corrects for the varying sensitivity across the EPIC detectors and e.g. hot pixels. The EPIC pn detector does not close its shutter during read-out and contaminates the data. Read-out can take up to 6% of the frame time. Events which occur during this read-out phase are called out-of-time (OoT) events. They are included in the event list because they cannot be distinguished from events during the regular observation time. OoT events can cause smeared stripes on the image in the read-out direction. If the observed source is located in such a stripe, a major contamination is caused. The fraction of OoT events depends on the imaging mode (Extended Full Frame or Full Frame) and is either 2.3% or 6.3%. We create so-called OoT event files to correct for this. These OoT events are subtracted from the raw image data to create the final pn images.

The final science products of all three detectors are combined to increase the photon statistic. The MOS1 and MOS2 images and exposure maps can be added directly. Due to the different sensitivity of the MOS and the pn detector, a scaling factor ( $\sim 3.3$ ) is applied to the combined

MOS science frames before adding the pn images and exposure maps. The results are a combined image, a combined exposure map and an exposure corrected flux map.

## 4.4 Point Sources

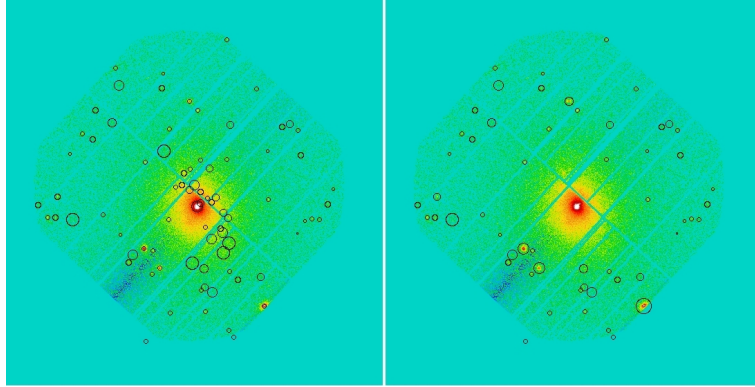


Figure 4.4: EPIC pn image including point sources selected by *ewavelet* and *ewavdetect* (left) and after visual inspection (right).

The removal of point sources is a very important step in the process of reducing X-ray data, especially for structural analysis. All objects on the image which are not originating from the ICM of the cluster are considered contaminating (point) sources, even if they are extended foreground galaxies. Big or close point sources can be brighter than the cluster and need to be removed. The point source removal cannot be done fully automatic, but needs optical inspection in order to assure that only real point sources and not e.g. the cluster center are cut out. In the first step, point sources are detected using the combined image of all detectors and the SAS tasks *ewavelet* and *ewavdetect*. A source list is generated which contains source positions, count rates and an indication of the source extent. This source list is transformed into a region file and can be examined in combination with the combined image by programs like *ds9*. However, *ewavdetect* classifies all surface brightness peaks as point sources, including the center of the cluster or regions near chip gaps. A visual inspection with *ds9* is needed. Incorrectly identified sources are removed from the source list, the size of others is adjusted and new region files are created. This procedure needs to be done with the outermost care to avoid incorrect classification of substructures and point sources. Whenever the distinction between substructure and point sources is unclear, we use additional information, including CHANDRA observations, NED information and previous published discussions of the cluster.

Detected sources are removed from the images and exposure maps and refilled using the CIAO<sup>5</sup> task *dmfilth*. This procedure replaces the counts inside the selected area and refills it with an average value determined from the region around the sources. Previously, the point sources are cut out of background-subtracted images. This method has some drawbacks, which are clearly visible during visual inspection. If this process however is done for each detector individually, the areas are refilled more smoothly and hardly visible in the final combined images and exposure maps.

<sup>5</sup>CHANDRA Interactive Analysis of Observations software package: <http://cxc.harvard.edu/ciao/>

## 4.5 Background

After removing the point sources from the combined images, all remaining background components need to be removed from the science frames. Therefore, the background models (Figure 4.5) of all three detectors are combined (including scaling for different sensitivity in pn and MOS) and subtracted from the point-source cleaned frames. The obtained combined images (Figure 4.6) and exposure maps are the final science products and can be used for our analysis.

The EPIC background consists of three main components which are due to photons (mainly Cosmic X-ray Background), particles (soft proton flares and particle interaction with the detector) and electronic detector noise, which was already removed on-board the X-ray satellite.

Noise caused by photons can be divided into two energy ranges. Photons in the hard X-ray range are due to the X-ray background (e.g. AGNs), single reflections from outside FOV and in the case of EPIC pn also to OoT events. The soft X-ray background is mainly due to X-ray emission from galactic foreground sources (Local Bubble, Galactic Disk,...), but like the hard X-ray background, also due to extragalactic sources, single reflections from outside the FOV and OoT events. The background caused by photons is variable over the sky but fairly constant with time.

The particle background consists of soft proton flares, a quiescent particle flux and the internal, cosmic-ray induced, background. The internal background is caused by interaction of cosmic rays with the detectors CCDs and is not constant with time. Flares due to soft, solar protons were already discussed in section 4.2.

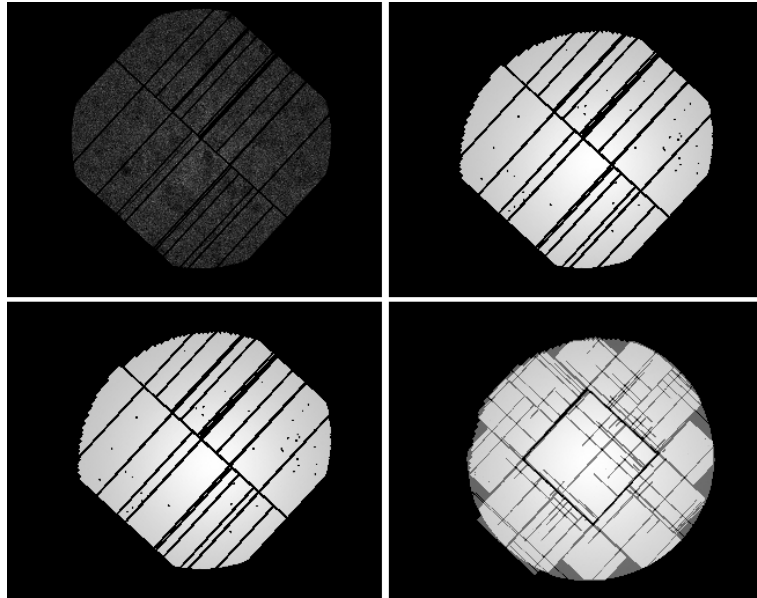


Figure 4.5: Background models. Top panel: EPIC pn (left), MOS1 (right). Bottom panel: MOS2 (left), Combination of all three detectors (right).

The last background component is caused by electronic noise. It includes bright pixels or columns, read-out noise and to some extent dark current, which can be neglected. Apart from bright pixels or columns, this component can be assumed constant.

Further details on the different background components can be found on the XMM-SAS web page and the XMM-Newton EPIC Background Jump Page<sup>6</sup>, which is maintained by Andy Read.

Flares are already removed at the beginning of the data reduction, however all other background components need to be addressed. In order to do so two methods to estimate the background are combined. If the source does not cover the whole detector, the background information is extracted from the detector itself, which is mostly not the case for the observations used here. Therefore, Blank Sky event files are used, which are provided at the XMM-Newton Homepage and were created using stacked pointed observations. These event files are recast onto the sky in order to adjust the background to the orientation of the target and images for each detector in the selected energy ranges are produced. Using the task *emask*, the science frame and the exposure map, a mask image of the blank sky image is created, which excludes e.g. chip gaps. This mask is needed for the next step, where a model of the background for each detector is created and chip gaps or source point regions need to be excluded. The SAS task *espinemap* then creates a model background using all the above mentioned frames. For this process, vignettted and unvignettted exposure maps need to be provided. This is due to the fact that the instrumental component is unvignettted because the particles do not go through the mirrors, while the X-ray background is vignettted. Thus when adding the background components each one gets a different scaling factor.

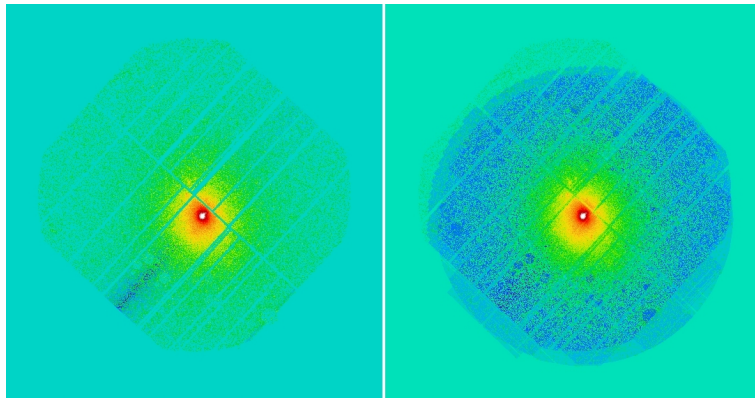


Figure 4.6: Point source corrected pn image (left) and combined image of all three detectors (right).

---

<sup>6</sup>EPIC Background, <http://www.star.le.ac.uk/~amr30/BG/BGTable.html>

## Chapter 5

# Power ratios

Quantifying structure in a cluster and estimating to which degree the cluster is disturbed, is very important to obtain accurate mass estimates, classify clusters correctly and investigate the relation between substructure and physical properties. One of the most promising methods to do so, is the power ratio method, which was introduced by Buote & Tsai (1995). Its aim is to parametrise the amount of substructure on different scales, which is related to the dynamical state of a cluster. While using this method, the large-scale structure distribution which dominates the global dynamical state is of interest. Single galaxies or small groups are not visible in the X-ray image and are thus not picked up by this method. Buote & Tsai (1995) claim that different optically distinguished morphologies (e.g. single-component, widely separated bimodal or multi-component clusters) can be differentiated.

The method is based on a 2D multipole expansion of the clusters gravitational potential using the surface mass density distribution. In X-rays the surface brightness distribution is used. Each term in the multipole expansion (power) is related to fluctuations in the gravitational potential and therefore also to the dynamical state of a cluster. The powers are calculated within a certain aperture radius (e.g.  $r_{500}$ ) and are sensitive to symmetries and asymmetries on different scales.

The 2D multipole expansion of the two-dimensional gravitational potential can be written as

$$\psi(R, \phi) = -2Ga_0 \ln \frac{1}{R} - 2G \sum_{m=1}^{\infty} \frac{1}{mR^m} (a_m \cos(m\phi) + b_m \sin(m\phi)) \quad (5.1)$$

where  $a_m$  and  $b_m$  are

$$a_m(R) = \int_{R' \leq R} \sum (\vec{x}') (R')^m \cos(m\phi') d^2 x' \quad (5.2)$$

$$b_m(R) = \int_{R' \leq R} \sum (\vec{x}') (R')^m \sin(m\phi') d^2 x' \quad (5.3)$$

while  $\vec{x}' = (R', \phi')$  and  $\sum$  represents the surface mass density (Buote & Tsai 1995). The powers are calculated by integrating the magnitude of  $\psi_m$ . The  $m$ th term in the multipole expansion of the potential is given for a circular aperture with radius  $R$  by

$$P_m(R) = \frac{1}{2\pi} \int_0^{2\pi} \psi_m(R, \phi) \psi_m(R, \phi) d\phi \quad (5.4)$$

Ignoring factors of  $2G$ , this relates to

$$P_0 = [a_0 \ln(R)]^2 \quad (5.5)$$

and

$$P_m = \frac{1}{2m^2 R^{2m}} (a_m^2 + b_m^2) \quad (5.6)$$

The projected mass density cannot be observed detailed enough. Therefore the X-ray surface brightness is used instead of the projected surface mass density, assuming that the X-ray surface brightness distribution follows the mass distribution closely. The power ratios are thus derived from a pseudo-potential. Buote & Tsai (1995) argue that although the X-ray emission is proportional to  $\rho_g^2$  and thus an increase in the gas density would increase the X-ray emission more than an increase in the mass density, the potential is dominated by dark matter and not by the ICM. Thus they conclude that the X-ray surface brightness is equally suited to obtain power ratios. In addition, it shows the same qualitative structure as the projected mass density.

In order to obtain powers which are independent of the X-ray luminosity, they are normalized by the zeroth-order moment (flux) and thus called power ratios. This allows a direct comparison of clusters with different X-ray brightness.  $P_0$ , the monopole, represents the flux.  $P_1$  and  $P_2$  represent dipole and quadrupole,  $P_3$  and  $P_4$  can be associated with hexapole and octopole moments. In general, even moments are sensitive to ellipticity or structure on the same scales (e.g. a bimodal cluster with two equal sized subclusters), while odd moments trace asymmetry. Previous studies established that  $P_3/P_0$  is the best indicator for asymmetry and thus structure in the ICM. It is therefore our primary substructure measure in our further analysis. The power ratios  $P_2/P_0$  and  $P_4/P_0$  are closely correlated ( $P_4$  is more sensitive to smaller scales than  $P_2$ ). Another characteristic of this method is the fact that it weights structure which is close to the aperture size more than such closer to the cluster center. This causes a dependence on the aperture radius (see section 5.2). For an ideal, spherical symmetric cluster, all power ratios would vanish, no matter which aperture size is used. However, we are dealing with real observations which contain photon noise. Therefore also apparently relaxed clusters will yield a small, but non-zero signal. This issue will be treated in section 5.1.3.

In this study, we are only interested in the lower-order power ratios  $P_2/P_0$ ,  $P_3/P_0$  and  $P_4/P_0$ . Higher power ratios would describe more complex structure on smaller scales, but the higher the order of the power ratio the lower the signal to noise ratio is likely to become. We choose 10 aperture radii ( $0.1-1 r_{500}$ ), which are centred around the brightest pixel in the central region. If not stated otherwise, power ratios and bias are obtained within an aperture radius of  $r_{500}$ . The power ratios for the 80 clusters are given in Table 6.9 in the Appendix.

## 5.1 Error Estimation

Observational data is never ideal. One limitation of the data, which has to be considered in the data reduction process, is shot noise. It is due to the finite number of photons reaching the mirrors, modifies the power ratio measurement and gives inaccurate results. Fortunately, it is a Poisson process and decreases with increasing number of photons. It is therefore very important to estimate the bias (difference between real and spuriously detected amount of structure) introduced by shot noise and its error, especially when dealing with low-count observations (e.g. below  $\sim 30\,000$  counts, see section 5.3).

The first step in estimating the bias and its error is to create several simulated clusters. For simulated cluster images, all parameters of the cluster are known, including the real amount of substructure. This allows a detailed analysis of the proposed bias- and error-estimation methods, which is performed in the following section. Such an analysis is not possible with real observations, because the amount of shot noise is unknown. In simulations, we can vary the amount of total counts and thus the influence of photon noise. In addition, we can test under which conditions the method gives reliable results.

The power ratio method is applied to clusters since 1995 (Buote & Tsai 1995), but the influence of photon noise on the measured power ratios is still not fully understood. Attempts to quantify the bias have been made in the past (e.g. Böhringer et al. 2010; Jeltama et al. 2005), however a fully verified and tested solution for the problem has not been presented yet. In the following sections, we investigate the difference (bias) between the ideal model and the exact same cluster with shot noise added to find out above which threshold a signal is significant. After discussing how the models are created, we test the method introduced by Böhringer et al. (2010) to estimate the bias and the measurement error.

### 5.1.1 Simulated clusters

In order to create simulated cluster images, up to four elliptical  $\beta$  models are added using the *kinging* task from the *zhtools*<sup>1</sup> package. We choose different models, including two spherical symmetric (A, B), one extremely elliptical (C) and two models with multiple surface brightness peaks (D, E). Those five models are created to estimate the bias due to photon noise. They do not resemble any particular real cluster and are created to bracket the range of the observed P3/P0. In addition, simulation F and H are chosen to have roughly the P3/P0 as real clusters and are modelled after A115 (F) and A1775 (H). Figure 5.3 shows the observed (left panels), the modelled ideal (middle panels) and a poissonised (noisy) cluster (right panels) for simulation H (top panel) and F (bottom panel). The aim is not to create perfect representations of these two given clusters but to get realistic looking clusters with realistic power ratios. Simulation H has a moderate amount of structure, while simulation F is a very structured cluster.

Figure 5.1 shows the ideal images without any photon noise for simulation A-E. Power ratios obtained using these images are called e.g.  $(P3/P0)_{\text{ideal}}$  and yield the clusters real power ratios due to its structure only and not due to shot noise or other sources of contamination. Figure 5.2 shows exactly the same simulated clusters (A-E) as Figure 5.1, but with Poisson noise added. Poissonised images are created using the *zhtools* task *poisson*. These cases correspond to real observations, which are biased by shot noise. The aperture radius is chosen to be 66 pixels for simulation A-E, but is increased to 100 pixels for simulation F and H, since 100 pixels is the average size of  $r_{500}$  in pixels of the observed sample of 80 clusters.

Simulation A and B are spherically symmetric single elliptical  $\beta$  models. They only differ in their central radii, while simulation C has a highly elliptical core. These simulations create a baseline having unrealistic low (A,B) or high (C) ellipticity values. Simulation D and E consist of multiple  $\beta$  models in order to get more realistic power ratios.

---

<sup>1</sup><http://hea-www.harvard.edu/RD/zhtools/>

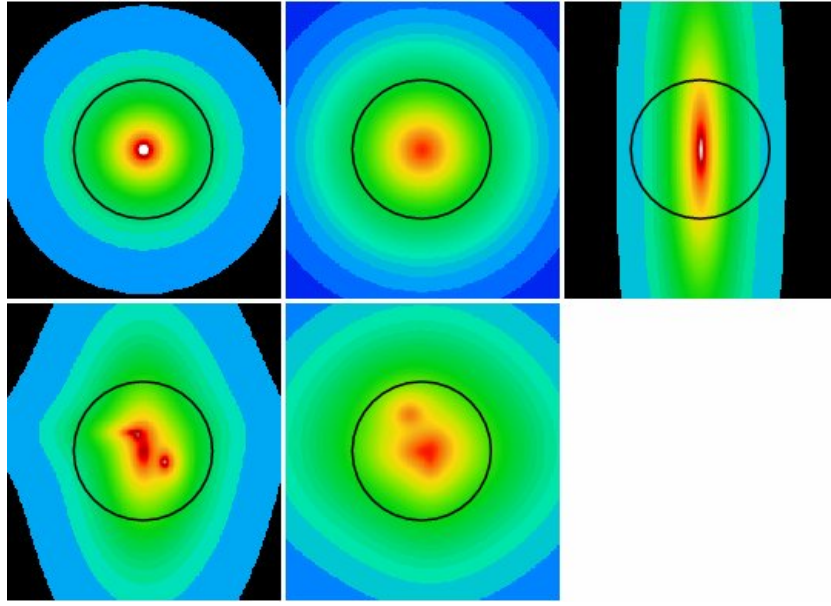


Figure 5.1: Ideal images without any noise for simulated clusters. Left to right, top panel: simulation A, B, C: bottom panel: simulation D, E. The circles indicate the aperture radius of 66 pixels for simulation A-E.

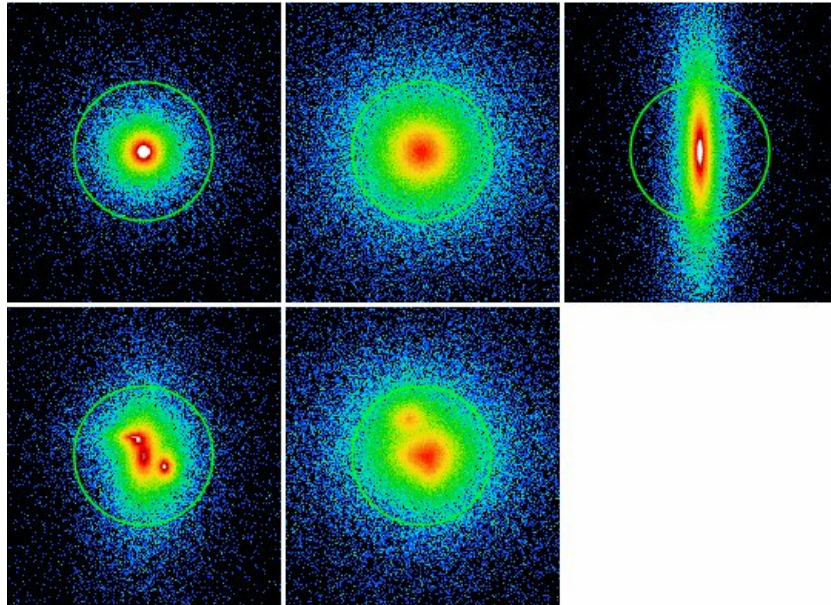


Figure 5.2: Images of simulated clusters with Poisson noise added. Left to right, top panel: simulation A, B, C: bottom panel: simulation D, E. The circles indicate the aperture radius of 66 pixels for simulation A-E.



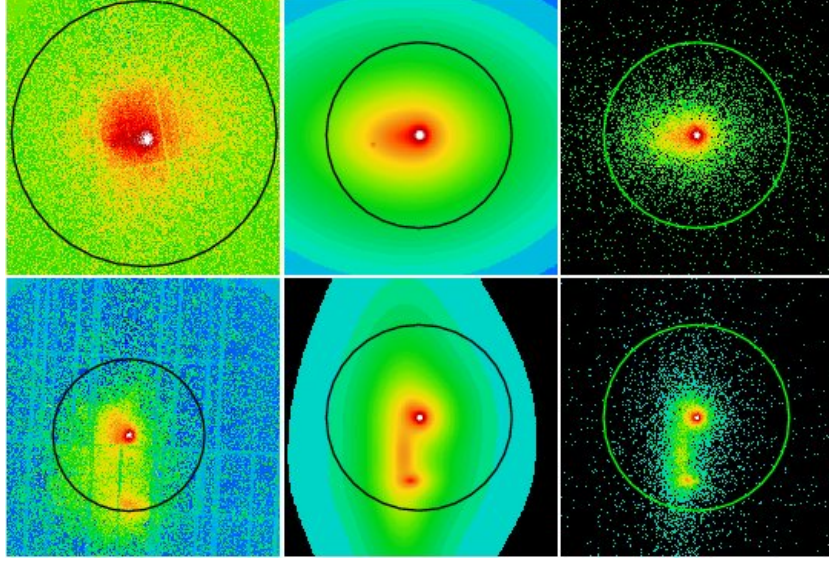


Figure 5.3: Left: Observed cluster image. Middle: modelled, ideal cluster image. Right: poissonised image. Top panel: A1775 and simulation H. Bottom panel: A115 and simulation F. The circles mark the aperture radius of  $r_{500}$  for the real cluster and of 100 pixels for the simulations.

The elliptical  $\beta$  model, which is used in the *kinging* task, is a two-dimensional model and can be described in the following way (e.g. Neumann & Böhringer 1997)

$$S(x, y) = S_0(1 + F_1 + F_2)^{-3\beta+1/2} + B \quad (5.7)$$

$$F_1 = \frac{[\cos\alpha(x - x_0) + \sin\alpha(y - y_0)]^2}{a_1^2} \quad (5.8)$$

$$F_2 = \frac{[-\sin\alpha(x - x_0) + \cos\alpha(y - y_0)]^2}{a_2^2} \quad (5.9)$$

where  $S_0$  is the central surface brightness,  $B$  the background,  $\alpha$  the position angle,  $x$  and  $y$  the positions of the center of the cluster and  $a_1$  and  $a_2$  the core radii for the major and minor axis.

Details about the different  $\beta$  models can be found in Table 5.1. The coordinates of the cluster center ( $x_{\text{cent}}, y_{\text{cent}}$ ) and the extension of the cluster core ( $x$  and  $y$  core radius) are given in pixels and correspond to  $x$ ,  $y$ ,  $a_1$  and  $a_2$  in equations 5.7-5.9. The center of the main cluster component (0,0) is chosen to be at the position (324,324) in a 648x648 pixel image. The number of expected total counts is set to  $3 \cdot 10^5$ , but varies a little bit from image to image due to the Poisson process. The Norm parameter gives the relative normalisation for each  $\beta$  model. The background  $B$  is set to zero, because the background is not of interest in this study. In addition,  $\alpha$  is set to zero, which means that the different  $\beta$  models are not rotated with respect to each other.

The position of the simulated clusters (mean of 100 poissonised images with  $3.16 \cdot 10^4$  total counts) with respect to the observed sample of 80 clusters in the P3/P0 - P4/P0 plane is shown in Figure 5.4. Simulation A and B, two spherical clusters, yield insignificant values for all power ratios. The extremely elliptical cluster of simulation C has very high even power ratios (P2/P0 and P4/P0) but very low P3/P0, reflecting high ellipticity but no substructure. Simulation D

and E have significant, but not too high power ratios and fit very well to the observed data. In addition, we create simulation F to analyse a cluster with very high power ratios, which is not the case for simulation A-E. Simulation H is comparable to simulation E.

Table 5.1: Details for simulations and  $\beta$  models used. Coordinates of the cluster center (xcent,ycent) and extension of the cluster core (x and y core radius) are given in pixel. The center of the main cluster component (0,0) is chosen to be at the position (324,324) in a 648x648 pixel image. The number of expected total counts is set to  $3 \cdot 10^5$  and  $\beta$  to 2/3 for all simulations. Norm gives the relative normalisation for each  $\beta$  model, where 1.0 equals 100%. Columns (1)-(7): Simulation A-H.

Simulation	A	B	C	D	E	F	H
	(1)	(2)	(3)	(4)	(5)	(6)	(7)
Number of $\beta$ models	1	1	1	4	4	4	4
$\beta$ model 1							
x core radius	3	15	3	5	15	3	5
y core radius	3	15	15	10	10	3	5
xcent	0	0	0	0	0	0	0
ycent	0	0	0	0	0	0	0
norm	1	1	1	1	1	1	1.15
$\beta$ model 2							
x core radius	-	-	-	3	10	7	0.5
y core radius	-	-	-	4	10	10	0.5
xcent	-	-	-	20	10	-9	-50
ycent	-	-	-	-10	5	4	-10
norm	-	-	-	0.4	0.6	0.2	0.01
$\beta$ model 3							
x core radius	-	-	-	5	10	6	35
y core radius	-	-	-	5	9	4	30
xcent	-	-	-	-5	-12	-10	-20
ycent	-	-	-	15	35	-68	-2
norm	-	-	-	0.3	0.5	0.2	0.4
$\beta$ model 4							
x core radius	-	-	-	5	8	10	25
y core radius	-	-	-	2	12	30	15
xcent	-	-	-	-10	8	-17	-17
ycent	-	-	-	18	-8	-41	-2
norm	-	-	-	0.2	0.5	0.6	1

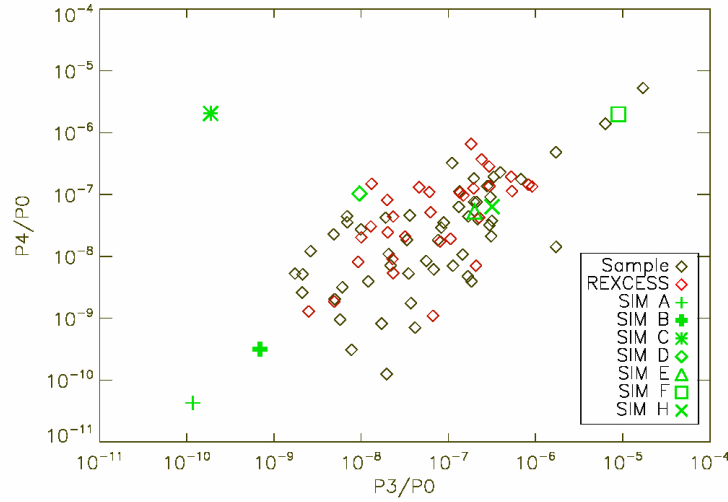


Figure 5.4:  $P3/P0$  -  $P4/P0$  plane with the sample of 80 observed clusters (black) including REXCESS (red) and the mean of 100 poissonised images for seven simulated clusters (green) and  $3.16 \cdot 10^4$  total counts.

### 5.1.2 Method of Böhringer et al. (2010)

In order to obtain precise (ideal) power ratios, corrections for the bias and error estimation are required. A relaxed cluster without any structure (e.g. simulation A) should yield power ratios equal to zero for all aperture radii. Due to numerical imprecision we obtain a very low, but non-zero signal for the ideal image of simulation A. Once noise is added (as is present in every real observation), the obtained signal of the same structureless cluster increases significantly. The power ratios should be the same, but due to photon noise structure is introduced. This is shown in Figure 5.5 in the left panel. The red line represents the ideal power ratios in 10 different aperture radii. Due to numerical imprecision, we obtain a non-zero but very low signal. The black lines show power ratios for 10 poissonised images of simulation A using  $3 \cdot 10^5$  counts. Once Poisson noise is added, the power ratios increase by more than 10 orders of magnitude. This illustrates that the effect of photon noise (which we simulate by adding Poisson noise to the image - thereafter called poissonising) is very important when dealing with low power ratios. Figure 5.5 (right) shows the comparison between 10 poissonised images (black lines) and the mean  $P3/P0$  of 100 poissonised images. The values are given as a ratio of  $[P3/P0]/[(P3/P0)_{\text{mean}}]$ , where  $(P3/P0)_{\text{mean}}$  is the mean of 100 poissonised simulations.

For a disturbed cluster (e.g. simulation F), the picture is different. Figure 5.6 (left) shows the comparison of the ideal power ratios (red line) and 10 poissonised ones (black lines) for 10 aperture radii using 100 000 total counts. As in the previous case, photon noise modifies structure. Unlike simulation A photon noise not only adds but sometimes smooths structure and thus yield too low power ratios. This effect is very mild for this simulation because the power ratio signal and the total counts are high. The - in this case very mild - effect that structure can also be smoothed by photon noise can be seen. This dependence on the counts will be discussed in section 5.3. It is however important to point out that these results show that photon noise (bias) does not always add structure (positive bias) but can also smooth it and yield lower power

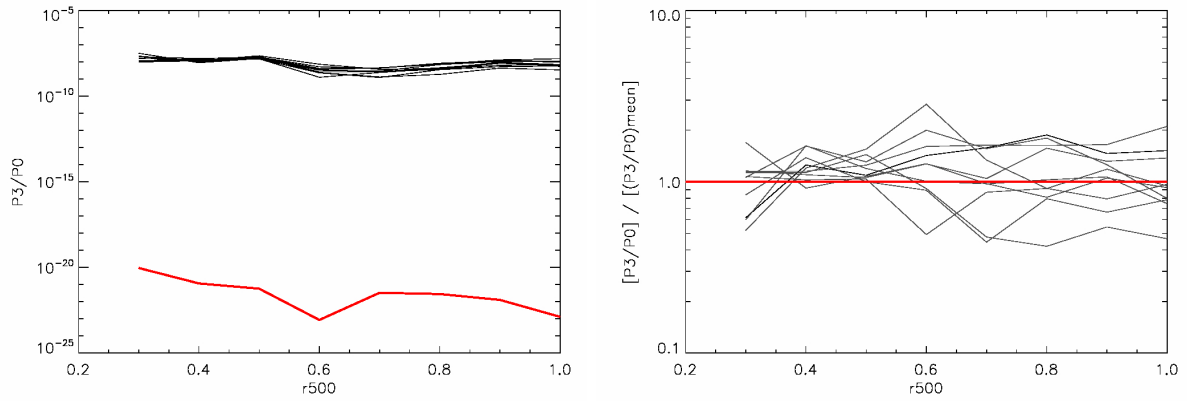


Figure 5.5: Simulation A:  $P3/P0$  derived in different aperture radii ( $0.1-1 r_{500}$ ) for 10 poissonised images with 300 000 total counts (black lines) and the ideal model (red line) without photon noise (left). Comparison between 10 poissonised images (black lines) and the mean  $P3/P0$  of 100 poissonised images (red line) (right). The values are given as a ratio of  $[P3/P0]/[(P3/P0)_{\text{mean}}]$ , where  $(P3/P0)_{\text{mean}}$  is the mean of 100 poissonised simulations.

ratios (negative bias). Figure 5.6 (right) shows the ratio  $[P3/P0]/[(P3/P0)_{\text{ideal}}]$  as a function of aperture radius and illustrates that sometimes negative biases ( $P3/P0 < (P3/P0)_{\text{ideal}}$ ) are found.

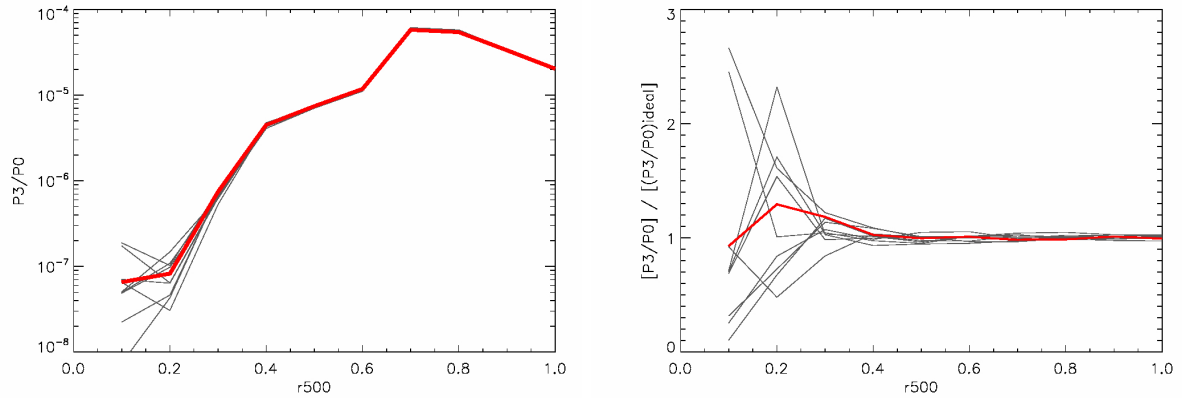


Figure 5.6: Simulation F:  $P3/P0$  derived in different aperture radii ( $0.1-1 r_{500}$ ) for 10 poissonised images with 100 000 total counts (black lines) and the ideal model (red line) without photon noise (left). Ratio  $[P3/P0]/[(P3/P0)_{\text{ideal}}]$  as a function of aperture radius (right). This illustrates that sometimes negative biases ( $P3/P0 < (P3/P0)_{\text{ideal}}$ ) are found.

Böhringer et al. (2010) estimate the bias and its error in the following way: For each pixel within the aperture radius only the radial distance is stored while the pixels are redistributed with random angles. Each pixel still has the same distance from the cluster center, but its position along this circle has changed. All azimuthal structure of the cluster is now randomly distributed. 100 redistributions are done and the mean of the power ratio signal computed (thereafter called B09-method). Ideally, this mean gives the power ratio of a regular cluster with the same amount of shot noise as the real observation. Therefore they conclude that this mean is the signal due to photon noise, subtract it from the power ratio signal of the observation and thus obtain a bias-corrected power ratio. Their thresholds above which a power ratio signal is significant are  $10^{-7}$  for P2/P0,  $2.4 \cdot 10^{-8}$  for P3/P0 and  $2 \cdot 10^{-8}$  for P4/P0. They conclude that this method is very useful for clusters with power ratios close to the threshold (no or small amount of structure), where the power ratio signal is dominated by randomly distributed photon noise.

For clusters with significant substructure, the photon noise will not be dominated by a random distribution but by the noise connected to the substructure. Shot noise will not create randomly distributed structure, but smoothen or boost the existing structure. Therefore a different method to estimate the error on the power ratio signal is needed. They poissonise the observation 200 times in order to simulate additional photon noise and again obtain a mean power ratio signal and a standard deviation  $\sigma$  (error estimation method). Those 200 images contain observational noise and Poisson noise on top of that, which yields a higher mean signal. The scatter ( $\sigma$ ) however is believed to be close to the Poisson uncertainty of the observed image. If this is the case, this  $\sigma$  can be used as error for the power ratios.

They subtract the bias determined by the B09-method from the observation to correct for shot noise and obtain the error on the power ratios from the error estimation method. The aim of this present work is to test the reliability of the proposed bias and error estimation method.

### 5.1.3 Bias

The real bias due to photon noise is the difference between the power ratio signal of an ideal image of a cluster ( $P_{\text{ideal}}$ ) and the signal of the same cluster with noise.

$$\frac{P - P_{\text{ideal}}}{P} = \text{bias} \quad (5.10)$$

We test the relation between the real bias (equation 5.10) and the bias calculated according to Böhringer et al. (2010) (B09-bias) using simulation A-E. We use an ideal, constant (=1) exposure map, which does not include any dead pixels or pixel rows, an aperture radius of 66 pixels and 300 000 total counts. We are using a constant (flat) exposure map, because the simulated observations are not affected by vignetting. We do not find the expected 1-1 correlation between the real and the B09-bias. Figure 5.7 shows that there is no correlation between the real and the B09-bias for P3/P0. The real bias spans a large range of values while the B09-bias always gives more or less the same value for all 100 poissonised images. The method of Böhringer et al. (2010) in general overestimates the bias and corrects too much. For simulation D and especially for E it mostly underestimates the bias. This underestimation is expected because the cluster has a significant signal and the noise is not dominated by randomly distributed photon noise but by noise connected to the structure. For P2/P0 and P4/P0 (Figure 5.8) a similar problem occurs. As long as the signal is low (A, B), the bias is overestimated, while it is mainly underestimated for a significant signal. However, the B09-bias is always positive for all five simulations, while the

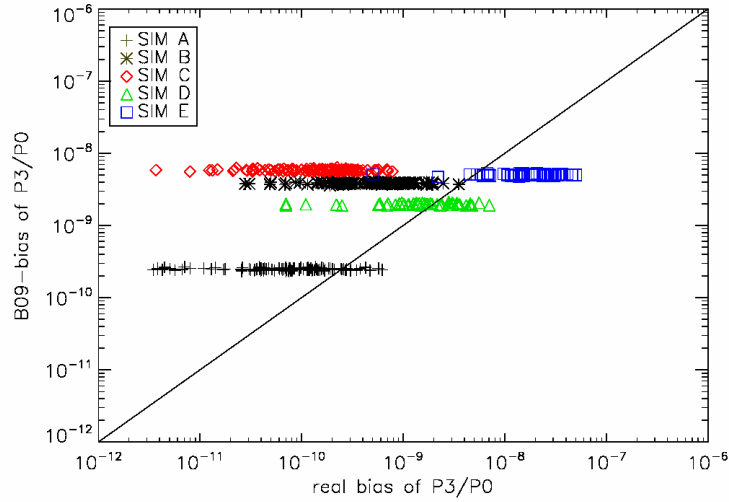


Figure 5.7:  $P3/P0$ . Comparison between the real bias due to photon noise and the computed B09-bias using 100 poissonised images of each simulation and a constant exposure map. The total counts are  $3 \cdot 10^5$ .

real bias is sometimes not. This indicates that shot noise in some cases smooths out structure and that structure sometimes needs to be added (negative bias) and not always removed. The negative values of the bias are not shown in the log-log Figure 5.7 and 5.8.

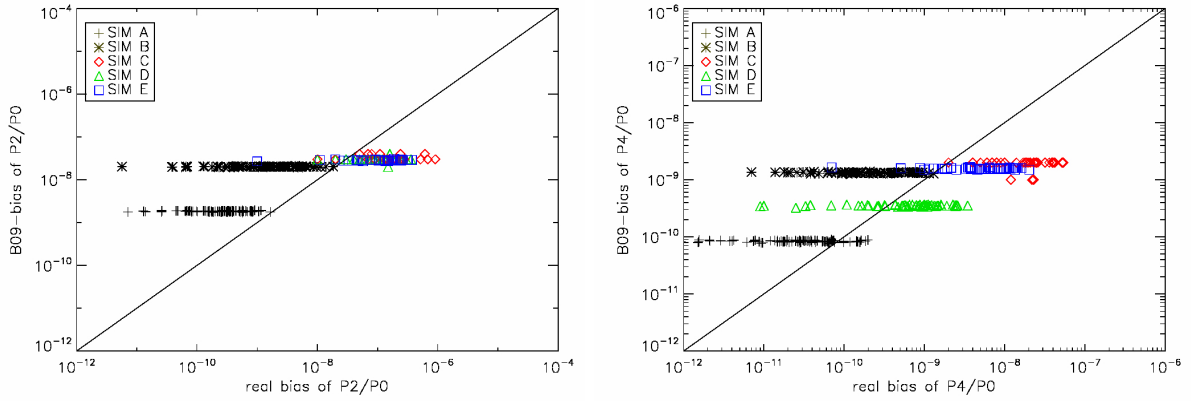


Figure 5.8: Comparison between the real bias due to photon noise and the computed B09-bias using 100 poissonised images of each simulation and a constant exposure map. Left:  $P2/P0$ , Right:  $P4/P0$ . The total counts are  $3 \cdot 10^5$ .

The B09-bias does not correlate with the real bias for each of the 100 simulation. The B09-bias however is given as the mean bias of 100 poissonised simulations. Therefore, we show Figure 5.9 and give Table 5.2 to illustrate that the bias estimation method (B09-bias) does not work for the mean of 100 simulations either. In order to do so, we show the fraction  $(\text{B09-bias})_{\text{mean}}/(\text{real bias})$  as a function of the mean  $P3/P0$  of 100 poissonised images for simulation A-E. Table 5.2 gives the same fraction for  $P2/P0$ ,  $P3/P0$  and  $P4/P0$ , where  $(\text{B09-bias})_{\text{mean}}$  is the mean B09-

bias of 100 poissonised images. A  $[(\text{B09-bias})_{\text{mean}}]/[\text{real bias}]$  ratio of 1 indicates that the values are identical and 2 that the B09-bias is twice as large as the real bias. The B09-bias always overestimates the real bias for the mean P3/P0 of 100 simulations. It seems to work best for a structureless cluster (simulation A), where the B09-bias and the real bias are almost the same. But this is only the case because the ideal simulation A has no signal ( $10^{-23}$ ) and the B09-bias is very similar to the measured mean P3/P0. For simulation B and C, which have almost the same ideal P3/P0 as simulation A, the B09-bias is far too high (factor 6 and 30). This is another indication that the B09-bias is not correlated with the real bias.

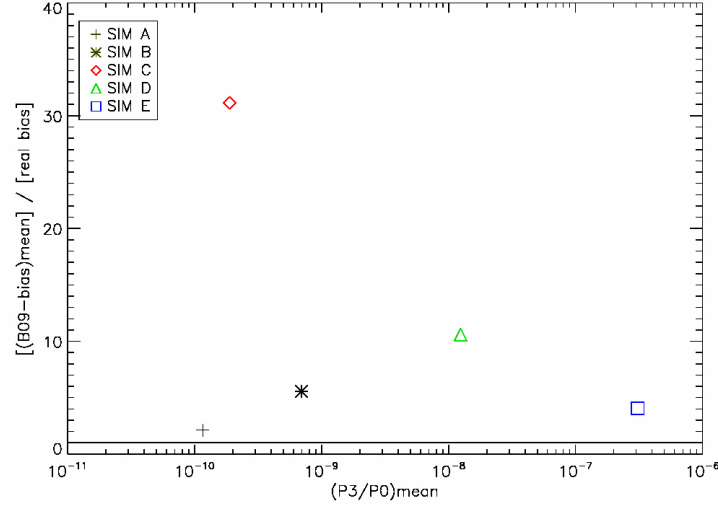


Figure 5.9: Ratio  $[(\text{B09-bias})_{\text{mean}}]/[\text{real bias}]$  as a function of the mean P3/P0 of 100 poissonised images for simulation A-E. The black line indicates a ratio of 1, where the B09- and real bias are the same.

Table 5.2: Ratio  $[(\text{B09-bias})_{\text{mean}}]/[\text{real bias}]$  for P2/P0, P3/P0 and P4/P0.  $(\text{B09-bias})_{\text{mean}}$  is the mean B09-bias of 100 poissonised images. 1 indicates that the values are identical and 2 that the B09-bias is twice as large as the real bias. A negative bias indicates that noise smoothed out structure and that structure needs to be added.

Simulation	P2/P0	P3/P0	P4/P0
(1)	(2)	(3)	(4)
SIM A	5.2	2.1	2.1
SIM B	7.8	5.6	6.0
SIM C	-0.1	31.1	-0.3
SIM D	-5.6	10.6	1.4
SIM E	-17.7	4.1	3.1

After discussing that the proposed bias-estimation method does not work as intended, we investigate how the bias depends on the total counts (total number of photons arriving at the detector and creating the image) and the initial amount of substructure. For simulation H and F, we vary the Norm parameter (expected total counts) from 1 000 to 100 000 and created 100 poissonised images for each value of total counts. We start with 1 000 counts (less than any observation in the sample of 80 clusters), because this is a typical value for high-redshift observations.

We find that the effect of photon noise becomes less important with increasing number of counts. The histograms in Figure 5.10 show the P3/P0 distribution of the ideal image of simulation H, which is poissonised 100 times for 1 000 counts (thin line histogram) and for 100 000 counts (filled histogram). The difference in the distribution is obvious. For higher total counts, the distribution is more peaked and narrow around the ideal value (thick solid line), while the P3/P0 distribution broadens a lot for low counts and becomes asymmetric around the mean. This long tail is shown in Figure 5.10 for 1 000 counts. In addition, the mean P3/P0 of 100 poissonised images for 1 000 (dotted line), 2 000 (dashed line), 3 160 (dashed-dotted line) and 10 000 counts (dash-dot-dotted line) are given. There is a significant offset of the mean P3/P0 and the ideal power ratio for very low counts. For 10 000 counts this offset becomes smaller and can be neglected for 30 000 counts or more.

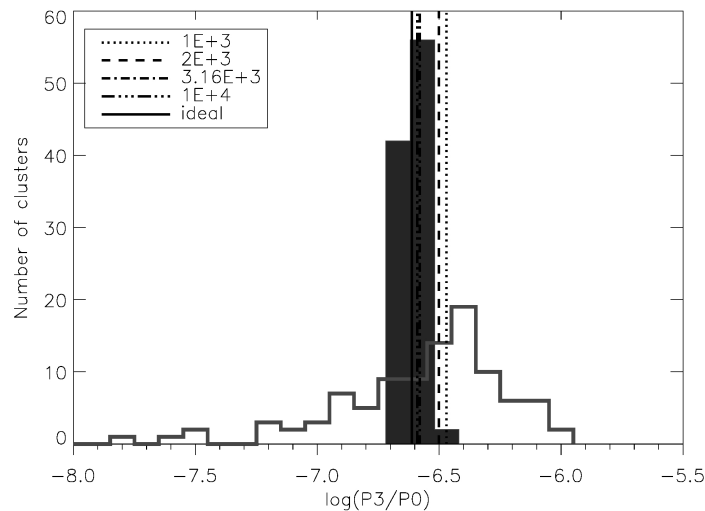


Figure 5.10: Simulation H. Histogram of P3/P0 distribution of 100 poissonised images of the model cluster for different total counts within the image. 1 000 counts (thin line histogram) and for 100 000 counts (filled histogram). In addition, the mean P3/P0 of 100 poissonised images is given for 1 000 (dotted line), 2 000 (dashed line), 3 160 (dashed-dotted line) and 10 000 total counts (dash-dot-dotted line).



The same histogram for the very structured simulation F shows a different picture. The P3/P0 distribution for 1 000 (thin line histogram) and 10 000 counts (filled histogram) is illustrated in Figure 5.11. Again, a broadening for low counts is visible, but the distribution is still very narrow compared to simulation H. The offset of the mean of 100 poissonised images for low counts (dotted line for 1 000 counts) is very small and can be neglected in this and all other cases with more total counts. This however is expected, because the effect of photon noise decreases with increasing amount of structure.

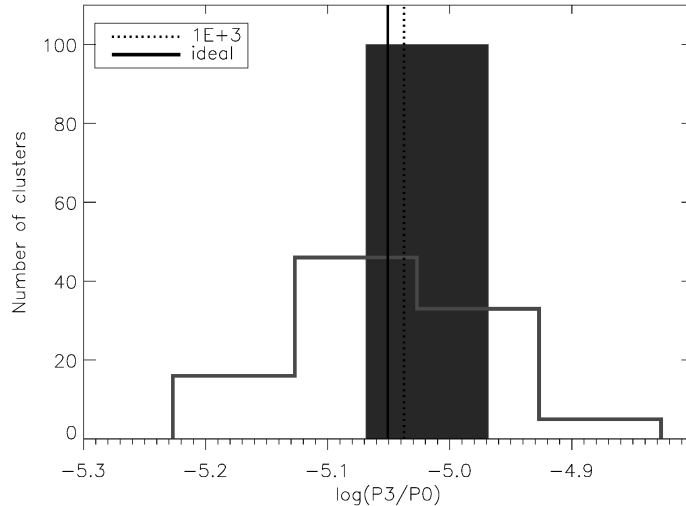


Figure 5.11: Simulation F. Histogram of P3/P0 distribution of 100 poissonised images of the model cluster for different total counts within the image. 1 000 counts (thin line histogram) and for 100 000 counts (filled histogram). In addition, the mean P3/P0 of 100 poissonised images is given for 1 000 (dotted line) total counts is given.

We conclude that the method of Böhringer et al. (2010) is a step in the right direction to estimate the bias. However, it does not work as intended, because it seems to subtract too much structure for images with large substructure signal. Furthermore, the effect of photon noise depends on the amount of initial structure (compare Figure 5.10 for small amounts of structure and 5.11 for significant structure), the total counts and also the morphology of the cluster itself (section 5.1.6). For low power ratio signals, the bias needs to be taken into account for images with less than 30 000 counts, while it can be neglected for all total counts in the case of high power ratios. We agree with Böhringer et al. (2010) about the fact that the bias is not important for significant power ratio signals, but disagree with the applied method. We thus suggest to drop the idea of subtracting a bias and try to calibrate the power ratio signal using a calibrated scaling relation between P3/P0 and  $(P3/P0)_{\text{ideal}}$ . Unfortunately the bias seems to be cluster specific. We thus perform several tests which will be discussed in detail in section 5.1.6.

#### 5.1.4 Error estimation

After concluding that the B09-bias does not correspond to the real bias and that the real bias is negligible for high power ratios and high total counts, we investigate the error estimation method proposed by Böhringer et al. (2010). They assume that the standard deviation  $\sigma$  of 200

repoissonised images of the observation is similar to the  $\sigma$  of the initial power ratio measurement. In order to test this, we use simulation H and F, which are already discussed in section 5.1.1. Our goal is to find out whether the method proposed by Böhringer et al. (2010) gives accurate results. We thus test the method step by step and under different conditions. At first we create noisy images from simulated cluster images. We take the ideal models H and F and create 200 poissonised images for each model. We add Poisson noise in the same way as for the bias analysis, using the *poisson* task from *zhtools*. This process is thereafter called first poissonisation. Each of those 200 poissonised images per model can be seen as an observation. As an observer however, we get only one image and do not know the ideal power ratio or the  $\sigma$ . Böhringer et al. (2010) suggest that the  $\sigma$  of the observation can be estimated by repoissonising the observation and obtaining the  $\sigma$  through the width of the computed power ratio distribution. For this method, the bias (discussed in the previous section) is not subtracted, but the initial observation is used, because only the distribution ( $\sigma$ ) and not the mean power ratio is of interest.

After the first poissonisation, we choose three images for each of the two models, thus six "observations". We compute the width of the distribution ( $\sigma$ ) for both simulations and take images which have the following three P3/P0: mean- $\sigma$ , mean, mean+ $\sigma$ . Each of those six images is repoissonised. This means that 200 poissonised images are created from each of those six chosen ones. This process is called second poissonisation. While images after the first poissonisation (mean- $\sigma$ , mean, mean+ $\sigma$ ) can be seen as real observations, the images after the second poissonisation are only used to estimate the  $\sigma$ . If the assumption of Böhringer et al. (2010) is correct, the  $\sigma$  of the ideal model (simulation F, H) and the poissonised images (mean- $\sigma$ , mean, mean+ $\sigma$ ) should be very similar. This means that the power ratio distribution after the first ( $\sigma$  of F, H) and second poissonisation ( $\sigma$  of mean- $\sigma$ , mean, mean+ $\sigma$ ) should be the same. We find that this relation holds well (maximal difference 30%). However, there seems to be a dependence on the number of counts and the amount of initial structure in the observation. Figure 5.13 and 5.12 illustrate this result. Figure 5.12 shows that the power ratio of the observation or in our case after the first poissonisation of the ideal images of simulation H and F (P3/P0 of mean- $\sigma$ , mean, mean+ $\sigma$ ) is closely related to the mean P3/P0 after repoissonising the six chosen images (second poissonisation). This relation is only violated for cluster with low counts, because such observations are very much affected by adding photon noise on top of an already noisy image. The mean after the second poissonisation is not used in the further analysis. It however underlines again the dependence on the effect of photon noise on the amount of counts and structure in the image.

The error estimation method through repoissonising the observation works well and is shown in Figure 5.13. In general the error on the real distribution ( $\sigma$  of P3/P0 after first poissonisation) and the error on the repoissonised distribution ( $\sigma$  of P3/P0 after second poissonisation) match well. The average residuals  $[\sigma_{\text{second poissonisation}} - \sigma_{\text{first poissonisation}}]/[\sigma_{\text{first poissonisation}}]$  are less than 10% and increase to at most 30% for very low counts. The residuals decrease for higher total counts and more structure. The residual for simulation H averaged over seven different total counts is 0.07 (7%) while it decreases to 0.01 (1%) for simulation F. This shows that the method works best for clusters with more initial structure (simulation F) and for high counts.

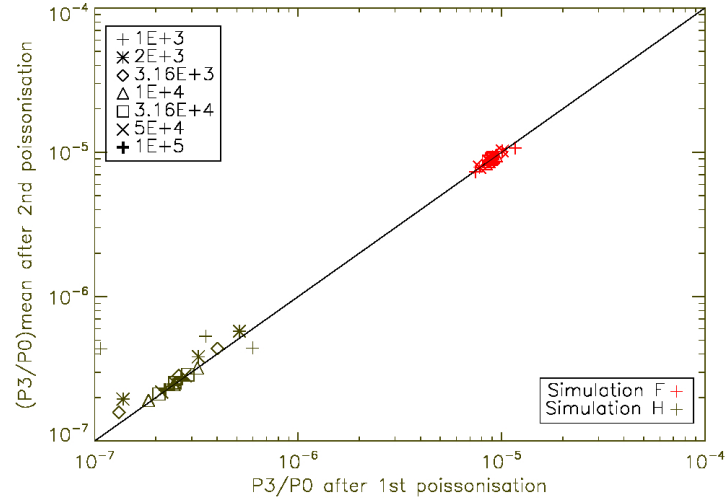


Figure 5.12: Comparison between  $P3/P0$  after the first poissonisation of the ideal model ( $P3/P0$  of mean- $\sigma$ , mean, mean+ $\sigma$ ) and the mean  $P3/P0$  of 200 poissonised images after the second poissonisation (repoissonisation of mean- $\sigma$ , mean, mean+ $\sigma$ ) using simulation H and F.

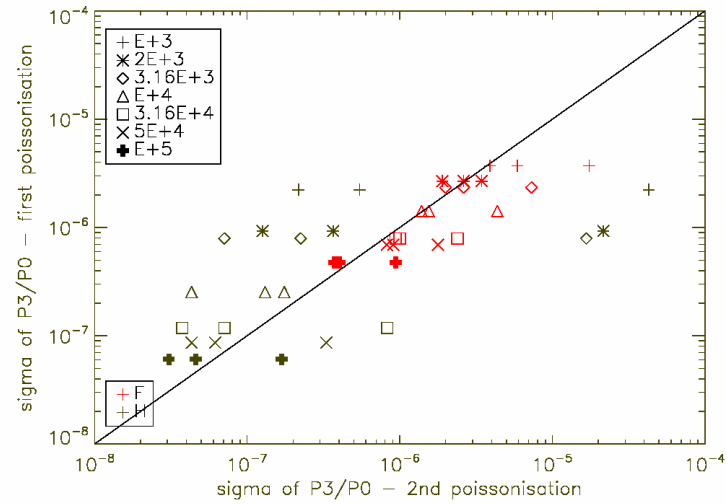


Figure 5.13: Comparison between the real  $P3/P0$  distribution ( $\sigma$  of  $P3/P0$  after first poissonisation) and the repoissonised distribution ( $\sigma$  of  $P3/P0$  after second poissonisation) using simulation H and F.

We conclude that the error estimation method works very well for observations with high counts or high power ratios (error of a few %). The reliability of the method decreases with decreasing total counts and power ratios (error up to 30%). We therefore agree with this method to estimate the error on the power ratio measurement and use it in our analysis of the observed clusters.

### 5.1.5 Method of Sanders (2006) - *contbin*

The error estimation works best for cases with a  $P3/P0$  close to the true (ideal) value. However, the method introduced by Böhringer et al. (2010) does not correct the bias as intended (see section 5.1.3). Another method to account for the bias by removing the noise is to smooth the image. We test several methods including wavelets and adaptive binning. We obtain the best results using the *contbin* technique of Sanders (2006). This method first smooths the image using a certain S/N ratio (*smoothsn*) and then creates bins with a defined S/N ratio (*sn*). We perform a parameter study and show as an example three pairs of parameters which yield the best results: (*smoothsn*,*sn*)=(10,1),(15,1),(25,1). We use simulation F and H and bin the images with the three sets of parameters for different number of counts. Figure 5.14 shows simulation H binned using the three parameter pairs (top panel) and the residuals (bottom panel). The residuals are calculated as described in equation 5.10. In these three cases the binned results are very similar. The point source however causes trouble for the parameter pairs (15,1) and (25,1), because the signal-to-noise ratio in each bin is too high. Bad binning therefore modifies structure.

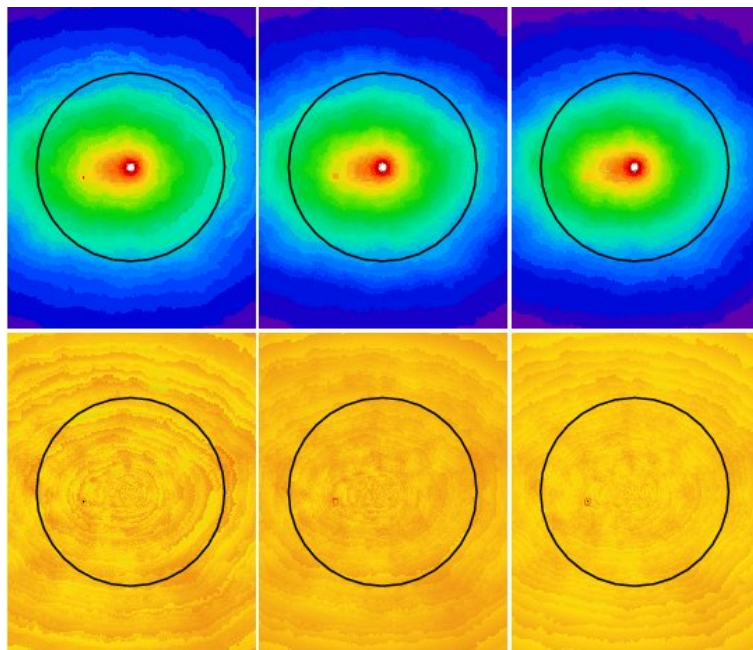


Figure 5.14: Simulation H. Top panel: Images with 50 000 total counts binned using the *contbin* technique of Sanders (2006) and the following parameters (*smoothsn*, *sn*): left (10,1), middle (15,1), right (25,1). Bottom panel: Residuals of the binned images in % of the ideal image.

The improvement of binning the image in order to get rid of the noise is very small. For clusters with large amounts of noise (large residuals) the method smooths the image and thus the noise decreases. The remaining residuals however are still very high and the bias is still too large to

obtain accurate results. We thus conclude that while the *contbin* method decreases the photon noise for very noisy observations, the improvement is not good enough to correct for the bias. Smoothed images are still affected by photon noise and give inaccurate results. Power ratios containing small biases due to photon noise stay almost unchanged (range of a few %).

### 5.1.6 Attempt to calibrate power ratios

Bias correction using the method of Böhringer et al. (2010) and binning using *contbin* is not as successful as hoped. Another way of obtaining the bias-corrected power ratio measurement is using a calibrated relation between the measured power ratio and the ideal value. Taking the results of the previous sections into account, this relation should depend on the total number of counts within the aperture radius and the absolute value of  $P3/P0$ . We thus try to find a relation between the total counts, the ideal power ratio and the obtained power ratio. If the real bias depends on the total counts only, then a ratio like  $[(P3/P0)_{\text{ideal}}]/[(P3/P0)_{\text{mean}}]$  should get closer to 1 with increasing total counts, because the effect of photon noise decreases. We take the mean of 100 simulations to illustrate our results. Figure 5.15 shows the ratio  $[(P3/P0)_{\text{ideal}}]/[(P3/P0)_{\text{mean}}]$  as a function of total counts. The bias decreases (ratio  $[(P3/P0)_{\text{ideal}}]/[(P3/P0)_{\text{mean}}]$  gets closer to 1) for increasing counts, this trend however depends on the cluster, thus the initial amount of substructure detected. Simulation A is - ideally - a symmetric cluster with almost no signal (in the range of  $10^{-23}$ ), the noisy images however yield much higher power ratios (around  $10^{-8}$ ). Therefore the shown ratio is very small compared to all other clusters which have - ideally - much higher power ratios. For simulation H and especially F, a very structured cluster, the dependence on the total counts is negligible.

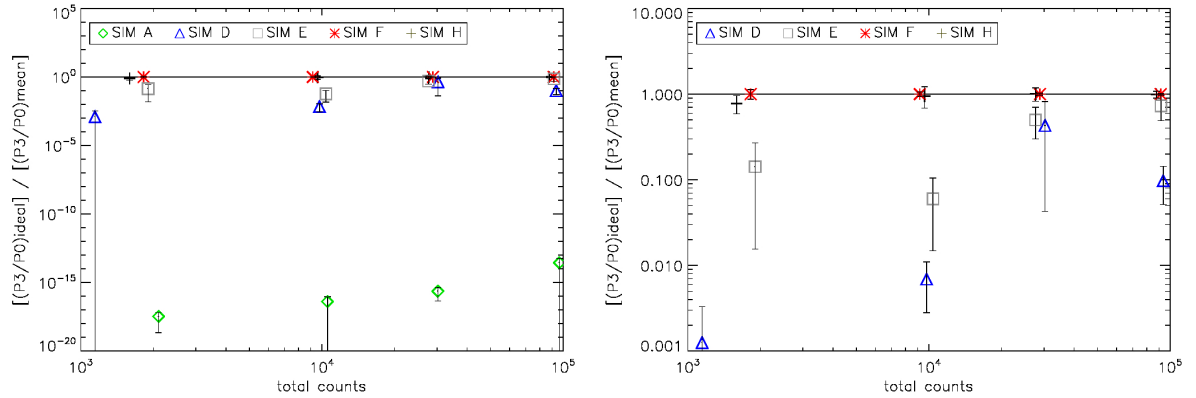


Figure 5.15: Ratio  $[(P3/P0)_{\text{ideal}}]/[(P3/P0)_{\text{mean}}]$  as a function of total counts for five simulations.  $(P3/P0)_{\text{ideal}}$  represents the ideal power ratio without any noise, while  $(P3/P0)_{\text{mean}}$  is the mean power ratio of 100 simulated, noisy clusters. All power ratios are obtained within  $r_{500}$ . Relation for all five simulations (left), excluding simulation A (right).

After establishing that the bias does not only depend on the total counts but also on the obtained power ratio signal, we decided to investigate the relation between  $(P3/P0)_{\text{ideal}}$  and  $[(P3/P0)_{\text{mean}}]/[(P3/P0)_{\text{ideal}}]$ . Figure 5.16 shows the ratio  $[(P3/P0)_{\text{mean}}]/[(P3/P0)_{\text{ideal}}]$  as a function of  $(P3/P0)_{\text{ideal}}$  for five different clusters (power ratios) and two different total counts ( $10^3$ ,  $10^5$ ). The dependence on the type of cluster substructure is obvious. Again the improvement of the power ratio measure with increasing total counts is visible (compare open and filled sym-

bols). Only for simulation F, the improvement cannot be seen because all power ratio (low and high counts) are very similar to each other. In addition, the bias decreases for increasing power ratios, as is shown before.

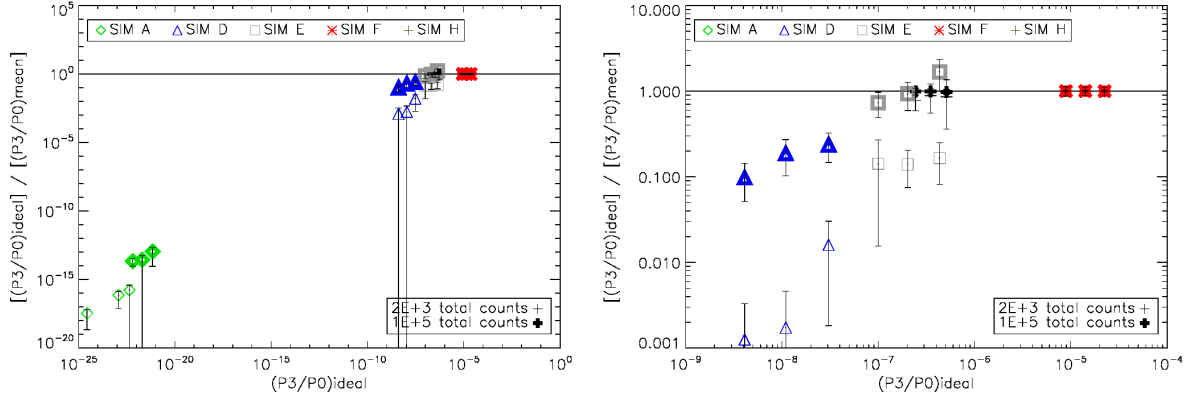


Figure 5.16: Ratio  $[(P3/P0)_{ideal}] / [(P3/P0)_{mean}]$  as a function of  $(P3/P0)_{ideal}$  for five simulations and two different total counts:  $10^3$  (open symbols) and  $10^5$  (filled symbols).  $(P3/P0)_{ideal}$  represents the ideal power ratio without any noise, while  $(P3/P0)_{mean}$  is the mean power ratio of 100 simulated, noisy clusters. All power ratios are obtained within the aperture radii 0.8, 0.9 and 1  $r_{500}$ . Relation for all five simulations (left), excluding simulation A (right).

The combined results shown in Figure 5.15 and 5.16 indicate that the bias does not only depend on the total counts or the obtained power ratio, but that it depends on both and probably the morphology of the cluster itself. If the bias depends on the shape of the cluster itself, this method of calibrating the power ratios cannot work. We thus perform the following test: two clusters which have the same power ratio have the same amount of structure. If we compare the power ratio of these two clusters in different aperture radii, we find that the power ratios are the same for cluster X in aperture radius  $r_x$  and cluster Y in aperture radius  $r_y$ . One can thus assume that one cluster is a scaled-down version of the other one. If they also have the same amount of total counts, both variables - counts and power ratio - are fixed and only the intrinsic shape of the cluster remains different. We investigate this idea and at first compare the ideal power ratios in different aperture radii for  $10^5$  total counts in Figure 5.17. As is indicated by the dotted lines, the ideal P3/P0 are the same for simulation D in 0.7  $r_{500}$  and simulation E in  $r_{500}$ .

We thus investigate the real bias (equation 5.10) for those two clusters in the chosen aperture radii. The result is shown in Figure 5.18. We obtain the real bias for 100 poissonised images of simulation D and E for the above mentioned aperture radii. In this histogram we thus fix the total counts ( $10^5$ ) and the P3/P0 ( $10^{-7}$ ). The only variable in this context is the cluster shape and as can be seen, this variable matters. If only the total counts and the obtained P3/P0 are responsible for the bias, the bias should be the same for the two mentioned cases. However Figure 5.18 shows that this is not the case. The comparison between the real bias of 100 poissonised images for simulation D within 0.7  $r_{500}$  (filled histogram) and 100 poissonised images for simulation E within  $r_{500}$  (line histogram) shows that the bias distribution is very different for both cases. Also the mean bias of those 100 simulations, which is indicated with the dotted line for simulation D and the dashed line for simulation E, is very different, but decreases with increasing P3/P0.

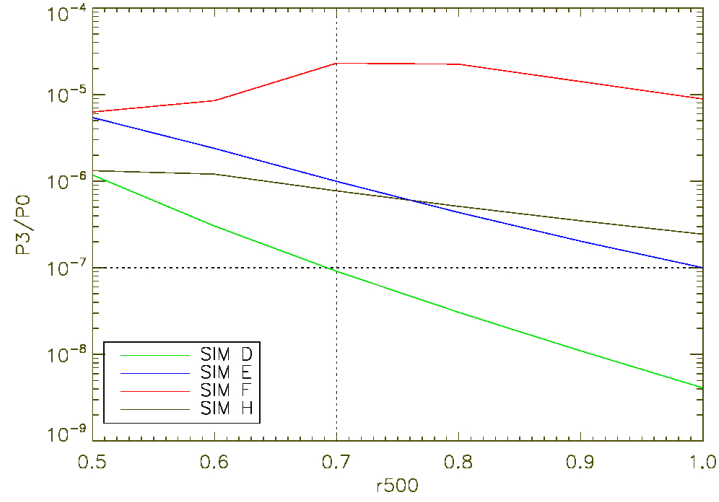


Figure 5.17:  $(P3/P0)_{\text{ideal}}$  for  $10^5$  total counts as a function of aperture radius. The dotted lines indicate where simulation D and E have the same  $P3/P0$ .

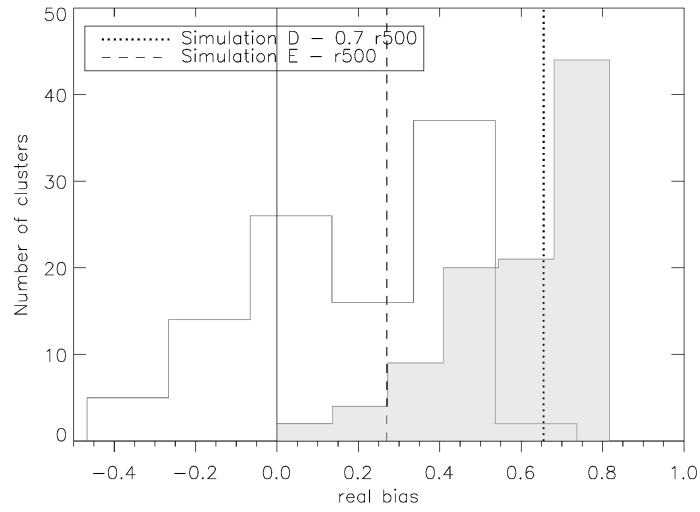


Figure 5.18: Histogram of the distribution of the real bias of 100 poissonised images of simulation D and E. The aperture radii are  $0.7 r_{500}$  for simulation D (filled histogram) and  $r_{500}$  for simulation E (line histogram). For those apertures the  $P3/P0$  and the total counts are the same for both simulations. The lines indicate the mean bias of 100 poissonised images for simulation D (dotted line) and E (dashed line) and clearly show that the bias does not only depend on the  $P3/P0$  and total counts but also on the morphology of the cluster.



We conclude that the bias decreases with increasing total counts or increasing power ratios. There is however no simple relation between the total counts, the power ratio and the bias. This shows that the photon noise depends on the shape of the clusters and thus cannot be estimated using a calibrated relation. This issue however will be addressed in future studies using a large number of simulated clusters.

## 5.2 Dependence on aperture radius

Power ratios are obtained by integrating over a certain aperture radius (see section 5). In addition, weighting proportional to  $r^m$  is applied during the integration, where  $m$  is the order of the power (e.g.  $m=2$  for P2). Therefore, structure closer to the aperture radius ( $r \sim r_{\text{ap}}$ ) is weighted more than structure closer to the center ( $r \ll r_{\text{ap}}$ ). This is negligible for regular clusters, but becomes very important for clusters with visible clumps, e.g. merging subclusters. It is thus not insignificant which aperture size is used. The dependence on the aperture radius was already mentioned in previous studies (e.g. Buote & Tsai 1995, 1996), however it was never discussed in such detail.

In the literature, cluster dependent ( $r_{500}$ ) and fixed sizes are used (e.g. 0.5 or 1 Mpc). A fixed aperture should be used only if equal-redshift clusters are compared, which is not the case in our work. In addition, we want to take the cluster size for closely self-similar cluster structure into account and therefore a scaled radius like  $r_{500}$  is used. The power ratio method is sensitive to large-scale disturbances in the gravitational potential of a cluster. Structure outside a certain radius cannot influence the cluster potential anymore enough to be picked up by the method. In addition, high quality data is needed to obtain accurate results. Thus,  $r_{500}$  is a very good compromise when dealing with clusters with different redshifts.

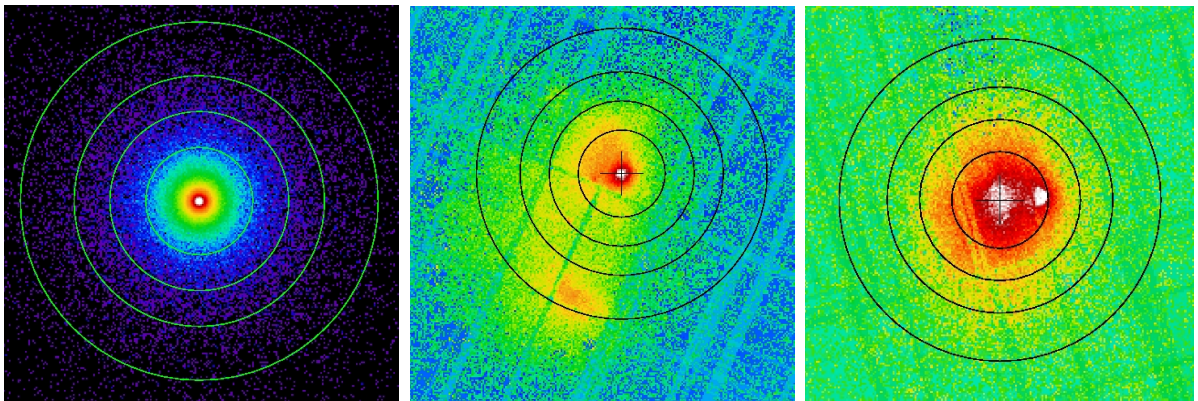


Figure 5.19: Simulation A with Poisson noise (left), A115 (middle), bullet cluster (right). The circles mark 0.3, 0.5, 0.7 and 1  $r_{500}$ .

In order to illustrate this dependence, three clusters are chosen and their power ratio P3/P0 shown for 10 different aperture radii: 0.1-1  $r_{500}$ . Figure 5.19 shows simulation A (left) and the real observations of A115 and the bullet cluster. Their power ratios as a function of aperture size are shown in Figure 5.20.



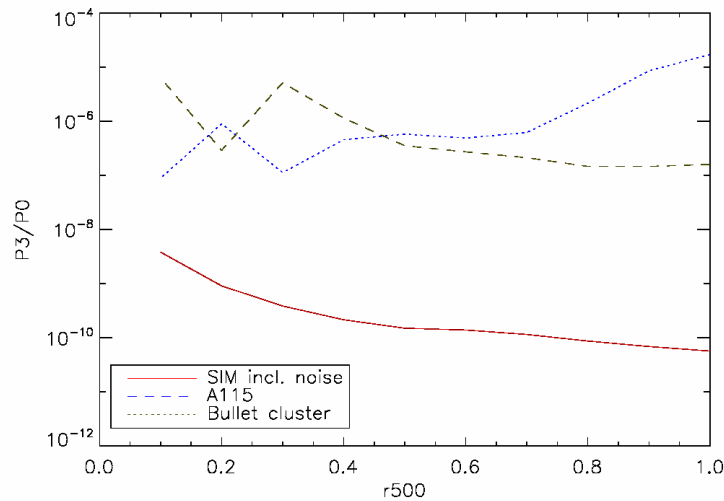


Figure 5.20:  $P3/P0$  for the three chosen clusters for 10 different aperture radii.

A symmetric cluster without any substructure should yield zero for all power ratios and in all aperture radii. However, every real observation is effected by photon noise, thus photon noise is added to this simulation. A regular cluster like simulation A (Figure 5.19 left) has very similar, low values of - in this case -  $P3/P0$  in all aperture radii, except for the innermost radii. For  $r_{ap} < 0.3 r_{500}$ , the effective photon noise increases and yields too high power ratios. If the size of one pixel is comparable to the radius, it spuriously introduces structure. This depends on the angular resolution of the observation. In our case, we think that only power ratios within aperture radii larger than  $0.3 r_{500}$  should be analysed.

The  $P3/P0$  signal changes for different  $r_{ap}$  for clusters with substructure. This is illustrated by the signals of A115 and the bullet cluster in Figure 5.20. A115 is a very interesting case, because it consists of two clusters. Here the weighting of structure with radius becomes important. As long as the aperture radius is small enough, only the first subcluster is enclosed and the signal is moderately constant for several  $r_{ap}$ . At larger radii however the gas bridge between the two subclusters introduces asymmetry and the signal starts to increase. As soon as the second subcluster is enclosed, the power ratio increases by more than a factor of 10 compared to medium sized apertures (e.g.  $0.5 r_{500}$ ).

While A115 would be classified as disturbed cluster within all  $r_{ap}$ , the bullet cluster would not. The peak in the signal at  $0.3 r_{500}$  is very strong, but the signal decreases with increasing  $r_{ap}$ . The "bullet" is just enclosed at  $0.3 r_{500}$ , but at  $r_{ap}=r_{500}$  it is very close to the center and weighted accordingly less. The bullet cluster is a well-known merging and thus disturbed cluster, but can only be classified as such if the aperture radius is small enough.

We thus investigate not to use a single aperture for our classification, but to combine power ratios obtained in several apertures. In this work, we explore the use of the mean and the standard deviation of several apertures.

## Mean and $\sigma$

Power ratios are sensitive to the size of the aperture and yield different results for disturbed clusters. Therefore it is not recommended to use a single aperture size but to combine the radii 0.3 to  $1 r_{500}$  when investigating the global cluster structure. The most simple combination would be the use of the mean of the eight power ratio measurements. This however smooths single peaks in the signal like for the bullet cluster and yields a lower signal. We thus suggest to use the standard deviation  $\sigma$  of the eight power ratio measurements. A regular cluster with only shot noise yields very similar power ratios for all aperture radii, because there is no structure which can be detected and produce peaks. A very disturbed cluster would not produce a constant high signal but a signal with one or more peaks. The  $\sigma$  of eight apertures therefore better characterises a cluster on a global scale than the combined mean or the power ratio of a single aperture. This will be illustrated in section 6.3 and 6.4.3.

## 5.3 Dependence on total counts

The dependence of the power ratio method and especially its bias on the amount of total counts within the aperture radius is already mentioned in section 5.1.3. In this section, we want to illustrate this dependence using three simulations: simulation A (spherical cluster without any structure), simulation F (very disturbed cluster) and simulation E (significant structure). In section 5.1.3 we discuss that the effect of Poisson noise decreases for increasing total counts and thus that the power ratio measurement becomes more accurate. This effect is very important when dealing with high redshift clusters. The number of total counts decreases with increasing redshift, because the exposure times are limited. We thus investigate until which counts threshold the power ratio method is reliable.

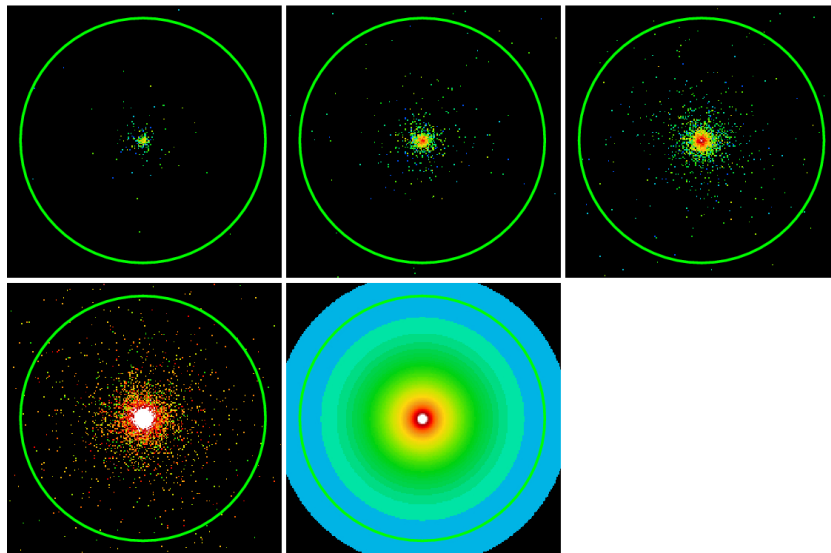


Figure 5.21: Simulation A. Poissonised images with different total counts and the ideal image. Top panel left to right:  $2 \cdot 10^3$ ,  $10^4$ ,  $3.16 \cdot 10^4$ . Bottom panel left to right:  $10^5$ , ideal image. The circles mark the aperture radius of 100 pixel.

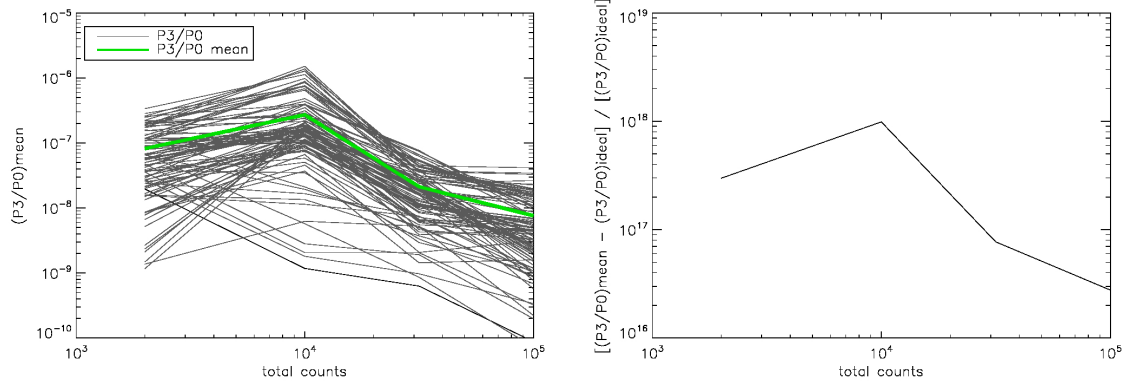


Figure 5.22: Simulation A.  $P3/P0$  of 100 poissonised images (black lines) within an aperture radius of 100 pixels as a function of total counts. In addition, the mean  $P3/P0$  of these 100 poissonised images is shown (green line). The ideal  $P3/P0$  is in the range of  $10^{-25}$  and not part of this figure (right).  $P3/P0$  residuals (ratio  $[(P3/P0)_{\text{mean}} - (P3/P0)_{\text{ideal}}] / [(P3/P0)_{\text{ideal}}]$ ) as a function of total counts, where 0 indicates that the ideal and noisy power ratios are the same (right).

The images of simulation A for four different total counts and the ideal image are shown in Figure 5.21. The total counts in the poissonised images range from  $2 \cdot 10^3$  to  $10^5$ , while the ideal image does not change with counts. The circles mark the aperture radius of 100 pixels. The dependence of the power ratios on the total counts is illustrated in Figure 5.22 for simulation A. On the left side, the  $P3/P0$  of 100 poissonised images (black lines) within an aperture radius of 100 pixels as a function of total counts is shown. The mean  $P3/P0$  of these 100 poissonised images is marked by the green line. The ideal  $P3/P0$  is in the range of  $10^{-23}$  and not part of this figure. Figure 5.22 (right) shows the  $P3/P0$  residuals (ratio  $[(P3/P0)_{\text{mean}} - (P3/P0)_{\text{ideal}}] / [(P3/P0)_{\text{ideal}}]$ ) as a function of total counts, where 0 indicates that the ideal and noisy power ratios are the same. As is already obvious from the visual inspection of Figure 5.21, the effect of noise is severe at low counts, but also high counts images are affected. This is indicated by the extremely high residuals. The ideal cluster has no noise and therefore yields very low power ratios, which are due to numerical noise. "Observed", noisy clusters however yield power ratios in the range of  $10^{-8}$ . This means that substructure can be boosted from no signal to signals higher than  $10^{-7}$  at low and  $10^{-8}$  at high counts by photon noise. Böhringer et al. (2010) give a threshold of  $2 \cdot 4 \cdot 10^{-8}$  for significant structure, all signals below are only due to noise. This threshold was computed after subtracting the B09-bias and for fixed total counts. This method of computing the bias does not work as intended and cannot be applied for this analysis. Therefore, we cannot directly apply this threshold for our analysis. In case of clusters without intrinsic structure (in contrary to structure due to photon noise), photon noise boosts the power ratio signal to mildly significant values. This effect is very strong for all total counts. Therefore, a threshold above which structure is only due to intrinsic structure and not due to noise needs to be defined.

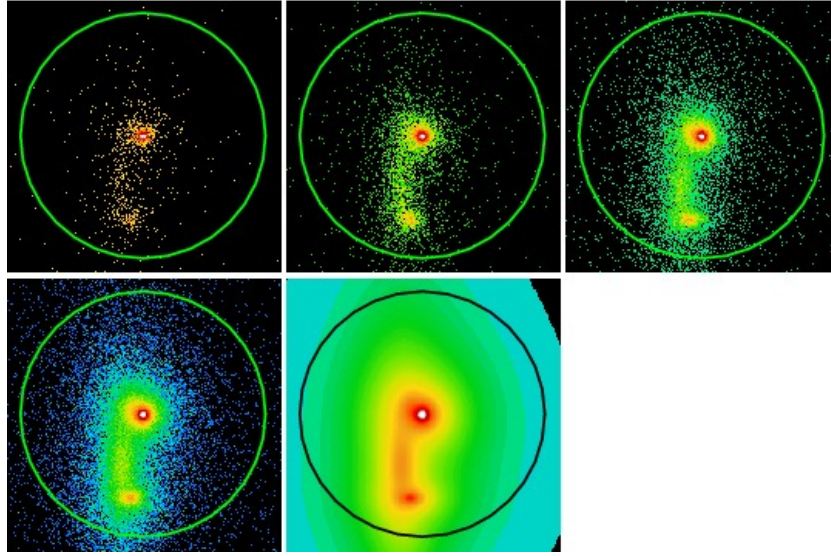


Figure 5.23: Simulation F. Poissonised images with different total counts and the ideal image. Top panel left to right:  $2 \cdot 10^3$ ,  $10^4$ ,  $3.16 \cdot 10^4$ . Bottom panel left to right:  $10^5$ , ideal image. The circles mark the aperture radius of 100 pixel.

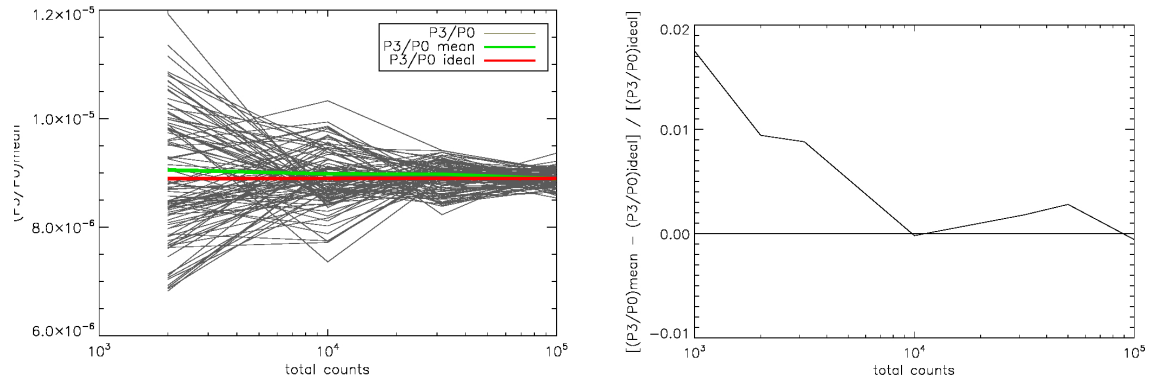


Figure 5.24: Simulation F.  $P3/P0$  of 100 poissonised images (black lines) within an aperture radius of 100 pixels as a function of total counts. In addition, the mean  $P3/P0$  of these 100 poissonised images is shown (green line). The ideal  $P3/P0$  is indicated by the red line (left).  $P3/P0$  residuals (ratio  $[(P3/P0)_{\text{mean}} - (P3/P0)_{\text{ideal}}] / [(P3/P0)_{\text{ideal}}]$ ) as a function of total counts, where 0 indicates that the ideal and noisy power ratios are the same (right).

Simulation F shows a different picture. This simulation has a lot of intrinsic structure, which is also visible at lowest counts in Figure 5.23. Figure 5.23 shows simulation F for four different total counts and the ideal image, as in the case of simulation A. With increasing total counts, the intrinsic structure becomes more and more pronounced because the effect of photon noise lessens. This result from visual inspection of the images is in agreement with the trend we see when investigating residuals. Figure 5.24 (left) shows the  $P3/P0$  of 100 poissonised images (black lines) within an aperture radius of 100 pixels as a function of total counts. In addition, the mean  $P3/P0$  of these 100 poissonised images (green line) and the ideal  $P3/P0$  (red line) are shown. Even at low counts the measured power ratios for the 100 poissonised images are very similar to the mean (green line) and the ideal  $P3/P0$  (red line). There is a wider spread in power ratios for lower counts, but this spread vanishes at high counts. Figure 5.24 (right) illustrates this result using  $P3/P0$  residuals. The residuals (ratio  $[(P3/P0)_{\text{mean}} - (P3/P0)_{\text{ideal}}] / [(P3/P0)_{\text{ideal}}]$ ) decrease with increasing total counts. However, even at low counts the residuals are very small (a few %). This underlines the fact that for clusters with high  $P3/P0$ , the dependence on the total counts is negligible.

Simulation A and F are two extreme cases. Simulation A yields a power ratio signal only due to noise. This effect increases for lower counts. For clusters with high initial structure like simulation F the effect of photon noise can be neglected and thus also the dependence on total counts is negligible. Apart from apparently relaxed and very disturbed clusters, our sample includes also clusters which have intermediate, but significant  $P3/P0$ , such as simulation E. Simulation E (Figure 5.25) has a disturbed core and yields significant power ratios. In this case, the dependence of the measured power ratios on the total counts is very obvious. One can clearly see that with 2 000 and 10 000 counts, the effect of photon noise is very severe, while this effect lessens higher counts. This can also be seen in Figure 5.26, where the left Figure shows  $P3/P0$  of 100 poissonised images (black lines) within an aperture radius of 100 pixels as a function of total counts. In addition, the mean  $P3/P0$  of these 100 poissonised images is shown (green line). The ideal  $P3/P0$  is indicated by the red line. For low counts, the obtained power ratios (and thus the mean) are mostly a lot higher than the real (ideal)  $P3/P0$ . At counts higher than 30 000, this effect lessens and all 100 poissonised images have similar signals. This effect is better visible in Figure 5.26 (right), where the residuals are shown. The decrease of the residuals with increasing counts is obvious. One might argue that the residuals are lower for 2 000 counts than for 10 000 counts and thus there is no real decrease. However, a residual of 6 indicates that the measured value is 6 times higher than the ideal one and while a residual of 16 is a lot more, both values are far too high to give accurate results. When increasing the total counts the residuals decrease.

The results are in agreement with the discussion about the bias (section 5.1.3). The dependence on the total counts is due to the increasing effect of photon noise when dealing with low counts images. For clusters without substructure the bias is as large as the measurement, no matter how many counts. For very structured clusters, the bias and also the dependence on the total counts is negligible. For all other clusters (clusters with moderate amounts of structure), there is a clear dependence on the total counts. Therefore, one should be careful when applying this method to low counts observations (less than 30 000 counts, where the bias can be larger than the signal).

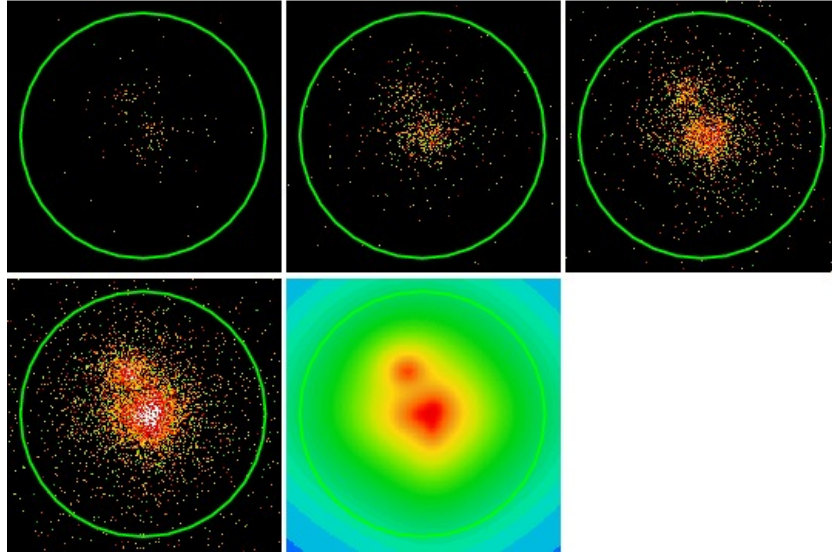


Figure 5.25: Simulation E. Poissonised images with different total counts and the ideal image. Top panel left to right:  $2 \cdot 10^3$ ,  $10^4$ ,  $3.16 \cdot 10^4$ . Bottom panel left to right:  $10^5$ , ideal image. The circles mark the aperture radius of 100 pixels.

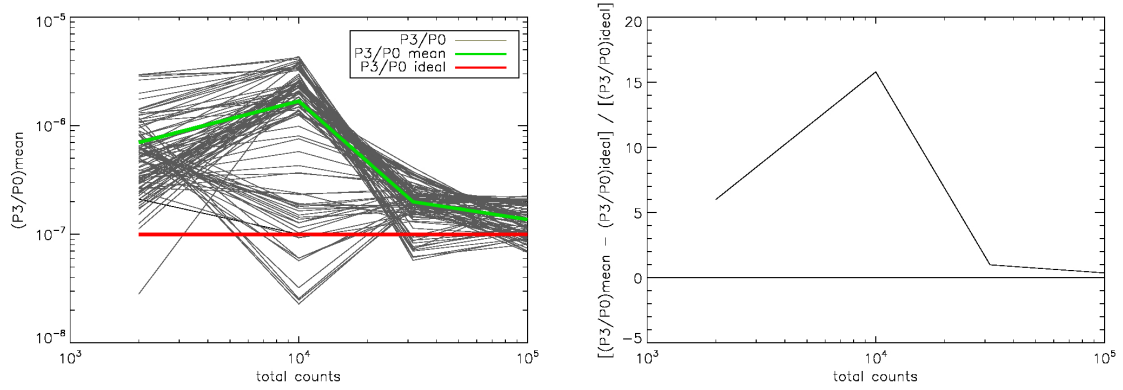


Figure 5.26: Simulation E.  $P3/P0$  of 100 poissonised images (black lines) within an aperture radius of 100 pixels as a function of total counts. In addition, the mean  $P3/P0$  of these 100 poissonised images is shown (green line). The ideal  $P3/P0$  is indicated by the red line (left).  $P3/P0$  residuals (ratio  $[(P3/P0)_{\text{mean}} - (P3/P0)_{\text{ideal}}] / [(P3/P0)_{\text{ideal}}]$ ) as a function of total counts, where 0 indicates that the ideal and noisy power ratios are the same (right).

# Chapter 6

## Results

### 6.1 Power ratios vs. cluster parameter

Cluster masses are important constraints for cosmological models. However, obtaining cluster masses is not always possible for larger number of clusters (see section 1.4). In X-rays, scaling relations are used. Such relations connect observed properties like temperature with the cluster mass. They are calibrated using well-studied and high-quality cluster samples.

At earlier times, due to lack of better information, clusters were assumed to be in hydrostatic equilibrium. Observations with better resolution revealed that a lot of clusters show structure on different scales and thus deviate from equilibrium. It is therefore important to know the implications of structure on scaling relations and more importantly their scatter. Substructure is created e.g. during the process of merging. This process is very energetic and can heat up the colliding cluster gas and boost the luminosity. Disturbed clusters could therefore have different scaling relations or at least bigger scatter around the undisturbed scaling relation. We thus investigated whether the amount of structure increases with increasing temperature, luminosity or mass, as might be expected from the current structure formation model.

In order to quantify our results, we show Figure 6.1-6.3 and obtain Spearman  $\rho$  and Kendall  $\tau$  rank correlation coefficients for the power ratios  $P2/P0$ ,  $P3/P0$  and  $P4/P0$  as a function of temperature, mass and luminosity for all 10 aperture radii ( $0.1-1 r_{500}$ ). All results are similar for the outer aperture radii ( $0.5-1 r_{500}$ ). We therefore only discuss the results for  $r_{500}$ . Table 6.2 gives the Spearman  $\rho$  and Kendall  $\tau$  rank correlation coefficient and the significance of its deviation from zero (*sig.*) for the aperture radius of  $r_{500}$ . Spearman  $\rho$  and Kendall  $\tau$  rank correlation coefficients of 1 give a 1-1 correlation and negative values an anti-correlation. Correlation coefficients below 0.5 are considered to indicate just random correlations. The second value (*sig.*) gives the significance of the deviation from zero, where a high number indicates a small significance in the correlation.

The relation between  $P3/P0$  obtained within  $r_{500}$  and temperature for REXCESS (red symbols) and the rest of the sample (black symbols) is shown in Figure 6.1. Visual inspection and both rank coefficients (given in Table 6.2) show that there is no correlation between the amount of structure and temperature. The correlation coefficient for the REXCESS subsample is higher, but still below 0.5 and therefore shows only a random correlation. This result is in agreement with previous results of Böhringer et al. (2010).



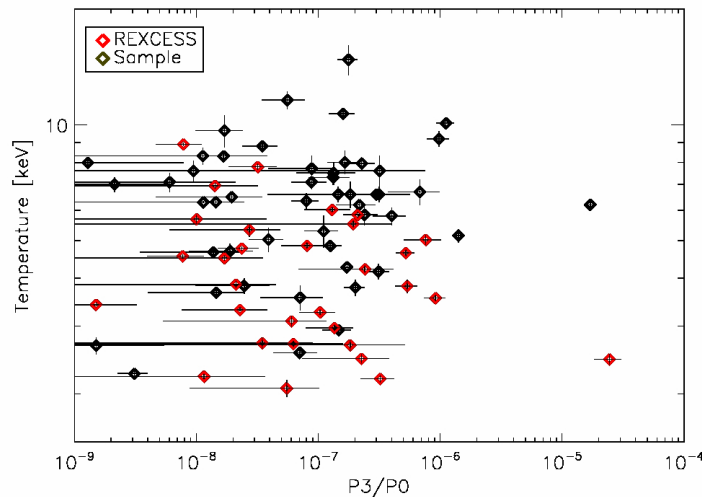


Figure 6.1: Relation between  $P3/P0$  obtained within  $r_{500}$  and temperature. Red symbols represent the REXCESS clusters, while black symbols show the rest of the sample. The errors are given for  $P3/P0$  and temperature.

When changing the X-ray temperature to luminosity, we find similar results. Figure 6.2 shows the same relation between  $P3/P0$  and luminosity for REXCESS (red symbols) and the rest of the sample (black symbols). The correlation coefficients give a hint of an anti-correlation for the REXCESS subsample, however, the correlation coefficients (-0.48 and -0.32) and the significances are very low (both 0.01). We thus agree with Böhringer et al. (2010) that the luminosity does not depend significantly on the amount of structure.

The most interesting cluster parameter is mass, because it is used to constrain cosmological models. Thinking of the hierarchical structure formation scenario, where clusters form through merging, one would expect an increase of structure for more massive clusters. Such clusters are formed through several merging events and should show features of more recent merging than smaller clusters. Theoretical  $\Lambda$ CDM studies on the growth of dark matter halos through major merging show that this effect is very mild. For different mass bins, the merger rate differs by less than 20% (Guo & White 2008). This is consistent with our results. We do not find any dependence of the amount of structure on cluster mass, as is illustrated in Figure 6.3. In this case, only LoCuSS, REXCESS and a few other clusters have known masses. Therefore, this Figure does not show all 80 clusters. The lack of a correlation between substructure and mass is expected because mass is connected with luminosity (luminosity-mass relation) and no relation was found between  $P3/P0$  and this parameter (see Figure 6.2). The luminosity-mass relation however is quite broad and thus we investigate the dependence on mass too. This independence of structure or dynamical state on the cluster mass has advantages for cosmological applications. In addition, the calibration of observable-mass relations is more reliable if the fraction of clusters in a certain dynamical state (disturbed/undisturbed) is not a strong function of mass.

We also investigate the relations between cluster parameters and power ratios for  $P2/P0$  and  $P4/P0$ . In addition to the hint of an anti-correlation between  $P3/P0$  - L, the correlation coefficients show a weak anti-correlation between  $P4/P0$  - L for REXCESS (-0.68 and -0.49) and the



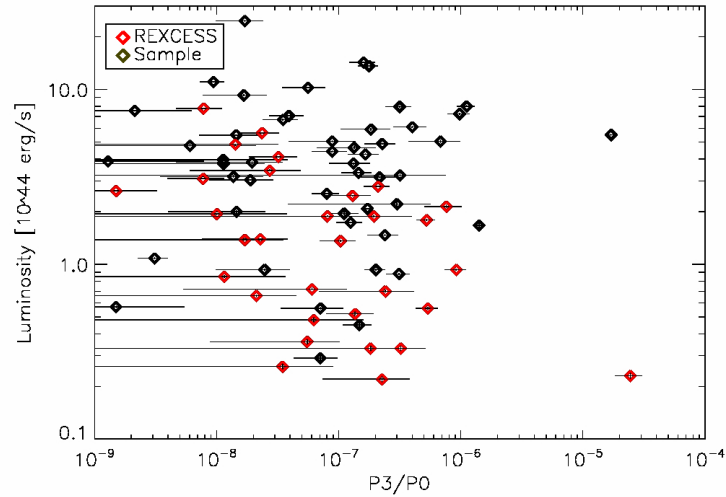


Figure 6.2: Relation between  $P3/P0$  obtained within  $r_{500}$  and luminosity. Red symbols represent the REXCESS clusters, while black symbols show the rest of the sample. The errors are given for  $P3/P0$  and luminosity.

whole sample (-0.45 and -0.32). This correlation is weak but has a high significance ( $10^{-5}$ ). The rank correlation coefficients however are obtained using only the measured data points and do not take measurement errors into account. We therefore perform a linear fit to the data in the log-log plane in order to see if the correlation holds once errors are added. Figure 6.4 shows the results. In addition to  $P4/P0$  as a function of luminosity for the REXCESS (red) and the whole sample (black), linear fits are shown. This and all other fits which will be displayed later are obtained using the linear regression method BCES (Akritas & Bershady 1996) ( $x$  and  $y$  as indicated in the figures). The fitting parameters are given in Table 6.1 for the relation  $y=10^{A+\log(x)*B}$ , using only the measured data points (NO ERRORS) and including errors (ERRORS) for the REXCESS subsample and for the whole sample of 80 clusters. In agreement with the correlation coefficients, we find an anti-correlation by performing a linear fit to the data points (BCES fit without errors). This fit to  $P4/P0$  -  $L$  however is very weak, because the errors on the fitting parameters are very large for both RECESS (red) and the whole sample (black). Once errors are included, the slope changes, however it is still within the very large errors (see Table 6.1). The correlation changes its slope when adding errors and gives poor fits. It is therefore difficult to establish a convincing significance to the correlation result.

The weak anti-correlation of power ratios with X-ray luminosity is already pointed out in previous studies (Böhringer et al. 2010). They show that there is no correlation of power ratios with mass but an anti-correlation with the occurrence of cool-cores. Cool core (CC) clusters have a brighter core and in general a higher X-ray luminosity than clusters without a cool core (NCC) at a given mass or temperature (discussed in section 6.2). In addition, CC clusters are in general more relaxed than NCC clusters. Therefore, more relaxed clusters are found at high luminosities than disturbed ones and thus a weak anti-correlation between X-ray luminosity and structure is introduced. If we remove the cores ( $0.1 r_{500}$ ) of all clusters, we remove the effect of cool cores and the correlation coefficient of  $P4/P0$  -  $L$  drops below significant values (-0.35 and -0.25).

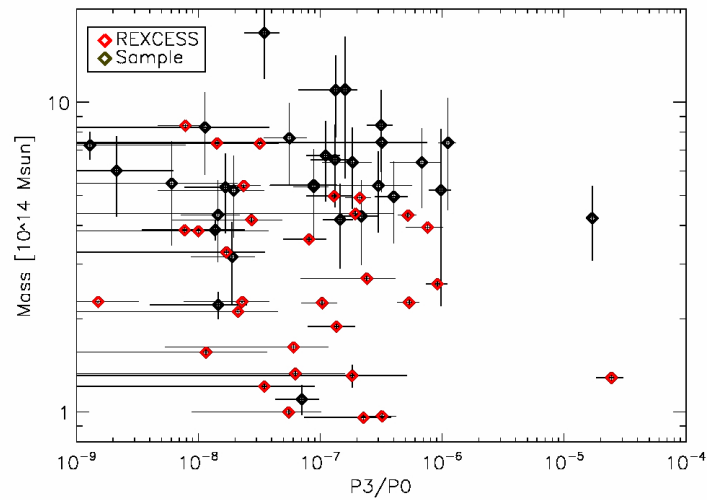


Figure 6.3: Relation between  $P3/P0$  obtained within  $r_{500}$  and cluster mass. Red symbols represent the REXCESS clusters, while black symbols show the rest of the sample. Cluster mass are only available for the LoCuSS and a few other clusters. The errors are given for  $P3/P0$  and mass.

Table 6.1: Fitting parameters for Figure 6.4: Intercept (A) and slope (B) for the relation  $y=10^{A+\log(x)*B}$  for REXCESS and the whole sample of 80 clusters. NO ERRORS indicates that measurement errors are neglected and only measurement are used for fitting. ERRORS shows the fitting parameters when using measurements and uncertainties.

	A	B
	(1)	(2)
NO ERRORS		
Sample	$-3.83 \pm 0.55$	$-0.55 \pm 0.65$
REXCESS	$-2.85 \pm 0.72$	$-0.39 \pm 0.49$
ERRORS		
Sample	$-2.89 \pm 0.52$	$-0.42 \pm 0.59$
REXCESS	$-1.85 \pm 0.52$	$-0.26 \pm 0.42$

Columns: (1) Intercept; (2) Slope for the relation  $y=10^{A+\log(x)*B}$ . The fitting parameters are obtained using the BCES fitting routine in the log-log plane. x and y as indicated in the figures.

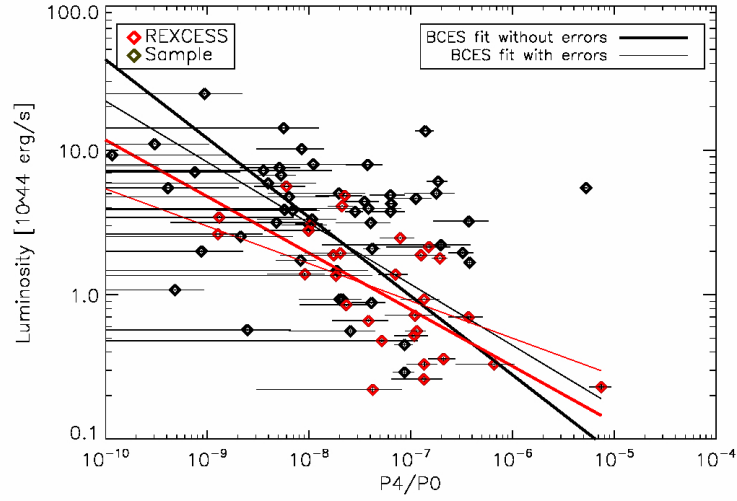


Figure 6.4: Relation between  $P4/P0$  obtained within  $r_{500}$  and luminosity. Error bars are given for  $P4/P0$  and luminosities. In addition, linear BCES fits are shown for REXCESS (red) and the whole sample of 80 clusters (black), taking only measurements (thick line) and also errors into account (thin line). The fitting parameters are given in Table 6.1.

Table 6.2: Spearman  $\rho$  and Kendall  $\tau$  rank correlation coefficient and the significance of its deviation from zero (*sig.*). The values are given for an aperture radius of  $r_{500}$ . Spearman  $\rho$  and Kendall  $\tau$  rank correlation coefficients of 1 give a 1-1 correlation and negative values an anti-correlation. Correlation coefficients below 0.5 are considered to indicate no or only very weak correlations. The second value (*sig.*) gives the significance of the deviation from zero, where a high number indicates a small significance in the correlation.

	Spearman $\rho$	<i>sig.</i>	Kendall $\tau$	<i>sig.</i>
	(1)	(2)	(3)	(4)
P2/P0 - T	-0.17	0.14	-0.10	0.17
P2/P0 - T (REXCESS)	-0.09	0.62	-0.05	0.67
P2/P0 - L	-0.24	0.03	-0.16	0.04
P2/P0 - L (REXCESS)	-0.23	0.22	-0.14	0.25
P2/P0 - M	-0.02	0.90	0.01	0.99
P2/P0 - M (REXCESS)	-0.07	0.70	-0.04	0.76
P3/P0 - T	0.01	0.96	0.10	0.96
P3/P0 - T (REXCESS)	-0.23	0.21	-0.17	0.17
P3/P0 - L	-0.13	0.26	-0.08	0.29
P3/P0 - L (REXCESS)	-0.48	0.01	-0.32	0.01
P3/P0 - M	-0.02	0.90	-0.02	0.82
P3/P0 - M (REXCESS)	-0.25	0.18	-0.18	0.16

Columns: (1) Spearman  $\rho$  rank correlation coefficient; (2) significance of its deviation from zero; (3) Kendall  $\tau$  rank correlation coefficient; (4) significance of its deviation from zero.

Table 6.2: continued.

	Spearman $\rho$ (1)	<i>sig.</i> (2)	Kendall $\tau$ (3)	<i>sig.</i> (4)
P4/P0 - T	-0.28	0.01	-0.18	0.01
P4/P0 - T (REXCESS)	-0.45	0.01	-0.31	0.01
P4/P0 - L	-0.45	$2.9 \cdot 10^{-5}$	-0.32	$2.8 \cdot 10^{-5}$
P4/P0 - L (REXCESS)	-0.68	$2.4 \cdot 10^{-5}$	-0.49	$9.6 \cdot 10^{-5}$
P4/P0 - L (core excluded)	-0.35	$1 \cdot 10^{-3}$	-0.25	$1 \cdot 10^{-3}$
P4/P0 - M	-0.07	0.53	-0.05	0.54
P4/P0 - M (REXCESS)	-0.46	0.01	-0.33	0.01

Columns: (1) Spearman  $\rho$  rank correlation coefficient; (2) significance of its deviation from zero; (3) Kendall  $\tau$  rank correlation coefficient; (4) significance of its deviation from zero.

In section 3, we discuss that the sample of 80 clusters consists of several subsamples. This means that temperatures and masses were obtained in different ways. We compare temperatures of clusters which are part of several subsamples and find that the temperatures are very similar. In order to make sure that the small difference in the data does not influence our results, we perform the following test. We increase and decrease the temperatures of the REXCESS subsample by a very conservative 20%, while all other temperatures stay the same. We then compute correlation coefficients. This test is also done for the LoCuSS and SNOWDEN subsample. In this way, we account for a 20% systematic difference in the temperatures in different subsamples. However, even such a large change in temperature does not change the fact that there are no correlations between power ratios and temperature. We thus conclude that our results are not biased by non-consistent temperature measurement and that the amount of structure does not depend on temperature and clusters mass.

## 6.2 Luminosity-Temperature and Luminosity-Mass relation

One of the most interesting application of deriving the dynamical state of a cluster is to investigate the influence of structure on X-ray scaling relations. Relations between clusters parameters like luminosity or  $Y_X$  and the cluster mass (e.g. Pratt et al. 2009) are very important tools to constraining the total mass of a cluster. Challenges in deriving the cluster mass from direct observations were discussed in section 1.4. Assumptions like hydrostatic equilibrium or spherical shape are needed to obtain masses. However, disturbed clusters are not relaxed systems and thus the assumptions made are not completely correct. It is therefore very interesting to investigate the effect of structure on scaling relations and their scatter. Apart from using power ratios, substructure can also be studied using cool-core properties or a visual classification. We discuss in previous sections that there is no significant dependence of substructure on cluster temperature, luminosity or mass. We therefore expect to find very similar scaling relations for smooth and structured clusters.

In order to quantify the modification of scaling relations by structure, we first divide the sample in cool-core (CC) and non-cool-core (NCC) clusters. This information is taken from the literature (e.g. Pratt et al. 2009, for REXCESS) and is known for about 70 cluster. We then obtain the

luminosity ratio between the luminosity within an aperture of  $r_{500}$  and the luminosity within the same aperture, but with the core ( $0.1 r_{500}$ ) excluded:

$$\text{Luminosity ratio} = \frac{L(r_{500})}{L(r_{500}) - L(0.1 r_{500})} \quad (6.1)$$

The comparison between the cool core classification and the luminosity ratio as a function of luminosity is shown in Figure 6.5. The errors on the luminosity ratio are propagated from the errors on the individual luminosities. Cool-core (red) and non-cool-core (green) clusters are displayed. There is a visual separation between high (CC) and low (NCC) luminosity ratios, therefore we conclude that the information from the literature is accurate and can be used for our further analysis. There are a few clusters which would be classified as NCC according to their luminosity ratio but are cool-core clusters according to the literature and vice versa. We investigate these objects in detail and find that their classification is accurate. In addition, their number is very small. For some clusters we do not have cool core information (black). They are located in the NCC region. They are not classified as NCC clusters in the further analysis, but one should keep in mind that they are rather NCC than CC clusters.

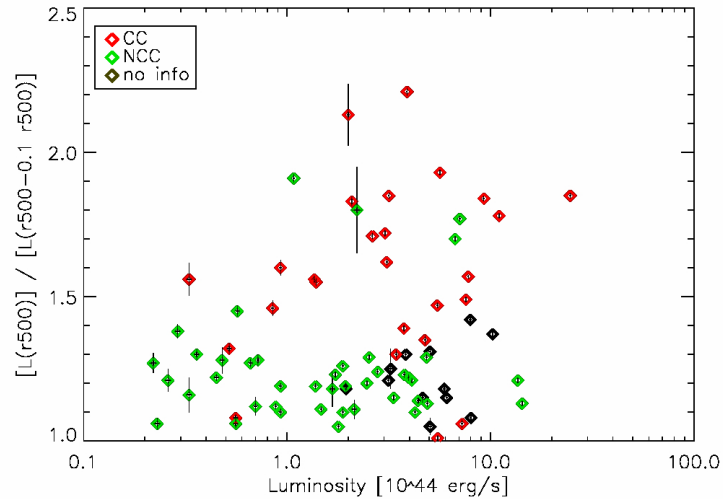


Figure 6.5: Comparison between the luminosity ratio (luminosity within an aperture of  $r_{500}$  and the luminosity within the same aperture, but with the core excluded:  $[L(r_{500})] / [L(r_{500} - 0.1 r_{500})]$ ) as a function of luminosity. The errors on the luminosity ratio are propagated from the errors on the individual luminosities. Cool-core (red) and non-cool-core (green) clusters are displayed. For some clusters we do not have cool core information (black). However, they are located in the NCC region and can be assumed to be rather NCC than CC clusters.

The luminosity-temperature (L-T) and luminosity-mass (L-M) relations are linear relations between luminosity and temperature or mass in the log-log plane. We show the L-T- and L-M-relation for our sample in Figure 6.6, including a linear fit to the data. The fitting parameters are given in Table 6.3. The fits are obtained using the BCES linear regression method in the log-log plane and the relation:  $y=10^{A+\log(x)*B}$ , where A is the intercept and B the slope in the linear fit (x and y are as indicated in the figures).

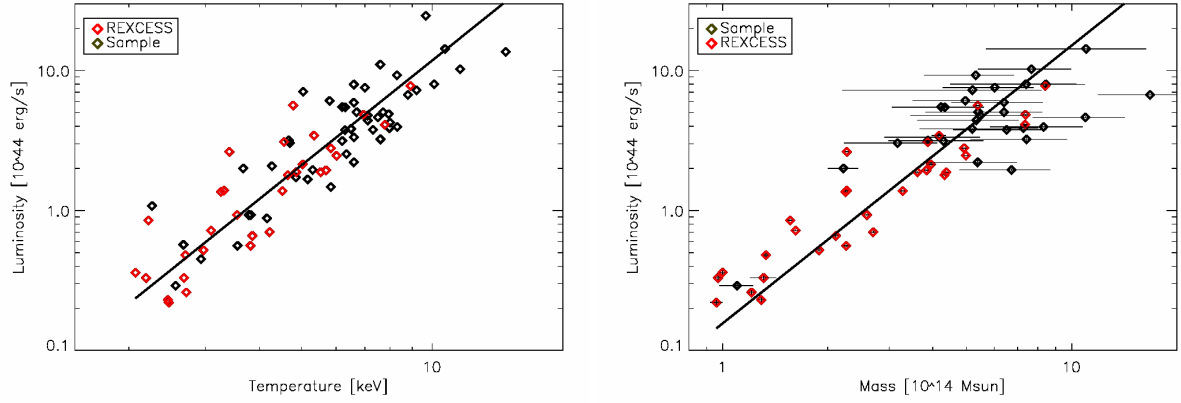


Figure 6.6: Luminosity-temperature (left) and luminosity-mass relation (right). The fits are obtained using the linear regression method BCES in the log-log plane and the relation:  $y=10^{A+\log(x)*B}$ , where A is the intercept and B the slope in the linear fit. The fitting parameters are given in Table 6.3.

Table 6.3: Fitting parameters: Intercept (A) and slope (B) for the relation  $y=10^{A+\log(x)*B}$ .

	A (1)	B (2)
L-T	$-1.41 \pm 0.10$	$2.48 \pm 0.42$
L-T (REXCESS)	$-1.46 \pm 0.13$	$2.57 \pm 1.13$
L-T (CC)	$-1.22 \pm 0.17$	$2.43 \pm 0.50$
L-T (NCC)	$-1.43 \pm 0.11$	$2.37 \pm 0.69$
L-T (undisturbed)	$-1.40 \pm 0.11$	$2.50 \pm 0.48$
L-T (disturbed)	$-1.60 \pm 0.11$	$2.56 \pm 0.90$
L-T ( $P3/P0 < 10^{-7}$ )	$-1.29 \pm 0.14$	$2.40 \pm 0.48$
L-T ( $P3/P0 > 10^{-7}$ )	$-1.55 \pm 0.11$	$2.57 \pm 0.72$
L-M	$-0.81 \pm 0.10$	$1.99 \pm 0.24$
L-M (REXCESS)	$-0.60 \pm 0.05$	$1.60 \pm 0.29$
L-M (CC)	$-0.63 \pm 0.12$	$1.73 \pm 0.27$
L-M (NCC)	$-0.69 \pm 0.07$	$1.63 \pm 0.21$
L-M (undisturbed)	$-0.69 \pm 0.08$	$1.81 \pm 0.23$
L-M (disturbed)	$-1.41 \pm 0.54$	$2.93 \pm 1.15$
L-M ( $P3/P0 < 10^{-7}$ )	$-0.59 \pm 0.09$	$1.71 \pm 0.26$
L-M ( $P3/P0 > 10^{-7}$ )	$-1.09 \pm 0.23$	$2.34 \pm 0.48$

Columns: (1) Intercept; (2) Slope for the relation  $y=10^{A+\log(x)*B}$ . The fitting parameters are obtained using the BCES fitting routine in the log-log plane. x and y as indicated in the figures.

Cool-core clusters are assumed to be rather regular clusters which are not disturbed by a recent merging event. This is not true for all clusters and therefore not all cool-core clusters can be seen as relaxed. The L-T- and L-M-relation for the CC- and NCC-subsamples are shown in Figure 6.7, including linear fits to all clusters (black line), CC (red line) and NCC (green line) clusters. In agreement with previous studies (e.g. Böhringer et al. 2010; Pratt et al. 2009), we find that CC clusters have in general a higher luminosity for a fixed temperature or fixed mass than NCC clusters. The linear fits in the log-log plane in Figure 6.7 emphasize this result, although their significance is not very high. This offset in the normalisation (similar slope but different intercept) of the L-T- and L-M-relation of CC clusters to the relation of NCC clusters indicates that in general CC clusters (rather relaxed) have a steeper L-T- and L-M-relation than NCC (rather disturbed) clusters. This however can also be explained by the enhanced central brightness of CC clusters and is not necessarily due to substructure. However, we need better statistics to better understand these results.

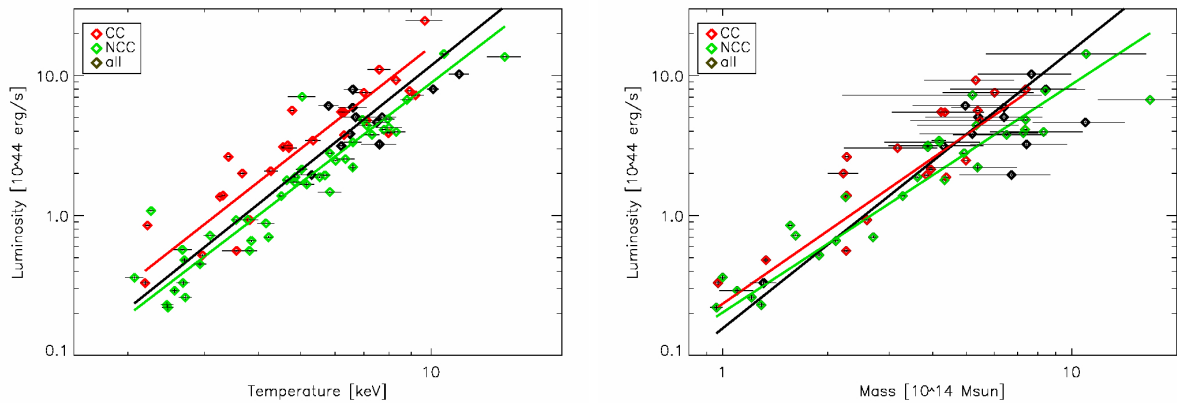


Figure 6.7: L-T- (left) and L-M- (right) relation for CC (red) and NCC (green) clusters. For some clusters we do not have cool core information (black). However, they are located in the NCC region and can be assumed to be rather NCC than CC clusters.

Another way to study the influence of morphology on the L-T- and L-M-relation is to divide the cluster sample into disturbed and undisturbed clusters. This classification is done first by the overall visual appearance of the cluster and then using P3/P0. The core properties are not well resolved and are not taken into account. This classification is therefore done independently of the cool core classification. We perform the same analysis using visual classification and show the results in Figure 6.8. As in the CC/NCC case, the linear fits for disturbed and undisturbed clusters are very similar to each other and the statistics are poor. Most clusters are classified as undisturbed (no apparent structure) and thus the fit for the disturbed sample is very weak. However, the general trend that undisturbed clusters have higher luminosities for a given temperature and mass seems to hold. This trend is more pronounced for cool-core properties (small scale properties) than for the overall (large-scale) visual appearance of the cluster. This indicates that the inner core properties are more important for the overall scaling relations than the global cluster properties.

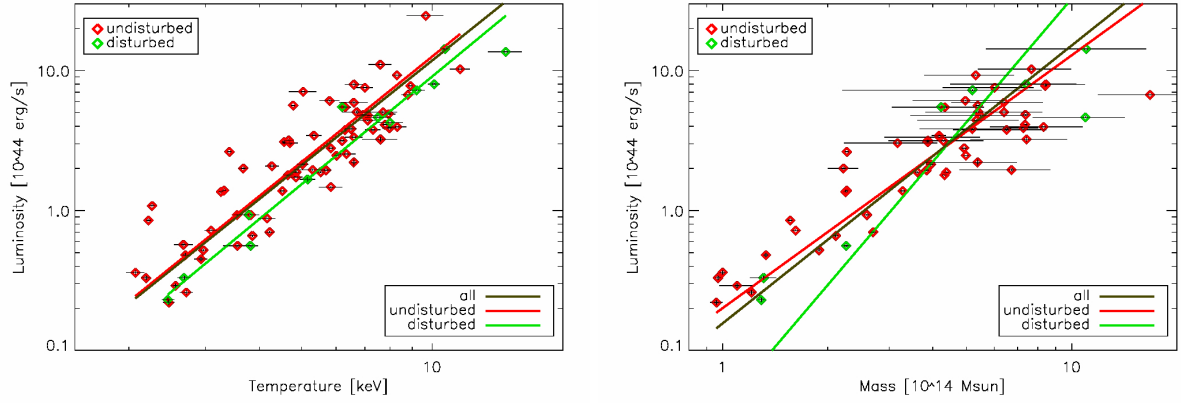


Figure 6.8: L-T- (left) and L-M-relation (right) for undisturbed (red) and disturbed (green) clusters. The clusters are classified by eye. The classification is given in Table 6.10 in the Appendix.

At last we divide the sample into disturbed and undisturbed objects using power ratios. Disturbed clusters have  $P3/P0 > 10^{-7}$ , while undisturbed ones have lower  $P3/P0$ . In this case, the uncertainties in the  $P3/P0$  calculations need to be taken into account. We obtain very similar results to the disturbed/undisturbed classification by eye because in both cases the global cluster appearance was used to divide the sample. The general trend that the linear fits to disturbed (green), undisturbed (red) and all clusters are very similar holds (Figure 6.9). Again, undisturbed clusters ( $P3/P0 < 10^{-7}$ ) seems to have higher luminosities at a given temperature and mass.

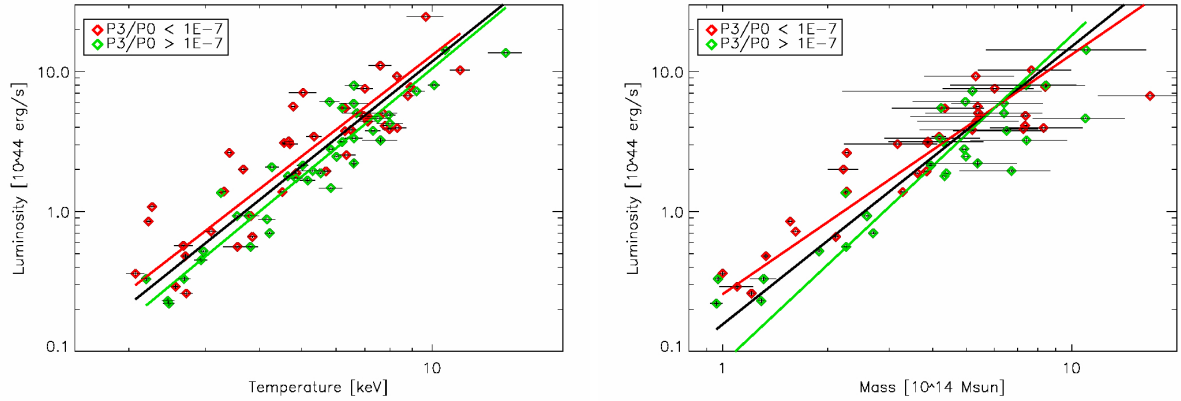


Figure 6.9: L-T- (left) and L-M-relation (right) for undisturbed (red) and disturbed (green) clusters. The clusters were classified using power ratios. Undisturbed clusters have power ratios  $P3/P0 < 10^{-7}$ , while disturbed clusters have  $P3/P0 > 10^{-7}$ . The classification is given in Table 6.10 in the Appendix.

We thus conclude that undisturbed clusters, no matter if classified by their cool-core properties, by eye or using the  $P3/P0$ , tend to have higher luminosities at a given temperature or mass than unrelaxed clusters. This finding is more pronounced when dividing the sample using inner



core properties (CC/NCC), than when using the global cluster appearance or its dynamical state. Better statistics are needed to underline these results, but if we trust what is indicated here, the dynamical state of a cluster is not as important as the properties of the core for the scaling relations. This is in agreement with O'Hara et al. (2006) and our findings that there is no correlation between cluster properties and the dynamical state (amount of substructure). Concerning the scatter around those relations, we would assume that disturbed clusters are more scattered around the scaling relation. However, we do not find any clear evidence. In any case, better statistics are needed to confirm this suspicion.

### 6.3 Mean and $\sigma$ vs. cluster parameter

In section 5.2 we explore the use of combined power ratios of several apertures and the use of the mean and the standard deviation  $\sigma$ . Therefore, we investigate the relation between the mean of the power ratios obtained in eight aperture radii ( $0.3-1 r_{500}$ ) and cluster parameter.

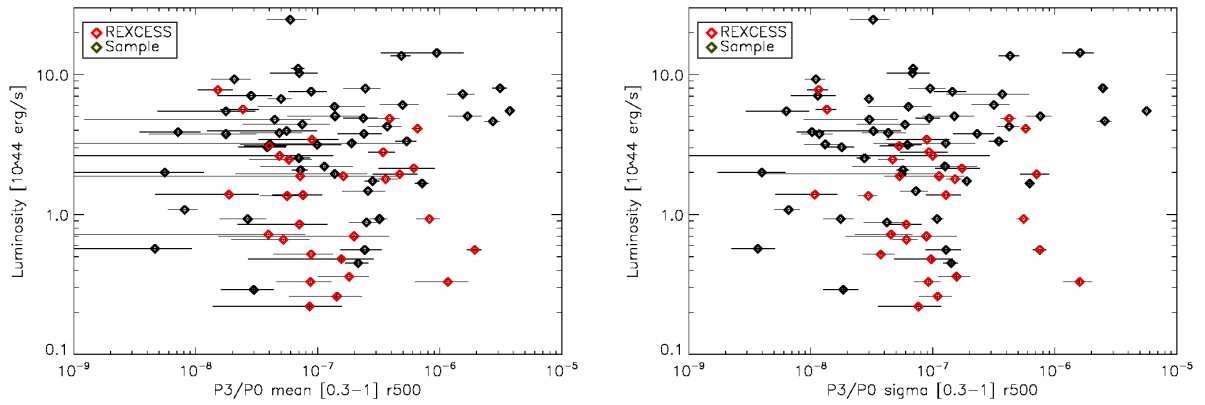


Figure 6.10: Relation between the mean (left) and standard deviation  $\sigma$  (right) of P3/P0 obtained within eight apertures ( $0.3-1 r_{500}$ ) and luminosity. Red symbols represent the REXCESS clusters, while black symbols show the rest of the sample.

The mean and  $\sigma$  of several apertures have the advantage that these properties are less sensitive to a single aperture size. Clusters can be divided more easily into disturbed and undisturbed using several apertures (see section 6.4.3). In case of a physical correlation between cluster properties and the morphology, one would expect a stronger trend using the mean and  $\sigma$ . However, all our findings are in agreement with section 6.1 that the morphology (amount of structure) does not depend on cluster properties.

In order to display these results, we always show the comparison between using the mean and the  $\sigma$  of eight aperture radii for these relations. Figure 6.10 shows the X-ray luminosity as a function of the mean (left) and  $\sigma$  (right) of P3/P0 of eight aperture radii. We obtain a correlation coefficient for the relation between P3/P0 and luminosity which indicates a weak anti-correlation. However, we do not see any hint of an anti-correlation with the mean or the  $\sigma$  of P3/P0 (see Table 6.4). If there was a correlation between the amount of structure and luminosity, it should be even more obvious when using the mean and  $\sigma$ , however the anti-correlation is weaker.

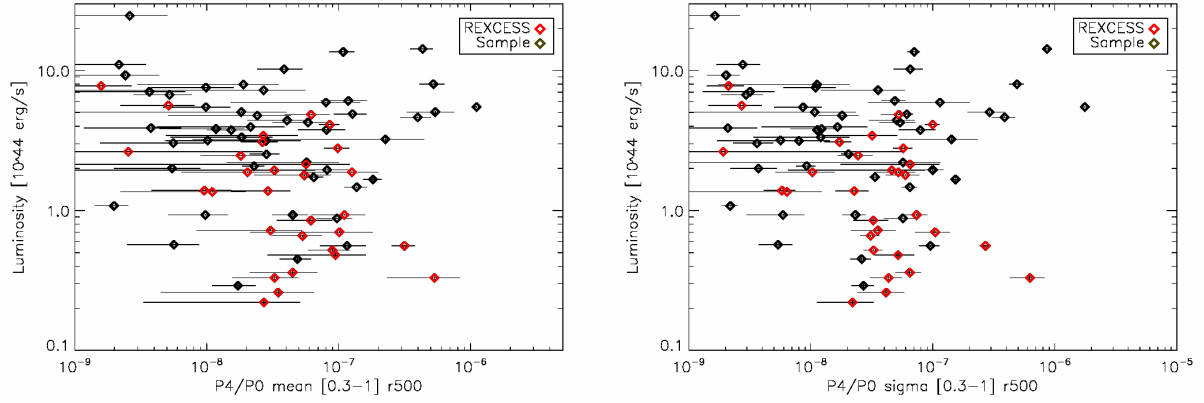


Figure 6.11: Relation between the mean (left) and standard deviation  $\sigma$  (right) of  $P4/P0$  obtained within eight apertures ( $0.3-1 r_{500}$ ) and luminosity. Red symbols represent the REXCESS clusters, while black symbols show the rest of the sample.

In section 6.1 we found a weak but significant correlation between  $P4/P0$  and luminosity using correlation coefficients. However, this relation did not hold when adding measurement errors and linear fits. When using the mean and  $\sigma$  (Figure 6.11), the mean errors are smaller. The obtained correlation coefficients (Table 6.4) do not indicate any correlation at all. As mentioned before, in case of a real correlation between the amount of structure and luminosity, this correlation should be stronger when using the mean or  $\sigma$ , however the correlation is weaker.

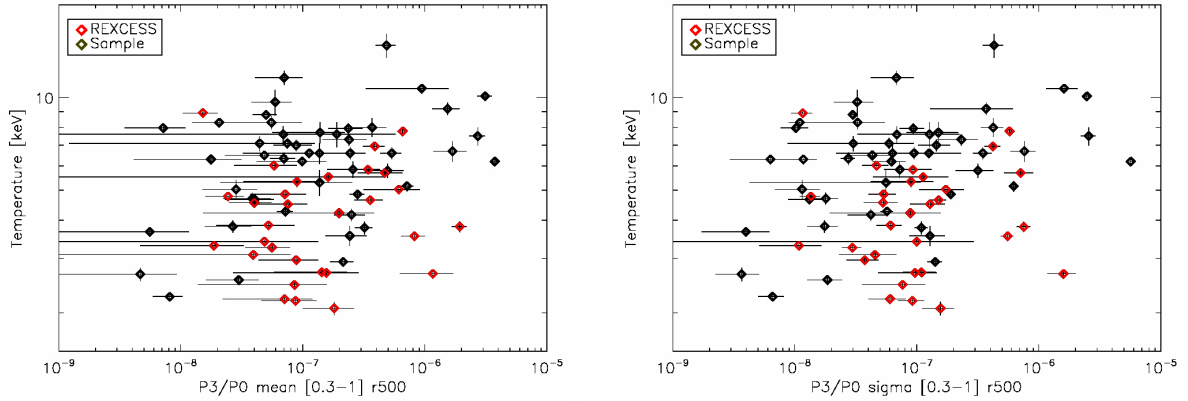


Figure 6.12: Relation between the mean (left) and standard deviation  $\sigma$  (right) of  $P3/P0$  obtained within eight apertures ( $0.3-1 r_{500}$ ) and temperature. Red symbols represent the REXCESS clusters, while black symbols show the rest of the sample.

In addition, we show the relation between  $P3/P0$  and temperature (Figure 6.12) and mass (Figure 6.13). The correlation coefficients are given in Table 6.4, but do not indicate any correlation. These results therefore confirm our conclusion of section 6.1, in which we state that there is no dependence of power ratios on physical parameters.

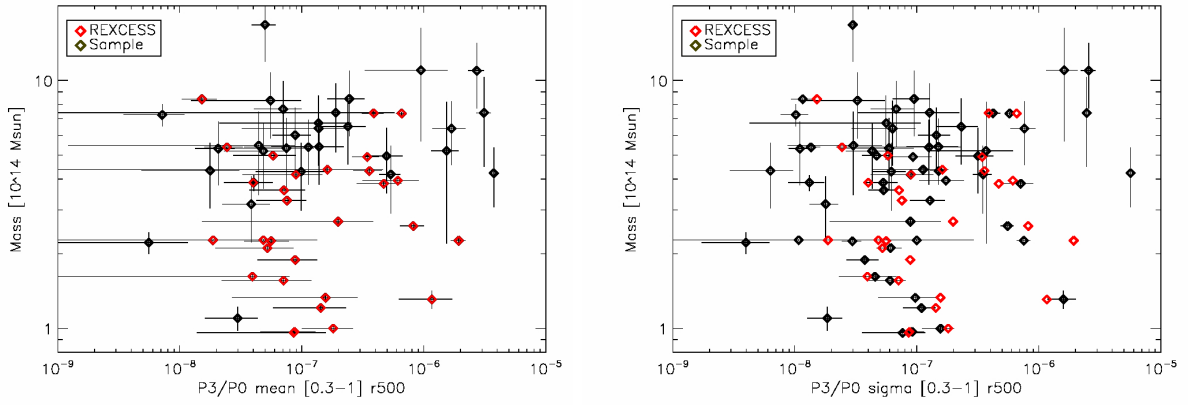


Figure 6.13: Relation between the mean (left) and standard deviation  $\sigma$  (right) of P3/P0 obtained within eight apertures (0.3-1  $r_{500}$ ) and mass. Red symbols represent the REXCESS clusters, while black symbols show the rest of the sample.

Table 6.4: Spearman  $\rho$  and Kendall  $\tau$  rank correlation coefficient and the significance of its deviation from zero (*sig.*). The values are given for the mean and the standard deviation  $\sigma$  of eight aperture radii: 0.3-1  $r_{500}$ . Spearman  $\rho$  and Kendall  $\tau$  rank correlation coefficients of 1 give a 1-1 correlation and negative values an anti-correlation. Correlation coefficients below 0.5 are considered to indicate no or only very weak correlations. The second value (*sig.*) gives the significance of the deviation from zero, where a high number indicates a small significance in the correlation.

	Spearman $\rho$	<i>sig.</i>	Kendall $\tau$	<i>sig.p</i>
	(1)	(2)	(3)	(4)
P2/P0 - T mean	0.10	0.40	0.07	0.33
P2/P0 - T $\sigma$	0.20	0.07	0.15	0.06
P2/P0 - L mean	-0.02	0.85	-0.02	0.83
P2/P0 - L $\sigma$	0.08	0.45	0.06	0.43
P2/P0 - M mean	0.11	0.33	0.08	0.29
P2/P0 - M $\sigma$	0.20	0.07	0.14	0.06
P3/P0 - T mean	0.14	0.22	0.09	0.22
P3/P0 - T $\sigma$	0.13	0.24	0.10	0.20
P3/P0 - L mean	-0.25	0.17	-0.01	0.95
P3/P0 - L $\sigma$	0.01	0.96	-0.1	0.99
P3/P0 - M mean	0.1	0.4	0.07	0.38
P3/P0 - M $\sigma$	-0.09	0.65	0.09	0.22
P4/P0 - T mean	-0.01	0.94	-0.01	0.96
P4/P0 - T $\sigma$	0.04	0.72	0.02	0.76
P4/P0 - L mean	-0.2	0.08	-0.14	0.07

Columns: (1) Spearman  $\rho$  rank correlation coefficient; (2) significance of its deviation from zero; (3) Kendall  $\tau$  rank correlation coefficient; (4) significance of its deviation from zero.

Table 6.4: continued.

	Spearman $\rho$	<i>sig.</i>	Kendall $\tau$	<i>sig.</i>
	(1)	(2)	(3)	(4)
P4/P0 - L $\sigma$	-0.15	0.17	-0.11	0.15
P4/P0 - M mean	0.04	0.75	0.02	0.77
P4/P0 - M $\sigma$	-0.13	0.48	0.09	0.23

Columns: (1) Spearman  $\rho$  rank correlation coefficient; (2) significance of its deviation from zero; (3) Kendall  $\tau$  rank correlation coefficient; (4) significance of its deviation from zero.

## 6.4 Morphological classification

### 6.4.1 Classification by Buote & Tsai (1996) - method

Buote & Tsai (1995) introduced the power ratio method as a tool to characterize clusters according to their projected morphologies and to estimate the clusters dynamical state. As is already discussed in section 5, the method is based on a multipole expansion of the projected gravitational potential, which is traced by the surface brightness in X-rays. The obtained power ratios are thus directly related to large-scale fluctuations in the gravitational potential. Clusters with a high amount of structure (high power ratios) are thus considered to be very disturbed, while low power ratios indicate relaxed clusters. According to Buote & Tsai (1996), their position in the power ratio plane shows their dynamical state. Buote & Tsai (1996) find the tightest relation between power ratios in the P2/P0 - P4/P0 plane, because these two power ratios measure structure in a similar way. Disturbed clusters have high P2/P0 and P4/P0, while undisturbed ones will be located on the other side of the P2/P0 - P4/P0 plane. Buote & Tsai (1996) show this plane for eight reference clusters for an aperture of  $1h_{80}^{-1}$  Mpc (Figure 6.14 left). The clusters on the upper right are dynamically young objects. With time they evolve dynamically and pass through several morphological stages. They start in their dynamical youth as double clusters (A1750), if they are formed through merging of equal-sized clusters. With time such clusters virialise and can be observed as highly elongated clusters (A2142) with an offset center, then as highly elongated (A545) and finally as smooth, regular clusters (A2029). However, the starting point can also be a cluster like A514, a very complex cluster with several small substructures. Over time they become less complex (A2382). Before virialising and forming a regular cluster, they can be observed as one cluster with a small secondary surface brightness peak (A85). However, in both scenarios, dynamically young clusters start out in the upper right of Figure 6.14 (left) and evolve to regular clusters which are located in the lower left.

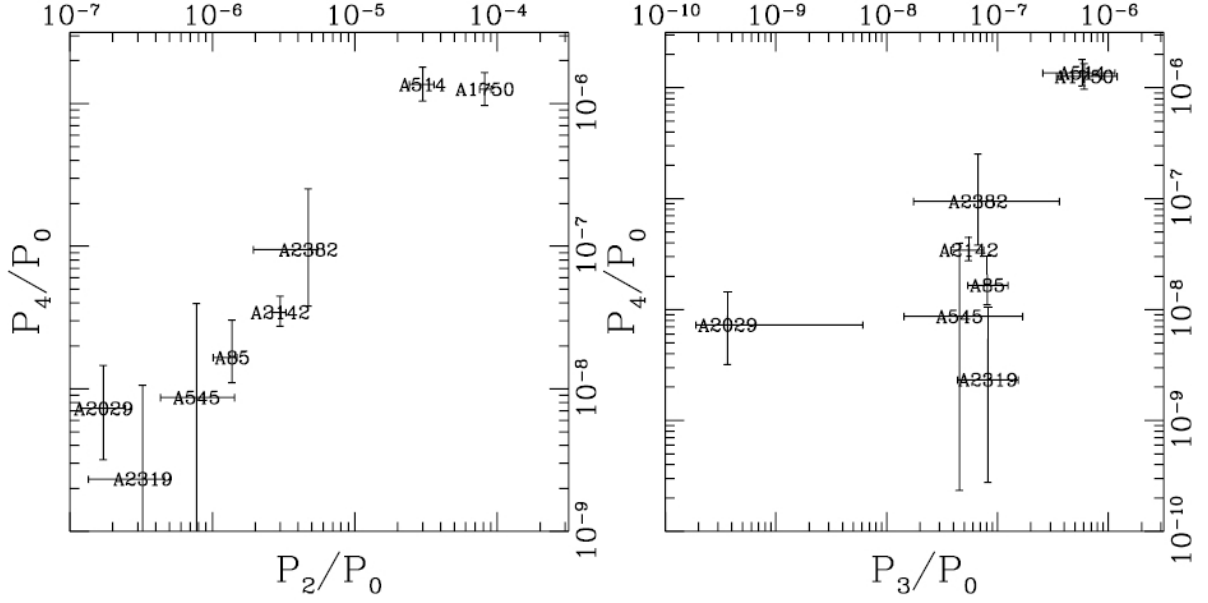


Figure 6.14: Power ratios of eight "reference clusters" obtained for an aperture of  $1h_{80}^{-1}$  Mpc.  $P_2/P_0$  -  $P_4/P_0$  plane including errors. This relation is seen as *evolutionary track* (left).  $P_3/P_0$  -  $P_4/P_0$  plane for the same clusters including errors (right). Source: Buote & Tsai (1996).

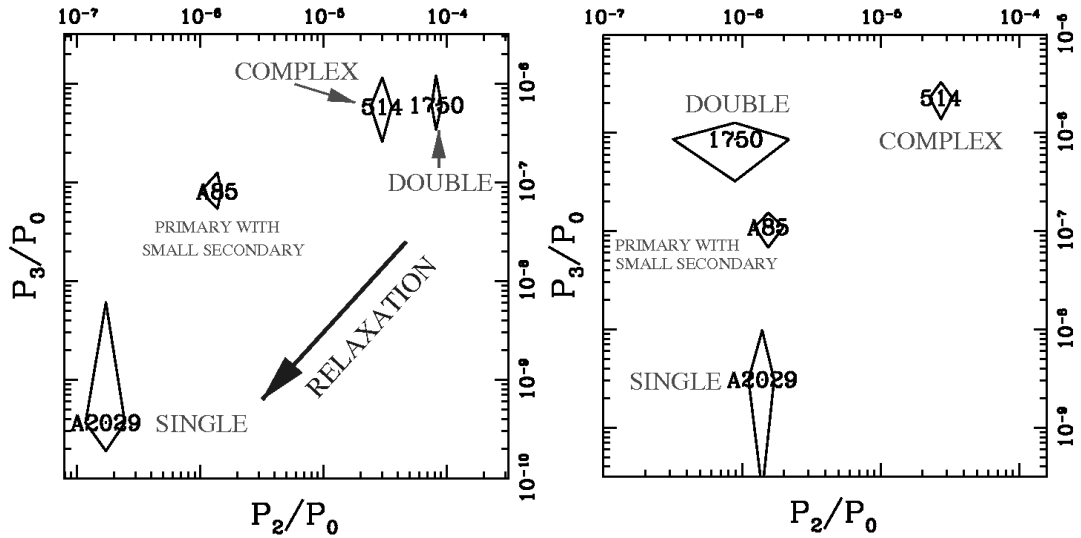


Figure 6.15: Power ratios for different morphologies (displayed in Figure 6.16) in the  $P_2/P_0$  -  $P_3/P_0$  plane. The power ratios were computed within an aperture of  $1 h_{80}^{-1}$  (left) and  $0.5 h_{80}^{-1}$  (right). Source: Buote & Tsai (1996).

The P3/P0 - P4/P0 plane can be interpreted in a similar way. Figure 6.14 (right) shows the P3/P0 - P4/P0 relation for these eight clusters. The two very disturbed clusters (A1750 and A514) are located in the upper right of the Figure, while the others are more scattered around the 1-1 relation. Also in this plane, the trend of evolving from the upper right to the lower left is obvious for those eight clusters. At last, Buote (2002) discusses the P2/P0 - P3/P0 plane. Figure 6.15 shows the location of different morphologies in the P2/P0 - P3/P0 plane for two different apertures:  $1h_{80}^{-1}$  Mpc (left) and  $0.5h_{80}^{-1}$  Mpc (right). The four different morphologies are shown in Figure 6.16. The separation of the complex and double cluster and the more regular primary with small secondary peak and single cluster is apparent and supports the theory of an evolutionary track for an aperture of  $1h_{80}^{-1}$  Mpc. For a smaller aperture (Figure 6.15 right) the location of the double cluster changes. This is due to the fact that in this aperture only one subcluster is enclosed. The dependence of the obtained power ratio on the aperture size is already established (section 5.2). Buote (2002) thus recommends to use an aperture of  $0.5h_{80}^{-1}$  Mpc to better distinguish between morphologies. However, as is established in section 5.2, a fixed aperture size can only be used if the redshift and mass ( $r_{500}$ ) range is small.

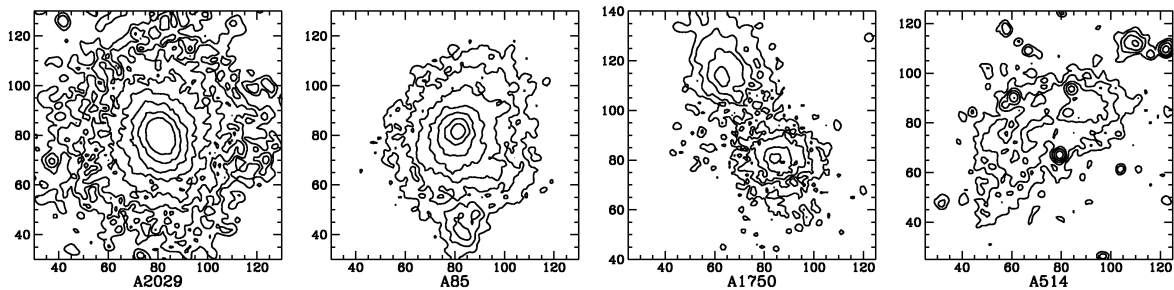


Figure 6.16: Morphological classification by Buote (2002). Left to right: Single, Primary with small secondary, Double, Complex cluster. Source: Buote (2002).

#### 6.4.2 Classification by Buote & Tsai (1996) - application to data

Buote & Tsai (1996) use only eight clusters for their detailed discussion. This classification works very well for their selected "reference clusters". Buote (2002) shows the P2/P0 - P3/P0 plane for  $\sim 40$  ROSAT clusters and finds a deficiency of highly disturbed (double and complex) clusters. In addition, the four distinct morphologies are not separated anymore. We thus test this morphological scheme with our sample of 80 clusters and visually divide them into four subgroups: single, primary with small secondary, double and complex. This is done for two apertures:  $0.5$  and  $1 r_{500}$  to enable comparison with the results of Buote & Tsai (1996) and Buote (2002).

Figure 6.17 shows the P2/P0 - P3/P0 plane for 80 clusters. In addition, Table 6.10 in the Appendix gives the classification for each cluster. Figure 6.17 shows this plane for both apertures ( $0.5$  and  $1 r_{500}$ ). The results fit quite well to the theoretical prediction (location of clusters in the diagram). Figure 6.17 (left) shows the relation for an aperture of  $1 r_{500}$ . A double (A115) and a complex cluster can be found in the upper right, as predicted by the theory. Other complex clusters are found in the upper right part of the diagram, but less separated from the single clusters. However, some complex clusters and also the bullet cluster (classified as a double cluster) are located in the cloud of single clusters. Also, a lot of single clusters have higher P2/P0 and P3/P0 than the ones classified as primary with small secondary. For a smaller aperture of

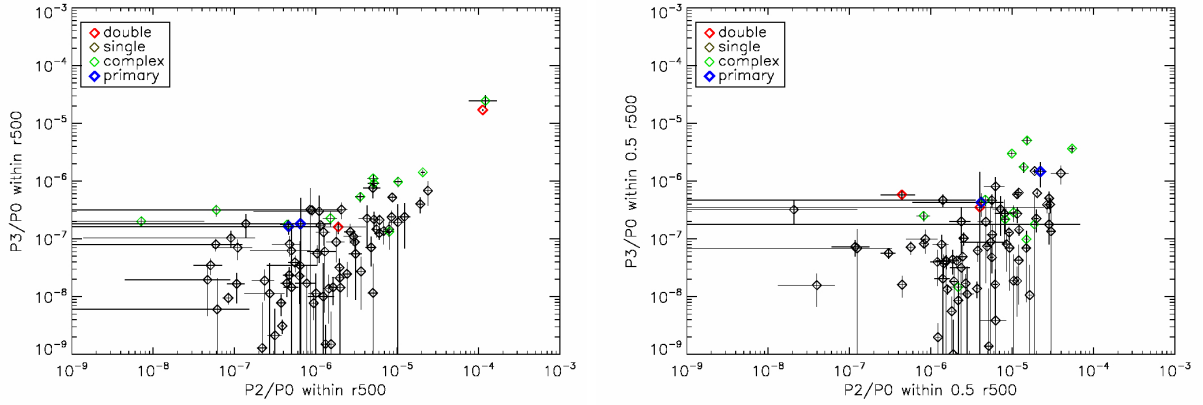


Figure 6.17: Power ratios for different morphologies (displayed in Figure 6.16) in the  $P2/P0$  -  $P3/P0$  plane. The power ratios were computed within an aperture of 1 (left) and  $0.5 r_{500}$  (right) for the sample of 80 clusters. The morphological classification is shown in Table 6.10 in the Appendix.

$0.5 r_{500}$  (Figure 6.17 right), one double cluster (A115) behaves as predicated and moves to the left. However, all three other subgroups are more entwined. We do see the trend that complex and double cluster accumulate at the upper right and that double clusters change their position (move to the left) for smaller apertures. In the case of A115 only the main cluster was enclosed when using an aperture of  $0.5 r_{500}$  and it moved to the left in the  $P2/P0$  -  $P3/P0$  plane. For this aperture size, the bullet cluster is still a double cluster and thus does not change its position. This shows that it depends on the size of the subcluster whether a double cluster changes its position in the  $P2/P0$  -  $P3/P0$  plane when using smaller apertures or not.

We do not think that such a classification works for each individual cluster, but it can be used in a statistical way for cluster samples. We agree with the trend that clusters start dynamically young in the upper right (high power ratios) in any power ratio diagram and later evolve to the lower left (low power ratios). Classification for each individual cluster however is not possible with a method like this. We thus suggest to use the mean or standard deviation  $\sigma$  of several apertures. In this case, we use eight apertures ( $0.3-1 r_{500}$ ). The clearer separation of the disturbed and undisturbed clusters when using the mean and  $\sigma$  is shown in Figure 6.18. Clusters are morphologically classified the same way as in Figure 6.17, but this time not the individual power ratios, but the mean (left) and the  $\sigma$  (right) of eight apertures are shown.

For both cases (mean and  $\sigma$ ), the  $P2/P0$  -  $P3/P0$  relation becomes tighter. In addition, the disturbed clusters (double, complex and primary with small secondary) are more separated from the single clusters. The few disturbed clusters which still overlap with the undisturbed ones can be considered as transition objects. We thus conclude that a clear classification for each cluster using power ratios is not possible. This is partly due to the fact that the bias due to photon noise could not be estimated sufficiently accurate yet. In addition, we know from simulations that the same cluster seen from different directions gives different results (Böhringer et al. 2010). Thus also the method has its limits. However, the method improved significantly by using the mean and  $\sigma$  and has more statistical power than when using only one aperture. In addition, samples can be divided into disturbed and undisturbed clusters with some transition objects and statistical results can be obtained. This is discussed in the next section.

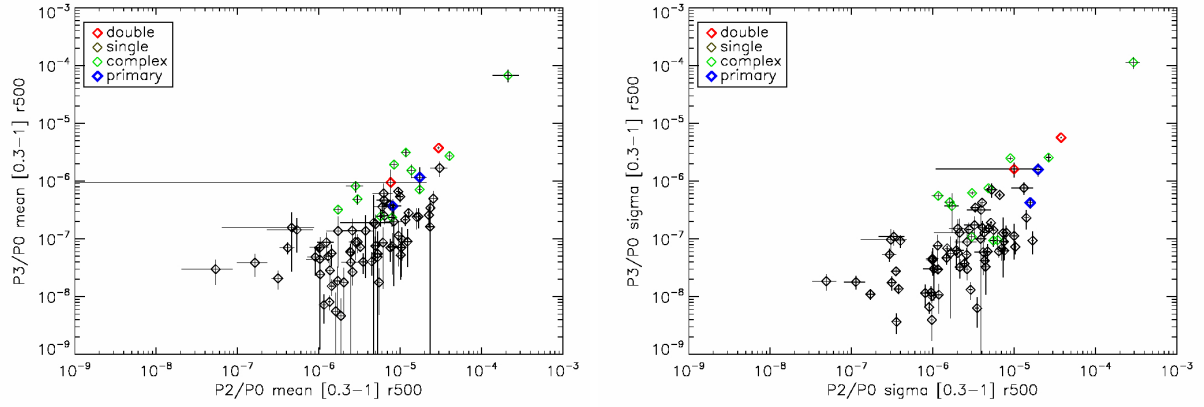


Figure 6.18: Mean (left) and  $\sigma$  (right) of power ratios obtained within eight aperture radii 0.3-1  $r_{500}$ . The different morphologies (displayed in Figure 6.16) are shown in the  $P2/P0$  -  $P3/P0$  plane for the sample of 80 clusters. The morphological classification is shown in Table 6.10 in the Appendix.

### 6.4.3 Classification using mean and $\sigma$

The quality of the data is not good enough to clearly classify every cluster according to its power ratios, because the errors in the measurement are too large. However, dividing them into disturbed and undisturbed clusters seems possible. The errors shown in the plots are mean errors of the eight apertures.

The classification is done by eye and is given in Table 6.10 in the Appendix for each cluster. Clusters which show signs of merging, several surface brightness peaks or irregular structure are classified as disturbed clusters. Undisturbed clusters have a regular shape (circular or elliptical). Figure 6.19 shows the  $P2/P0$  -  $P3/P0$  plane for disturbed and undisturbed clusters. The separation of the two subgroups (disturbed - red, undisturbed - black) in the  $P2/P0$  -  $P3/P0$  plane is visible, however the overlap is apparent and the errors quite large.

In order to make the separation between the two subgroups more visible, we use the mean  $P2/P0$  and  $P3/P0$  of eight apertures (0.3-1  $r_{500}$ ) and repeat the analysis. The results are shown in Figure 6.20. The separation of the two groups is a lot more distinct than in case of a single aperture radius (Figure 6.19). In addition, the relation is tighter. An even bigger improvement is using the standard deviation  $\sigma$  of the eight apertures (Figure 6.21). The two subgroups are very clear. The disturbed cluster located in the "undisturbed" cloud is RXCJ0014.3-3022. This big cluster has an infalling small subcluster. It is thus clearly a transition object between a double cluster and a relaxed single cluster.



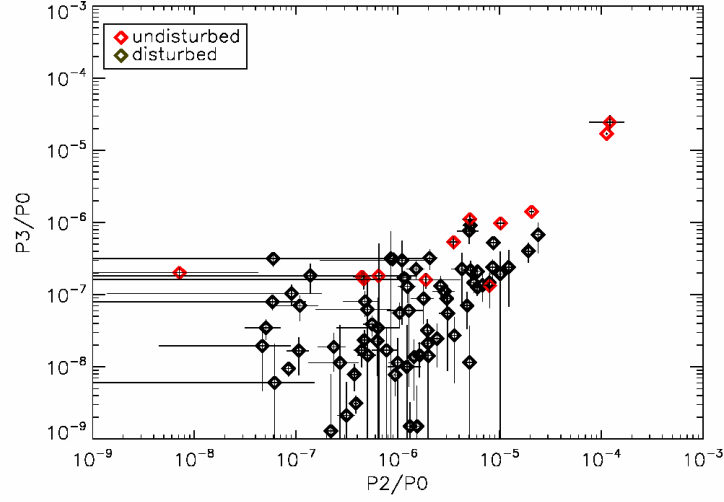


Figure 6.19: Power ratios for different morphologies (disturbed and undisturbed) in the  $P2/P0$  -  $P3/P0$  plane. Disturbed clusters are shown as red diamonds, while undisturbed ones are displayed as black diamonds. The power ratios are computed within an aperture of  $1 r_{500}$  for the sample of 80 clusters. The morphological classification is shown in Table 6.10 in the Appendix.

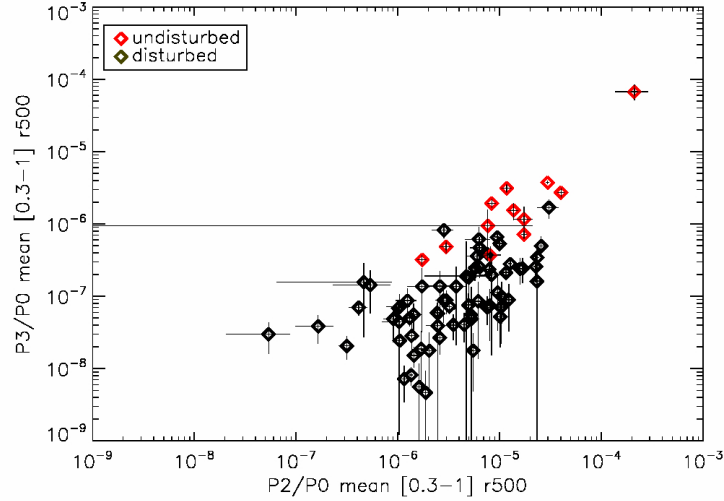


Figure 6.20: Mean of power ratios obtained within eight aperture radii  $0.3-1 r_{500}$  for different morphologies (disturbed and undisturbed) in the  $P2/P0$  -  $P3/P0$  plane. Disturbed clusters are shown as red diamonds, while undisturbed ones are displayed as black diamonds. The power ratios are computed within an aperture of  $1 r_{500}$  for the sample of 80 clusters. The morphological classification is shown in Table 6.10 in the Appendix.

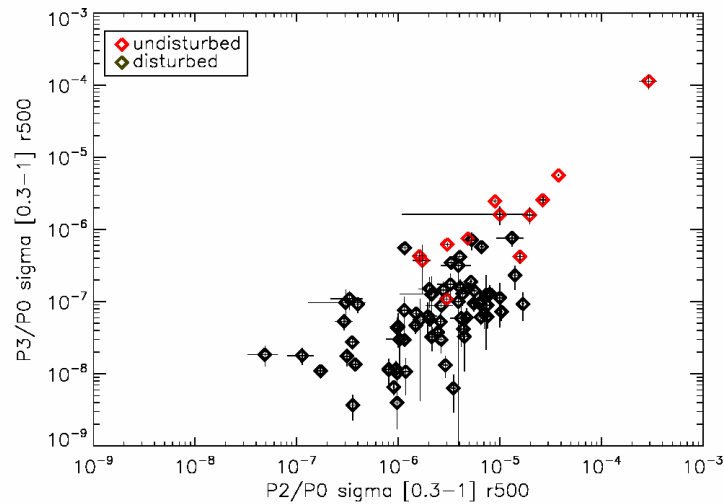


Figure 6.21: Standard deviation  $\sigma$  of power ratios obtained within eight aperture radii 0.3-1  $r_{500}$  for different morphologies (disturbed and undisturbed) in the P2/P0 - P3/P0 plane. Disturbed clusters are shown as red diamonds, while undisturbed ones are displayed as black diamonds. The power ratios are computed within an aperture of 1  $r_{500}$  for the sample of 80 clusters. The morphological classification is shown in Table 6.10 in the Appendix.

To complete the analysis, we investigate the P2/P0 - P4/P0 and P3/P0 - P4/P0 plane. As results we show the power ratios and the  $\sigma$  of eight power ratios. The improvement in the separation is clearly visible in Figure 6.22 for the P2/P0 - P4/P0 plane and in Figure 6.23 for the P3/P0 - P4/P0 plane.

As long as the errors on the power ratio measurements are as large as they are right now, a clear classification of each individual cluster cannot be achieved. The most important issue is that the real bias due to photon noise, which spuriously introduces or smooths out structure, cannot be quantified with sufficient accuracy. However, obtaining power ratios in several aperture sizes and combining them (mean and  $\sigma$ ) enables us to clearly divide big cluster samples into disturbed and undisturbed clusters.

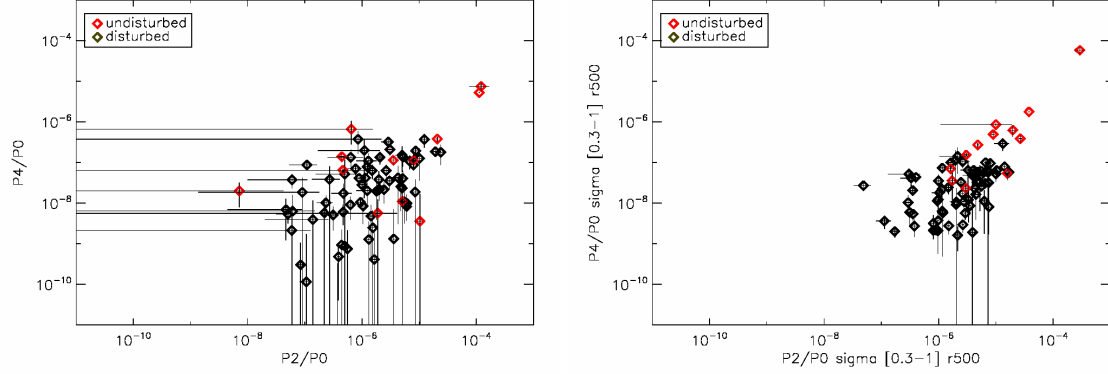


Figure 6.22: Power ratios for different morphologies (disturbed and undisturbed) in the  $P2/P0$  -  $P4/P0$  plane. The power ratios are computed within an aperture of  $1 \text{ } r_{500}$  (left). Standard deviation  $\sigma$  of power ratios obtained within eight aperture radii  $0.3-1 \text{ } r_{500}$  (right). Disturbed clusters are shown as red diamonds, while undisturbed ones are displayed as black diamonds. The morphological classification is shown in Table 6.10 in the Appendix.

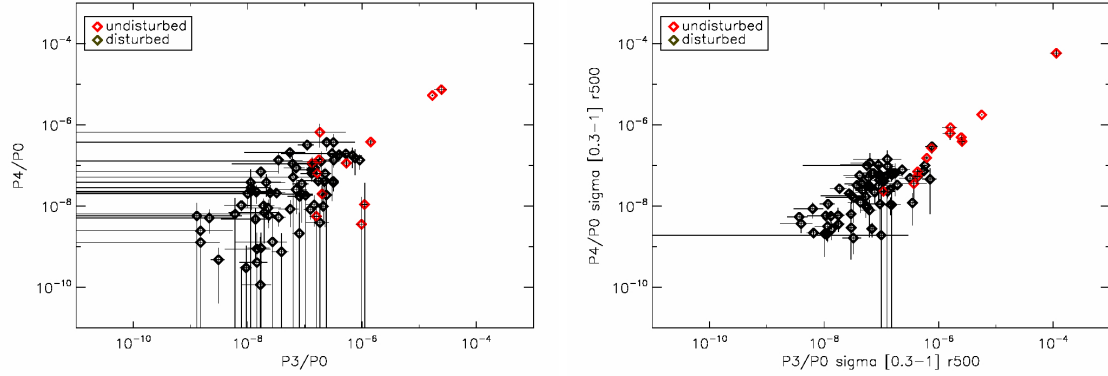


Figure 6.23: Power ratios for different morphologies (disturbed and undisturbed) in the  $P3/P0$  -  $P4/P0$  plane. The power ratios are computed within an aperture of  $1 \text{ } r_{500}$  (left). Standard deviation  $\sigma$  of power ratios obtained within eight aperture radii  $0.3-1 \text{ } r_{500}$  (right). Disturbed clusters are shown as red diamonds, while undisturbed ones are displayed as black diamonds. The morphological classification is shown in Table 6.10 in the Appendix.

## 6.5 Application for high-redshift cluster

With the advance of X-ray telescopes, the number of detected high-redshift clusters increases. It is therefore interesting to find out whether the power ratio method can be applied to those clusters. When dealing with high-redshift clusters, two main problems occur. The apparent cluster size on the detector decreases with increasing distance. Due to the instrumental resolution limit, very distant clusters are not as well resolved as those close by. This leads to larger uncertainties in measuring structure and can be solved by using the X-ray telescope CHANDRA<sup>1</sup>. CHANDRA has an about 10 times better angular resolution than XMM-Newton and is thus as suitable for distant clusters ( $z > 0.5$ ) as XMM-Newton is for nearby clusters. However, CHANDRA has only one X-ray telescope and thus the number of photons is very small. With increasing distance, also the number of photons arriving at the detector plane decreases. Exposure times are limited and thus, the total counts of high-redshift clusters are often only around  $10^3$  counts. Longer exposure times increase this number but such deep observations are very rare. Using CHANDRA would indeed solve the resolution problem, however the number of total counts would only be around 2 000 counts and thus well below the 30 000 counts threshold.

We therefore investigate how the power ratio method depends on the total counts. This is discussed in detail in section 5.3. It is shown that the method is not reliable below 30 000 total counts, unless the cluster has a lot of structure (high initial  $P3/P0$ ). This unreliability due to low counts can be compensated by using a much larger cluster sample and thus improve the statistics. The results would still be unreliable for an individual cluster, but the behaviour and trends of ensembles can be investigated and yield statistically significant results. However, such a large sample is not available at the point of our analysis. We thus do not recommend to use the power ratio method for high-redshift clusters without significant structure at this point. The most important improvement which needs to be done is the treatment of the bias. We explore several methods but we do not find a consistent way to model and subtract the bias. Once this is accomplished, we will perform another study and we plan to improve it so that the method can be applied to high-redshift clusters. This investigation is especially important when thinking of future X-ray telescopes. They will find and observe thousands of new clusters. Such a big sample would enhance the statistics significantly. However, the issue of the bias-estimation needs to be solved or at least better understood to obtain accurate and reliable results.

---

<sup>1</sup><http://chandra.harvard.edu/>

# Conclusions

Substructure in clusters of galaxies can be investigated in several ways. In this work, we test a very popular substructure characterisation method called power ratios and methods to estimate the bias and measurement errors. We then apply power ratios to a sample of 80 galaxy clusters and investigate the relation between the amount of substructure and physical properties.

Our findings concerning the power ratio method can be summarized as follows:

- We develop a method to simulate multiple-component elliptical  $\beta$  model cluster images and study the effect of poisson noise on the power ratios using a range of toy and realistic cluster models.
- We test a bias- and an error estimation method proposed by Böhringer et al. (2010) and find that the bias estimation method does not work as intended. We however agree with the proposed procedure to estimate measurement uncertainties.
- We find that the bias due to photon noise is not easy to characterise. The bias decreases for increasing total counts and for increasing structure. We test different methods to quantify those findings, including the possibility of calibrating a relation between the measured  $P3/P0$ , the unbiased (ideal)  $P3/P0$  and the total counts. However, the bias depends too much on the individual cluster structure. Therefore more work is needed to solve this issue. We also investigate the possibility of bias correction by smoothing the image before calculating power ratios. We obtain best results with the *contbin* method, however the improvements are not sufficient to obtain a reliable bias correction.
- Taking the findings about the bias into account, we conclude that a good unbiased measurement can be only obtained for observations with more than  $\sim 30\,000$  counts or high  $P3/P0$ . This is especially important for high-redshift clusters which do not have such high counts.

We apply the power ratio method to 80 galaxy cluster observations and conclude:

- After compiling a sample of 80 clusters from the literature, we process archival observations of all clusters and improved the method of removing point sources obtaining excellent quality images. In addition, we measure luminosities in the 0.5-2 keV energy band and calculate power ratios for all clusters in a consistent way. Our sample contains power ratios and errors for 80 high-quality observations. It is thus the largest sample for this kind of substructure study.
- We investigate the relation between  $P3/P0$  and luminosity, temperature and mass. We do not find a correlation with temperature and mass, but a hint of a correlation with luminosity. We show that this difference is caused mainly by the presence of cool cores.

- We classify the clusters morphology according to different independent criteria (cool core properties (CC/NCC), visual (undisturbed/disturbed) and P3/P0) and investigate the L-T- and L-M-relation. We do agree with previous studies that CC clusters have higher luminosities at a given temperature or mass than NCC clusters. However we do not find any significant difference in the slope and intercept of the scaling relations between globally relaxed and unrelaxed clusters.
- We classify the clusters (single, double, primary with small secondary, complex cluster) according to Buote & Tsai (1995) and test their morphological classification with power ratios. We see a trend of the reported *evolutionary track*, however not as strong as predicted and can only be used as a rough classification.
- We investigate the dependence of the power ratios on the aperture radius and found that the classification can be improved by using the mean and standard deviation ( $\sigma$ ) of the P3/P0 of eight apertures.
- Using the mean and  $\sigma$  we tested the relation between substructure and physical properties but do not find any correlations.
- This work gives several new insights on the power ratio method and its bias and proposes recipes to improve the method (e.g. the use of the mean or  $\sigma$  of several aperture radii). The next step is to provide a more precise calibration of the bias using simulations with much better statistics.

# Outlook

Clusters of galaxies are well-studied objects. Nonetheless there are still a lot of open question concerning these structures. Cluster parameters like mass are used to constrain cosmological parameters and need to be known as accurately as possible. In most cases, hydrostatic equilibrium is assumed to obtain masses e.g. from X-ray observations. However a lot of clusters show substructure and are thus not relaxed. It is therefore very important to study the implication of structure on X-ray scaling relation and the cluster mass. We make a step in this direction by using the power ratio method to quantify the dynamical state of a clusters and investigating the implications on X-ray scaling relations. However, this method needs refinement. We discuss the issue of the bias due to photon noise in detail. Especially low counts observations suffer from this effect, which cannot be fully quantified yet.

eROSITA, the extended ROentgen Survey with an Imaging Telescope Array, should be launched in 2012 and will be the successor of X-ray satellites like XMM-Newton or CHANDRA. With this advance in technology, tens of thousands of new cluster will be found. For this vast number of clusters, a simple method to quantify the morphology and the dynamical state is needed. Such a method is the power ratio method. It is easy to apply and gives the fraction of disturbed to undisturbed clusters. Individual classification is not necessary in such big samples, but an overall picture can be obtained. Concerning the scaling relations, the statistics will be improved a lot with a sample of a few thousand high-quality observations. Due to its large point-spread-function (PSF) and low counts for high-redshift observations, we can only safely apply the power ratio method to a small fraction ( $\sim 1\ 000$ ) of all high-redshift clusters found by eROSITA. For deep follow-up observations of high redshift clusters, the X-ray telescope CHANDRA can be used. CHANDRA has an about 10 times better angular resolution than XMM-Newton. It is thus better to apply the power ratio method to high-redshift CHANDRA observations than to high-redshift XMM-Newton observations. However, CHANDRA has only one X-ray telescope and thus the number of photons is very small.

With the method we discuss in this work, only a fraction of the high-redshift clusters can be used for analysis, because 30 000 or more counts are needed. In the future, we hope to obtain observations of a few hundred up to thousand galaxy clusters. This number can be increased if the bias can be quantified in a consistent way. Therefore we plan to use several hundred hydrodynamical simulations of galaxy clusters to test the power ratio method in even more detail than in this work. We make a step in refining the method by introducing the mean and the  $\sigma$  of several aperture radii, however this approach is very simple and can be improved. Apart from a clearer picture of the influence of noise, we hope to find a connection between the power ratios and the deviation from hydrostatic equilibrium. Once this is achieved, we can investigate the influence of the violation of hydrostatic equilibrium in estimating the cluster mass.

The most important and most interesting question regarding substructure of clusters is whether substructure increases with redshift. From the hierarchical structure formation scenario we expect clusters to be more disturbed at higher redshifts. This question can be answered using power ratios. However, a large sample of both nearby and high-redshift clusters is needed. Regarding nearby clusters, a large number is already known and thousands of new clusters will be found by eROSITA. This will improve the statistics significantly. At present however, only a few high-redshift clusters are known. Increasing the number and knowledge of high-redshift clusters is a key mission for the cluster community, especially at MPE in Garching, Germany. We are thus looking forward to the near future, when the power ratio method and especially the bias will be better understood and can be applied to new, extremely large samples.



# Bibliography

- Abell, G. O. 1958, ApJS, 3, 211
- Akritas, M. G. & Bershadsky, M. A. 1996, ApJ, 470, 706
- Arnaud, M., Pointecouteau, E., & Pratt, G. W. 2005, A&A, 441, 893
- Arnaud, M., Pratt, G. W., Piffaretti, R., et al. 2009, ArXiv e-prints: 0910.1234
- Böhringer, H. & Hensler, G. 1989, A&A, 215, 147
- Böhringer, H., Pratt, G. W., Arnaud, M., et al. 2010, A&A, 514, A32+
- Böhringer, H., Schuecker, P., Guzzo, L., et al. 2004, A&A, 425, 367
- Böhringer, H., Schuecker, P., Pratt, G. W., et al. 2007, A&A, 469, 363
- Briel, U. G., Henry, J. P., Schwarz, R. A., et al. 1991, A&A, 246, L10
- Buote, D. A. 2002, in *Astrophysics and Space Science Library*, Vol. 272, *Merging Processes in Galaxy Clusters*, ed. L. Feretti, I. M. Gioia & G. Giovannini, 79–107
- Buote, D. A. & Tsai, J. C. 1995, ApJ, 452, 522
- Buote, D. A. & Tsai, J. C. 1996, ApJ, 458, 27
- Carroll, B. W. & Ostlie, D. A. 2006, *An introduction to modern astrophysics and cosmology* (Institute for Mathematics and Its Applications)
- Cavaliere, A. & Fusco-Femiano, R. 1976, A&A, 49, 137
- Cavaliere, A. & Fusco-Femiano, R. 1978, A&A, 70, 677
- Croston, J. H., Arnaud, M., Pointecouteau, E., & Pratt, G. W. 2006, A&A, 459, 1007
- Diaferio, A. & Geller, M. J. 1997, ApJ, 481, 633
- Fabian, A. C., Crawford, C. S., Edge, A. C., & Mushotzky, R. F. 1994, MNRAS, 267, 779
- Fabricant, D. G., Kent, S. M., & Kurtz, M. J. 1989, ApJ, 336, 77
- Fassbender, R. 2008, ArXiv e-prints: 0806.0861
- Felten, J. E., Gould, R. J., Stein, W. A., & Woolf, N. J. 1966, ApJ, 146, 955
- Finoguenov, A., Reiprich, T. H., & Böhringer, H. 2001, A&A, 368, 749

- Grebel, E. K. 2001, in *Astronomical Society of the Pacific Conference Series*, Vol. 239, *Microlensing 2000: A New Era of Microlensing Astrophysics*, ed. J. W. Menzies & P. D. Sackett, 280
- Guo, Q. & White, S. D. M. 2008, *MNRAS*, 384, 2
- Haarsma, D. B., Leisman, L., Donahue, M., et al. 2010, *ApJ*, 713, 1037
- Jeltema, T. E., Canizares, C. R., Bautz, M. W., & Buote, D. A. 2005, *ApJ*, 624, 606
- Jeltema, T. E., Hallman, E. J., Burns, J. O., & Motl, P. M. 2008, *ApJ*, 681, 167
- Jones, C. & Forman, W. 1984, *ApJ*, 276, 38
- Jones, C. & Forman, W. 1991, in *Bulletin of the American Astronomical Society*, Vol. 23, 1338+
- Jones, C. & Forman, W. 1999, *ApJ*, 511, 65
- King, I. 1962, *AJ*, 67, 471
- Kolokotronis, V., Basilakos, S., Plionis, M., & Georgantopoulos, I. 2001, *MNRAS*, 320, 49
- McMillan, S. L. W., Kowalski, M. P., & Ulmer, M. P. 1989, *ApJS*, 70, 723
- Mitchell, R. J., Culhane, J. L., Davison, P. J. N., & Ives, J. C. 1976, *MNRAS*, 175, 29P
- Mohr, J. J., Evrard, A. E., Fabricant, D. G., & Geller, M. J. 1995, *ApJ*, 447, 8
- Mohr, J. J., Fabricant, D. G., & Geller, M. J. 1993, *ApJ*, 413, 492
- Navarro, J. F., Frenk, C. S., & White, S. D. M. 1995, *MNRAS*, 275, 720
- Navarro, J. F., Frenk, C. S., & White, S. D. M. 1996, *ApJ*, 462, 563
- Navarro, J. F., Frenk, C. S., & White, S. D. M. 1997, *ApJ*, 490, 493
- Neumann, D. M. & Böhringer, H. 1997, *MNRAS*, 289, 123
- O'Hara, T. B., Mohr, J. J., Bialek, J. J., & Evrard, A. E. 2006, *ApJ*, 639, 64
- Plionis, M. 2002, *ApJ*, 572, L67
- Pratt, G. W., Arnaud, M., Piffaretti, R., et al. 2010, *A&A*, 511, A85+
- Pratt, G. W., Croston, J. H., Arnaud, M., & Böhringer, H. 2009, *A&A*, 498, 361
- Sanders, J. S. 2006, *MNRAS*, 371, 829
- Schindler, S. & Diaferio, A. 2008, *Space Science Reviews*, 134, 363
- Schuecker, P., Böhringer, H., Reiprich, T. H., & Feretti, L. 2001, *A&A*, 378, 408
- Shore, S. N. 2002, *The Tapestry of Modern Astrophysics* (Wiley-VCH)
- Simionescu, A., Werner, N., Böhringer, H., et al. 2009, *A&A*, 493, 409
- Snowden, S. L., Mushotzky, R. F., Kuntz, K. D., & Davis, D. S. 2008, *A&A*, 478, 615

- Strüder, L., Briel, U., Dennerl, K., et al. 2001, *A&A*, 365, L18
- Sunyaev, R. A. & Zeldovich, Y. B. 1970, *Ap&SS*, 7, 3
- Sunyaev, R. A. & Zeldovich, Y. B. 1972, *Comments on Astrophysics and Space Physics*, 4, 173
- Werner, N., Durret, F., Ohashi, T., Schindler, S., & Wiersma, R. P. C. 2008, *Space Science Reviews*, 134, 337
- Zhang, Y., Böhringer, H., Finoguenov, A., et al. 2006, *A&A*, 456, 55
- Zhang, Y., Finoguenov, A., Böhringer, H., et al. 2008, *A&A*, 482, 451
- Zwicky, F. 1933, *Helvetica Physica Acta*, 6, 110
- Zwicky, F. 1937, *ApJ*, 86, 217



# List of Figures

1.1	Local group of galaxies. Source: Grebel (2001). . . . .	5
1.2	Optical (left) and XMM-Newton Image (right) of the Coma cluster of galaxies including point sources. Source: U. Briel/MPE (left); Snowden/MPE (right). . .	6
1.3	ROSAT Image of the Virgo cluster including point sources. Source: Snowden/MPE.	7
1.4	Uhuru satellite in preflight checks. Source: NASA. . . . .	8
1.5	Radiative cooling rate coefficient as a function of temperature. Contribution of different elements to the radiative cooling coefficient (left). Combined RGS 1 <sup>st</sup> - and 2 <sup>nd</sup> -order spectrum of the core of the galaxy cluster Hydra A (right). Source: Böhringer & Hensler (1989) (left), Simionescu et al. (2009) (right). . . . .	10
1.6	Composite Image of galaxy cluster 1E 0657-56, also known as the "bullet cluster". In the optical wavelength individual galaxies and stars are seen (white). The ICM of the merging clusters can be seen as two red clouds, while the dark matter distribution is displayed in blue. While the ICM clouds are interacting, the dark matter halos pass by undisturbed. Source: X-ray: NASA/CXC/CfA/M.Markevitch et al.; Optical: NASA/STScI, Magellan/U.Arizona/D.Clowe et al.; Lensing Map: NASA/STScI, ESO WFI, Magellan/U.Arizona/D.Clowe et al. . . . .	13
1.7	Examples of disturbed cluster morphologies. A665 (left), A3921 (middle), Cygnus A (right). . . . .	14
2.1	CCDs of the MOS (left) and pn camera (right). Source: ESA. . . . .	15
2.2	Light path with the MOS (left) and pn (right) camera in focus (not to scale). Source: XMM-Newton Users Handbook V2.7. . . . .	16
2.3	Geometry of the MOS1 (left), MOS2 (middle) and pn (right) CCDs. Source: XMM-Newton Users Handbook V2.7. . . . .	16
2.4	Quantum efficiency of the MOS CCDs (left) and pn detector (right). Source: ESA (left) and Strüder et al. (2001) (right). . . . .	17
3.1	Redshift distribution of the sample. The overlaid filled histogram represents the REXCESS subsample. . . . .	20
3.2	Temperature (left) and luminosity (right) distribution of the sample. The overlaid filled polygons represent the REXCESS subsample. . . . .	20
3.3	Histogram of counts (left), Histogram of total exposure time (right). The solid line indicates the mean values of the sample of 80 clusters. . . . .	21
3.4	Cumulative histogram of the total number of counts after cleaning and combination of all three detectors. The solid line indicates the mean of the sample. . . . .	21
3.5	Comparison of different subsamples. blue asterisk: REXCESS, red diamonds: LoCuSS, black crosses: Rest of the sample. L-T relation (left), L-M relation (right). . . . .	22
3.6	Comparison between REXCESS and LoCuSS temperatures . . . . .	22

3.7	Comparison between the three temperature provided by Pratt et al. (2009). The histograms show $(T - T_{\text{used}})/T_{\text{used}} \cdot 100$ . Filled histogram (thin line): $[0.15-1] r_{500}$ . Thick line: $[0.15-0.75] r_{500}$ . . . . .	25
4.1	100 second-binned pn (left) and MOS1 (right) light curve in the hard X-ray band at 12-14 keV. . . . .	28
4.2	Count-level histograms after the first (left) and second (right) cleaning stage in the hard (left) and soft (right) X-ray band. . . . .	29
4.3	Result of the first cleaning stage: 10 second-binned pn light curve (left). Final result after both cleaning stages: 100 second-binned pn light curve (right). . . . .	29
4.4	EPIC pn image including point sources selected by <i>ewavelet</i> and <i>ewavdetect</i> (left) and after visual inspection (right). . . . .	30
4.5	Background models. Top panel: EPIC pn (left), MOS1 (right). Bottom panel: MOS2 (left), Combination of all three detectors (right). . . . .	31
4.6	Point source corrected pn image (left) and combined image of all three detectors (right). . . . .	32
5.1	Ideal images without any noise for simulated clusters. Left to right, top panel: simulation A, B, C; bottom panel: simulation D, E. The circles indicate the aperture radius of 66 pixels for simulation A-E. . . . .	36
5.2	Images of simulated clusters with Poisson noise added. Left to right, top panel: simulation A, B, C; bottom panel: simulation D, E. The circles indicate the aperture radius of 66 pixels for simulation A-E. . . . .	36
5.3	Left: Observed cluster image. Middle: modelled, ideal cluster image. Right: poissonised image. Top panel: A1775 and simulation H. Bottom panel: A115 and simulation F. The circles mark the aperture radius of $r_{500}$ for the real cluster and of 100 pixels for the simulations. . . . .	37
5.4	P3/P0 - P4/P0 plane with the sample of 80 observed clusters (black) including REXCESS (red) and the mean of 100 poissonised images for seven simulated clusters (green) and $3.16 \cdot 10^4$ total counts. . . . .	39
5.5	Simulation A: P3/P0 derived in different aperture radii ( $0.1-1 r_{500}$ ) for 10 poissonised images with 300 000 total counts (black lines) and the ideal model (red line) without photon noise (left). Comparison between 10 poissonised images (black lines) and the mean P3/P0 of 100 poissonised images (red line) (right). The values are given as a ratio of $[P3/P0]/[(P3/P0)_{\text{mean}}]$ , where $(P3/P0)_{\text{mean}}$ is the mean of 100 poissonised simulations. . . . .	40
5.6	Simulation F: P3/P0 derived in different aperture radii ( $0.1-1 r_{500}$ ) for 10 poissonised images with 100 000 total counts (black lines) and the ideal model (red line) without photon noise (left). Ratio $[P3/P0]/[(P3/P0)_{\text{ideal}}]$ as a function of aperture radius (right). This illustrates that sometimes negative biases ( $P3/P0 < (P3/P0)_{\text{ideal}}$ ) are found. . . . .	40
5.7	P3/P0. Comparison between the real bias due to photon noise and the computed B09-bias using 100 poissonised images of each simulation and a constant exposure map. The total counts are $3 \cdot 10^5$ . . . . .	42
5.8	Comparison between the real bias due to photon noise and the computed B09-bias using 100 poissonised images of each simulation and a constant exposure map. Left: P2/P0, Right: P4/P0. The total counts are $3 \cdot 10^5$ . . . . .	42

5.9	Ratio $[(B09-bias)_{\text{mean}}]/[\text{real bias}]$ as a function of the mean P3/P0 of 100 poissonised images for simulation A-E. The black line indicates a ratio of 1, where the B09- and real bias are the same. . . . .	43
5.10	Simulation H. Histogram of P3/P0 distribution of 100 poissonised images of the model cluster for different total counts within the image. 1 000 counts (thin line histogram) and for 100 000 counts (filled histogram). In addition, the mean P3/P0 of 100 poissonised images is given for 1 000 (dotted line), 2 000 (dashed line), 3 160 (dashed-dotted line) and 10 000 total counts (dash-dot-dotted line). . . . .	44
5.11	Simulation F. Histogram of P3/P0 distribution of 100 poissonised images of the model cluster for different total counts within the image. 1 000 counts (thin line histogram) and for 100 000 counts (filled histogram). In addition, the mean P3/P0 of 100 poissonised images is given for 1 000 (dotted line) total counts is given. . .	45
5.12	Comparison between P3/P0 after the first poissonisation of the ideal model (P3/P0 of mean- $\sigma$ , mean, mean+ $\sigma$ ) and the mean P3/P0 of 200 poissonised images after the second poissonisation (repoissonisation of mean- $\sigma$ , mean, mean+ $\sigma$ ) using simulation H and F. . . . .	47
5.13	Comparison between the real P3/P0 distribution ( $\sigma$ of P3/P0 after first poissonisation) and the repoissonised distribution ( $\sigma$ of P3/P0 after second poissonisation) using simulation H and F. . . . .	47
5.14	Simulation H. Top panel: Images with 50 000 total counts binned using the <i>contbin</i> technique of Sanders (2006) and the following parameters (smoothsn, sn): left (10,1), middle (15,1), right (25,1). Bottom panel: Residuals of the binned images in % of the ideal image. . . . .	48
5.15	Ratio $[(P3/P0)_{\text{ideal}}]/[(P3/P0)_{\text{mean}}]$ as a function of total counts for five simulations. $(P3/P0)_{\text{ideal}}$ represents the ideal power ratio without any noise, while $(P3/P0)_{\text{mean}}$ is the mean power ratio of 100 simulated, noisy clusters. All power ratios are obtained within $r_{500}$ . Relation for all five simulations (left), excluding simulation A (right). . . . .	49
5.16	Ratio $[(P3/P0)_{\text{ideal}}]/[(P3/P0)_{\text{mean}}]$ as a function of $(P3/P0)_{\text{ideal}}$ for five simulations and two different total counts: $10^3$ (open symbols) and $10^5$ (filled symbols). $(P3/P0)_{\text{ideal}}$ represents the ideal power ratio without any noise, while $(P3/P0)_{\text{mean}}$ is the mean power ratio of 100 simulated, noisy clusters. All power ratios are obtained within the aperture radii 0.8, 0.9 and 1 $r_{500}$ . Relation for all five simulations (left), excluding simulation A (right). . . . .	50
5.17	$(P3/P0)_{\text{ideal}}$ for $10^5$ total counts as a function of aperture radius. The dotted lines indicate where simulation D and E have the same P3/P0. . . . .	51
5.18	Histogram of the distribution of the real bias of 100 poissonised images of simulation D and E. The aperture radii are 0.7 $r_{500}$ for simulation D (filled histogram) and $r_{500}$ for simulation E (line histogram). For those apertures the P3/P0 and the total counts are the same for both simulations. The lines indicate the mean bias of 100 poissonised images for simulation D (dotted line) and E (dashed line) and clearly show that the bias does not only depend on the P3/P0 and total counts but also on the morphology of the cluster. . . . .	51
5.19	Simulation A with Poisson noise (left), A115 (middle), bullet cluster (right). The circles mark 0.3, 0.5, 0.7 and 1 $r_{500}$ . . . . .	52
5.20	P3/P0 for the three chosen clusters for 10 different aperture radii. . . . .	53

5.21	Simulation A. Poissonised images with different total counts and the ideal image. Top panel left to right: $2 \cdot 10^3$ , $10^4$ , $3.16 \cdot 10^4$ . Bottom panel left to right: $10^5$ , ideal image. The circles mark the aperture radius of 100 pixel. . . . .	54
5.22	Simulation A. P3/P0 of 100 poissonised images (black lines) within an aperture radius of 100 pixels as a function of total counts. In addition, the mean P3/P0 of these 100 poissonised images is shown (green line). The ideal P3/P0 is in the range of $10^{-25}$ and not part of this figure (right). P3/P0 residuals (ratio $[(P3/P0)_{\text{mean}} - (P3/P0)_{\text{ideal}}] / [(P3/P0)_{\text{ideal}}]$ ) as a function of total counts, where 0 indicates that the ideal and noisy power ratios are the same (right). . . . .	55
5.23	Simulation F. Poissonised images with different total counts and the ideal image. Top panel left to right: $2 \cdot 10^3$ , $10^4$ , $3.16 \cdot 10^4$ . Bottom panel left to right: $10^5$ , ideal image. The circles mark the aperture radius of 100 pixel. . . . .	56
5.24	Simulation F. P3/P0 of 100 poissonised images (black lines) within an aperture radius of 100 pixels as a function of total counts. In addition, the mean P3/P0 of these 100 poissonised images is shown (green line). The ideal P3/P0 is indicated by the red line (left). P3/P0 residuals (ratio $[(P3/P0)_{\text{mean}} - (P3/P0)_{\text{ideal}}] / [(P3/P0)_{\text{ideal}}]$ ) as a function of total counts, where 0 indicates that the ideal and noisy power ratios are the same (right). . . . .	56
5.25	Simulation E. Poissonised images with different total counts and the ideal image. Top panel left to right: $2 \cdot 10^3$ , $10^4$ , $3.16 \cdot 10^4$ . Bottom panel left to right: $10^5$ , ideal image. The circles mark the aperture radius of 100 pixels. . . . .	58
5.26	Simulation E. P3/P0 of 100 poissonised images (black lines) within an aperture radius of 100 pixels as a function of total counts. In addition, the mean P3/P0 of these 100 poissonised images is shown (green line). The ideal P3/P0 is indicated by the red line (left). P3/P0 residuals (ratio $[(P3/P0)_{\text{mean}} - (P3/P0)_{\text{ideal}}] / [(P3/P0)_{\text{ideal}}]$ ) as a function of total counts, where 0 indicates that the ideal and noisy power ratios are the same (right). . . . .	58
6.1	Relation between P3/P0 obtained within $r_{500}$ and temperature. Red symbols represent the REXCESS clusters, while black symbols show the rest of the sample. The errors are given for P3/P0 and temperature. . . . .	60
6.2	Relation between P3/P0 obtained within $r_{500}$ and luminosity. Red symbols represent the REXCESS clusters, while black symbols show the rest of the sample. The errors are given for P3/P0 and luminosity. . . . .	61
6.3	Relation between P3/P0 obtained within $r_{500}$ and cluster mass. Red symbols represent the REXCESS clusters, while black symbols show the rest of the sample. Cluster mass are only available for the LoCuSS and a few other clusters. The errors are given for P3/P0 and mass. . . . .	62
6.4	Relation between P4/P0 obtained within $r_{500}$ and luminosity. Error bars are given for P4/P0 and luminosities. In addition, linear BCES fits are shown for REXCESS (red) and the whole sample of 80 clusters (black), taking only measurements (thick line) and also errors into account (thin line). The fitting parameters are given in Table 6.1. . . . .	63



6.5	Comparison between the luminosity ratio (luminosity within an aperture of $r_{500}$ and the luminosity within the same aperture, but with the core excluded: $[L(r_{500})] / [L(r_{500} - 0.1r_{500})]$ as a function of luminosity. The errors on the luminosity ratio are propagated from the errors on the individual luminosities. Cool-core (red) and non-cool-core (green) clusters are displayed. For some clusters we do not have cool core information (black). However, they are located in the NCC region and can be assumed to be rather NCC than CC clusters. . . . .	65
6.6	Luminosity-temperature (left) and luminosity-mass relation (right). The fits are obtained using the linear regression method BCES in the log-log plane and the relation: $y=10^{A+\log(x)*B}$ , where A is the intercept and B the slope in the linear fit. The fitting parameters are given in Table 6.3. . . . .	66
6.7	L-T- (left) and L-M- (right) relation for CC (red) and NCC (green) clusters. For some clusters we do not have cool core information (black). However, they are located in the NCC region and can be assumed to be rather NCC than CC clusters. . . . .	67
6.8	L-T- (left) and L-M-relation (right) for undisturbed (red) and disturbed (green) clusters. The clusters are classified by eye. The classification is given in Table 6.10 in the Appendix. . . . .	68
6.9	L-T- (left) and L-M-relation (right) for undisturbed (red) and disturbed (green) clusters. The clusters were classified using power ratios. Undisturbed clusters have power ratios $P3/P0 < 10^{-7}$ , while disturbed clusters have $P3/P0 > 10^{-7}$ . The classification is given in Table 6.10 in the Appendix. . . . .	68
6.10	Relation between the mean (left) and standard deviation $\sigma$ (right) of $P3/P0$ obtained within eight apertures ( $0.3-1 r_{500}$ ) and luminosity. Red symbols represent the REXCESS clusters, while black symbols show the rest of the sample. . . . .	69
6.11	Relation between the mean (left) and standard deviation $\sigma$ (right) of $P4/P0$ obtained within eight apertures ( $0.3-1 r_{500}$ ) and luminosity. Red symbols represent the REXCESS clusters, while black symbols show the rest of the sample. . . . .	70
6.12	Relation between the mean (left) and standard deviation $\sigma$ (right) of $P3/P0$ obtained within eight apertures ( $0.3-1 r_{500}$ ) and temperature. Red symbols represent the REXCESS clusters, while black symbols show the rest of the sample. . . . .	70
6.13	Relation between the mean (left) and standard deviation $\sigma$ (right) of $P3/P0$ obtained within eight apertures ( $0.3-1 r_{500}$ ) and mass. Red symbols represent the REXCESS clusters, while black symbols show the rest of the sample. . . . .	71
6.14	Power ratios of eight "reference clusters" obtained for an aperture of $1h_{80}^{-1}$ Mpc. $P2/P0 - P4/P0$ plane including errors. This relation is seen as <i>evolutionary track</i> (left). $P3/P0 - P4/P0$ plane for the same clusters including errors (right). Source: Buote & Tsai (1996). . . . .	73
6.15	Power ratios for different morphologies (displayed in Figure 6.16) in the $P2/P0 - P3/P0$ plane. The power ratios were computed within an aperture of $1 h_{80}^{-1}$ (left) and $0.5 h_{80}^{-1}$ (right). Source: Buote & Tsai (1996). . . . .	73
6.16	Morphological classification by Buote (2002). Left to right: Single, Primary with small secondary, Double, Complex cluster. Source: Buote (2002). . . . .	74
6.17	Power ratios for different morphologies (displayed in Figure 6.16) in the $P2/P0 - P3/P0$ plane. The power ratios were computed within an aperture of 1 (left) and $0.5 r_{500}$ (right) for the sample of 80 clusters. The morphological classification is shown in Table 6.10 in the Appendix. . . . .	75

6.18	Mean (left) and $\sigma$ (right) of power ratios obtained within eight aperture radii 0.3-1 $r_{500}$ . The different morphologies (displayed in Figure 6.16) are shown in the P2/P0 - P3/P0 plane for the sample of 80 clusters. The morphological classification is shown in Table 6.10 in the Appendix. . . . .	76
6.19	Power ratios for different morphologies (disturbed and undisturbed) in the P2/P0 - P3/P0 plane. Disturbed clusters are shown as red diamonds, while undisturbed ones are displayed as black diamonds. The power ratios are computed within an aperture of 1 $r_{500}$ for the sample of 80 clusters. The morphological classification is shown in Table 6.10 in the Appendix. . . . .	77
6.20	Mean of power ratios obtained within eight aperture radii 0.3-1 $r_{500}$ for different morphologies (disturbed and undisturbed) in the P2/P0 - P3/P0 plane. Disturbed clusters are shown as red diamonds, while undisturbed ones are displayed as black diamonds. The power ratios are computed within an aperture of 1 $r_{500}$ for the sample of 80 clusters. The morphological classification is shown in Table 6.10 in the Appendix. . . . .	77
6.21	Standard deviation $\sigma$ of power ratios obtained within eight aperture radii 0.3-1 $r_{500}$ for different morphologies (disturbed and undisturbed) in the P2/P0 - P3/P0 plane. Disturbed clusters are shown as red diamonds, while undisturbed ones are displayed as black diamonds. The power ratios are computed within an aperture of 1 $r_{500}$ for the sample of 80 clusters. The morphological classification is shown in Table 6.10 in the Appendix. . . . .	78
6.22	Power ratios for different morphologies (disturbed and undisturbed) in the P2/P0 - P4/P0 plane. The power ratios are computed within an aperture of 1 $r_{500}$ (left). Standard deviation $\sigma$ of power ratios obtained within eight aperture radii 0.3-1 $r_{500}$ (right). Disturbed clusters are shown as red diamonds, while undisturbed ones are displayed as black diamonds. The morphological classification is shown in Table 6.10 in the Appendix. . . . .	79
6.23	Power ratios for different morphologies (disturbed and undisturbed) in the P3/P0 - P4/P0 plane. The power ratios are computed within an aperture of 1 $r_{500}$ (left). Standard deviation $\sigma$ of power ratios obtained within eight aperture radii 0.3-1 $r_{500}$ (right). Disturbed clusters are shown as red diamonds, while undisturbed ones are displayed as black diamonds. The morphological classification is shown in Table 6.10 in the Appendix. . . . .	79

Ich habe mich bemüht, sämtliche Inhaber der Bildrechte ausfindig zu machen und ihre Zustimmung zur Verwendung der Bilder in dieser Arbeit eingeholt. Sollte dennoch eine Urheberrechtsverletzung bekannt werden, ersuche ich um Meldung bei mir.

# List of Tables

1.1	Characteristic parameters of a galaxy cluster . . . . .	6
2.1	Characteristics of the EPIC Instruments EPIC MOS (column 1) and EPIC pn (column 2). Source: XMM-Newton Users Handbook V2.7. . . . .	17
3.1	Overview of methods to obtain temperatures. Columns: (1) Cluster name; (2) Extraction area in which temperature is obtained; (3) "used" indicates which of the provided temperatures is used for the analysis. . . . .	24
5.1	Details for simulations and $\beta$ models used. Coordinates of the cluster center (xcent,ycent) and extension of the cluster core (x and y core radius) are given in pixel. The center of the main cluster component (0,0) is chosen to be at the position (324,324) in a 648x648 pixel image. The number of expected total counts is set to $3 \cdot 10^5$ and $\beta$ to 2/3 for all simulations. Norm gives the relative normalisation for each $\beta$ model, where 1.0 equals 100%. Columns (1)-(7): Simulation A-H. . . . .	38
5.2	Ratio $[(B09-bias)_{mean}]/[real\ bias]$ for P2/P0, P3/P0 and P4/P0. $(B09-bias)_{mean}$ is the mean B09-bias of 100 poissonised images. 1 indicates that the values are identical and 2 that the B09-bias is twice as large as the real bias. A negative bias indicates that noise smoothed out structure and that structure needs to be added. . . . .	43
6.1	Fitting parameters for Figure 6.4: Intercept (A) and slope (B) for the relation $y=10^{A+log(x)*B}$ for REXCESS and the whole sample of 80 clusters. NO ERRORS indicates that measurement errors are neglected and only measurement are used for fitting. ERRORS shows the fitting parameters when using measurements and uncertainties. . . . .	62
6.2	Spearman $\rho$ and Kendall $\tau$ rank correlation coefficient and the significance of its deviation from zero ( <i>sig.</i> ). The values are given for an aperture radius of $r_{500}$ . Spearman $\rho$ and Kendall $\tau$ rank correlation coefficients of 1 give a 1-1 correlation and negative values an anti-correlation. Correlation coefficients below 0.5 are considered to indicate no or only very weak correlations. The second value ( <i>sig.</i> ) gives the significance of the deviation from zero, where a high number indicates a small significance in the correlation. . . . .	63
6.2	continued. . . . .	64
6.3	Fitting parameters: Intercept (A) and slope (B) for the relation $y=10^{A+log(x)*B}$ . . . . .	66

6.4	Spearman $\rho$ and Kendall $\tau$ rank correlation coefficient and the significance of its deviation from zero ( <i>sig.</i> ). The values are given for the mean and the standard deviation $\sigma$ of eight aperture radii: 0.3-1 $r_{500}$ . Spearman $\rho$ and Kendall $\tau$ rank correlation coefficients of 1 give a 1-1 correlation and negative values an anti-correlation. Correlation coefficients below 0.5 are considered to indicate no or only very weak correlations. The second value ( <i>sig.</i> ) gives the significance of the deviation from zero, where a high number indicates a small significance in the correlation. . . . .	71
6.4	continued. . . . .	72
6.5	Observational details of cluster sample. . . . .	99
6.5	continued. . . . .	100
6.6	Cluster details: total exposure times and total counts after the final cleaning stage for MOS1, MOS2, pn and all three detectors combined. . . . .	101
6.6	continued. . . . .	102
6.7	Values for $r_{500}$ in Mpc, arcminutes and pixels (1 pixel=4 arcseconds). $r_{500}$ was provided for REXCESS (Pratt et al. 2009) and LoCuSS (Zhang et al. 2008). For all other clusters the relation of Arnaud et al. (2005) was used: $r_{500}[\text{Mpc}] = 1.104 h_{70}^{-1} (kT/5\text{keV})^{0.57} [\Omega_M(1+z)^3 + \Omega_\Lambda]^{-1/2}$ . . . . .	103
6.7	continued. . . . .	104
6.8	Cluster properties in the 0.5-2 keV band. Redshift, $N_H$ , Temperature and $M_{500}$ were taken from the References. $L[0.5-2 \text{ keV}]$ was calculated as described in section 3.2. . . . .	105
6.8	continued. . . . .	106
6.9	Power ratios and measurement errors obtained within $r_{500}$ in the 0.5-2 keV energy range. . . . .	107
6.9	continued. . . . .	108
6.10	Morphological classification for 80 clusters by eye and using the classification scheme of Buote (2002). . . . .	109
6.10	continued. . . . .	110

# List of Abbreviations

B09-method	Method of Böhringer et al. (2010)
CC/NCC	Cool-core/non-cool core cluster
CMB	Cosmic microwave background
FF/EFF	Full frame/Extended full frame
GTI	Good time interval
ICM	Intracluster medium
ISM	Interstellar medium
L-M	Luminosity-mass relation
L-T	Luminosity-temperature relation
MEKAL model	Mewe-Kaastra-Liedahl model
NFW profile	Navarro-Frenk-White profile
$N_{\text{H}}$	Hydrogen column density
ODF	Observation Data File
OoT events	Out-of-time events
PSF	Point-spread-function
SAS	XMM-Newton Science Analysis Software
SZ effect	Sunyaev-Zeldovich effect
$\sigma$	Standard deviation, width of distribution
$z$	Redshift



# Appendix

Table 6.5: Observational details of cluster sample.

Cluster name (1)	Alt. name (2)	OBSID (3)	RA (4)	DEC (5)	Mode (6)	Date (7)
RXCJ0307.0-2840	A3088	042340501	03 07 04.0	-28 40 14.9	FE	16.02.2001
RXCJ0516.7-5430		042340701	05 16 43.8	-54 31 36.7	FE	17.10.2001
RXCJ0528.9-3927		042340801	05 28 56.2	-39 28 49.0	FE	15.09.2001
RXCJ0532.9-3701		042341801	05 32 56.4	-37 02 33.6	FE	07.10.2002
RXCJ0658.5-5556	1E 0657-56	112980201	06 58 16.8	-55 58 36.0	FE	21.10.2000
RXCJ0945.4-0839	A868	017540101	09 45 25.2	-08 39 00.0	FF	02.12.2001
RXCJ2129.6+0005		093030201	21 29 37.9	00 06 38.4	FE	29.10.2002
RXCJ2308.3-0211	A2537	042341201	23 08 23.1	-02 12 31.9	FE	10.06.2001
RXCJ2337.6+0016	A2631	042341301	23 37 40.9	00 17 33.6	FE	06.12.2001
A68		084230201	00 37 06.4	09 09 20.0	FE	14.12.2001
A115		203220101	00 55 50.5	26 25 39.0	FE	16.07.2004
A209		084230301	01 31 53.7	-13 37 47.0	FE	15.01.2001
A267		084230401	01 52 41.8	01 01 43.0	FE	02.01.2002
A383		084230501	02 48 03.2	-03 32 42.0	FE	16.08.2002
A773		084230601	09 17 52.8	51 44 38.0	FE	26.04.2001
A963		084230701	10 17 03.6	39 03 56.0	FE	02.11.2001
A1413		112230501	11 55 19.0	23 25 36.0	FF	06.12.2000
A1763		084230901	13 35 19.0	40 60 56.0	FE	13.12.2002
A1914		112230201	14 26 02.0	37 50 48.0	FE	18.12.2002
A2390		111270101	21 53 37.0	17 42 45.0	FF	19.06.2001
A2667		148990101	23 51 39.1	-26 05 04.0	FF	21.06.2003
A2204		306490401	16 32 47.0	05 35 30.1	FF	14.02.2006
A2218		112980101	16 35 48.0	66 13 36.0	FE	28.09.2002
RXCJ0232.2-4420		042340301	02 32 17.2	-44 21 43.1	FE	11.07.2002
A13		200270101	00 13 28.5	-19 30 02.6	FF	25.06.2004
A520		201510101	04 54 09.3	02 55 21.0	FE	16.09.2004
A665		109890401	08 31 58.0	65 50 20.0	FE	04.04.2001
A1068		147630101	10 40 44.6	39 57 12.0	FF	24.05.2003
A1589		149900301	12 41 18.3	18 35 33.2	FF	18.06.2003
A2163		112230601	16 15 46.0	-06 09 00.0	FF	28.08.2000
A2717		145020201	00 03 12.9	-35 56 12.3	FF	26.12.2002
A3112		105660101	03 17 56.0	-44 14 06.0	FE	24.12.2000
A3827		149670101	22 01 56.0	-59 57 57.0	FF	16.11.2002

Columns: (1) Cluster name; (2) Alternative cluster name; (3) Observation ID; (4) Right ascension (RA 2000); (5) Declination (DA 2000); (6) Observation Mode: FF-Full Frame, EF-Extended Full Frame; (7) Observation Date.

Table 6.5: continued.

Cluster name (1)	Alt. name (2)	OBSID (3)	RA (4)	DEC (5)	Mode (6)	Date (7)
A3911		149670301	22 46 17.0	-52 44 35.0	FF	23.10.2003
A3921		112240101	22 49 48.0	-64 23 60.0	FF	25.10.2000
E1455+2232		108670201	14 57 15.0	22 21 36.0	FF	03.08.2002
PKS0745-19		105870101	07 47 31.5	-19 18 40.0	FE	31.10.2000
RXJ1347-1145		112960101	13 47 31.0	-11 45 09.0	FF	31.07.2002
Sersic159-3		147800101	23 14 59.0	-42 44 36.0	FF	20.11.2002
ZW3146		108670101	10 23 39.8	04 11 11.0	FF	05.12.2000
A2597		108460201	23 25 21.0	-12 07 12.0	FF	30.11.2000
A1775		108460101	13 41 50.0	26 21 00.0	FF	10.01.2003
A1837		109910101	14 01 36.0	-11 08 44.0	FE	11.01.2001
RXCJ0014.3-3022	A2744	042340101	00 14 20.1	-30 23 32.5	FE	30.05.2001
RXCJ1131.9-1955	A1300	042341001	11 31 56.6	-19 56 32.9	FE	01.07.2001
A1651		203020101	12 59 22.9	-04 12 46.0	FF	01.07.2004
A133		144310101	01 02 41.1	-21 53 47.0	FE	22.12.2002
A2626		148310101	23 36 30.5	21 09 45.5	FE	28.12.2002
A2065		202080201	15 22 29.3	27 43 35.0	FE	08.01.2005
A1689	RXCJ1311.4-0120	093030101	13 11 29.4	-01 20 29.0	FE	24.12.2001
RXCJ0547.6-3152	A3364	201900901	05 47 38.2	-31 53 31.4	FE	07.03.2004
RXCJ0645.4-5413	A3404	201903401	06 45 29.3	-54 13 08.4	FE	12.06.2004
RXCJ0958.3-1103	A907	201903501	09 58 22.2	-11 04 34.9	FE	17.06.2004
RXCJ2218.6-3853		201903001	22 18 40.2	-38 54 50.6	FE	24.10.2004
RXCJ0003.8+0203	A2700	201900101	00 03 50.6	02 04 48.2	FE	24.06.2004
RXCJ0006.0-3443	A2721	201900201	00 06 03.0	-34 43 26.8	FE	08.12.2004
RXCJ0020.7-2542	A22	201900301	00 20 42.8	-25 43 37.1	FE	26.05.2004
RXCJ0049.4-2931	AS84	201900401	00 49 24.1	-29 31 27.8	FE	04.12.2004
RXCJ0145.0-5300	A2941	201900501	01 45 02.3	-53 01 50.0	FE	12.11.2004
RXCJ0345.7-4112	AS384	201900801	03 45 45.7	-41 12 27.4	FE	05.03.2004
RXCJ0605.8-3518	A3378	201901001	06 05 52.7	-35 18 01.8	FE	29.10.2004
RXCJ0616.8-4748		201901101	06 16 53.6	-47 48 17.6	FE	26.04.2004
RXCJ0821.8+0112	A653	201901301	08 21 51.7	01 13 41.8	FE	13.10.2004
RXCJ1044.5-0704	A1084	201901501	10 44 33.1	-07 04 22.4	FE	23.12.2004
RXCJ1141.4-1216		201901601	11 41 24.3	-12 16 19.9	FE	09.07.2004
RXCJ1236.7-3354	AS700	201901701	12 36 44.7	-33 54 10.4	FE	28.07.2004
RXCJ1302.8-0230	A1663	201901801	13 02 50.7	-02 30 22.3	FE	22.06.2004
RXCJ1516.3+0005	A2050	201902001	15 16 19.2	00 06 52.0	FE	22.07.2004
RXCJ2014.8-2430		201902201	20 14 49.7	-24 31 30.2	FE	08.01.2004
RXCJ2023.0-2056	AS868	201902301	20 23 01.6	-20 57 55.3	FE	06.04.2005
RXCJ2048.1-1750	A2328	201902401	20 48 10.6	-17 51 37.6	FE	13.05.2004
RXCJ2129.8-5048	A3771	201902501	21 29 51.0	-50 48 03.9	FE	16.10.2004
RXCJ2149.1-3041	A3841	201902601	21 49 07.4	-30 42 55.3	FE	29.11.2004
RXCJ2157.4-0747	A2399	404910701	21 57 25.8	-07 48 40.5	FE	19.11.2006
RXCJ2217.7-3543	A3854	201902901	22 17 43.3	-35 44 34.3	FE	12.05.2005
RXCJ0211.4-4017	A2984	201900601	02 11 25.5	-40 17 11.8	FE	27.12.2004
RXCJ2319.6-7313		201903301	23 19 41.8	-73 14 51.2	FE	15.05.2004
RXCJ0225.1-2928		302610601	02 25 10.5	-29 28 26.0	FE	27.01.2006
RXCJ1516.5-0056	A2051	201902101	15 16 34.0	00 57 55.6	FE	03.08.2004
RXCJ2234.5-3744	A3888	404910801	22 34 31.0	-37 44 06.0	FE	02.05.2006

Columns: (1) Cluster name; (2) Alternative cluster name; (3) Observation ID; (4) Right ascension (RA 2000); (5) Declination (DA 2000); (6) Observation Mode: FF-Full Frame, EF-Extended Full Frame; (7) Observation Date.



Table 6.6: Cluster details: total exposure times and total counts after the final cleaning stage for MOS1, MOS2, pn and all three detectors combined.

Cluster name (1)	Total exposure time [s]				Total counts [ $r_{500}$ ]			
	pn (2)	MOS1 (3)	MOS2 (4)	all (5)	pn (6)	MOS1 (7)	MOS2 (8)	all (9)
RXCJ0307.0-2840	6530	10800	10500	27830	11231.6	5572.8	5575.5	22379.9 $\pm$ 0.03
RXCJ0516.7-5430	3630	7340	7060	18030	4283.4	2510.3	2633.4	9427.1 $\pm$ 0.04
RXCJ0528.9-3927	3320	6090	5990	15400	5644.0	3337.3	3504.2	12485.5 $\pm$ 0.04
RXCJ0532.9-3701	5000	9150	8960	23110	7650.0	4218.2	4327.7	16195.8 $\pm$ 0.03
RXCJ0658.5-5556	13700	20800	18700	53200	46306.0	21632.0	19822.0	87760.0 $\pm$ 0.03
RXCJ0945.4-0839	2780	4660	4390	11830	5615.6	2889.2	2875.5	11380.3 $\pm$ 0.05
RXCJ2129.6+0005	21600	33900	32400	87900	48168.0	23085.9	22712.4	93966.3 $\pm$ 0.02
RXCJ2308.3-0211	750	2230	2190	5170	652.5	590.9	578.2	1821.6 $\pm$ 0.06
RXCJ2337.6+0016	5850	10200	9610	25660	8014.5	4212.6	4074.6	16301.7 $\pm$ 0.03
A68	15000	22100	20800	57900	19050.0	8663.2	8320.0	36033.2 $\pm$ 0.02
A115	22100	29600	28800	80500	69836.0	26462.4	25056.0	121354.4 $\pm$ 0.02
A209	9100	14200	13300	36600	22659.0	10266.6	10081.4	43007.0 $\pm$ 0.03
A267	9010	14000	13400	36410	12614.0	5922.0	6083.6	24619.6 $\pm$ 0.02
A383	16300	23900	22300	62500	32926.0	14794.1	14272.0	61992.1 $\pm$ 0.02
A773	10900	10100	9530	30530	22781.0	6433.7	6213.6	35428.3 $\pm$ 0.03
A963	12900	20100	17800	50800	29025.0	13567.5	12744.8	55337.3 $\pm$ 0.03
A1413	560	16000	15300	31860	1551.2	25600.0	24633.0	51784.2 $\pm$ 0.18
A1763	7390	11100	10900	29390	15962.4	6970.8	7292.1	30225.3 $\pm$ 0.03
A1914	8670	12100	11600	32370	51933.3	21538.0	21692.0	95163.3 $\pm$ 0.05
A2390	6610	8340	7470	22420	26770.5	10425.0	9785.0	46981.2 $\pm$ 0.05
A2667	11300	19000	17100	47400	39437.0	19760.0	19152.0	78349.0 $\pm$ 0.03
A2204	6550	14500	10400	31450	60980.5	40745.0	30056.0	131781.5 $\pm$ 0.06
A2218	9670	13500	12700	35870	25238.7	10543.5	10490.2	46272.4 $\pm$ 0.03
RXCJ0232.2-4420	5860	10100	9580	25540	13243.6	6524.6	6504.8	26273.0 $\pm$ 0.04
A13	17500	20900	19400	57800	37450.0	13229.7	12668.2	63347.9 $\pm$ 0.02
A520	19800	30500	27200	77500	45936.0	21624.5	19856.0	87416.5 $\pm$ 0.02
A665	6020	9430	8520	23970	21310.8	10467.3	9798.0	41576.1 $\pm$ 0.05
A1068	11000	15400	14400	40800	41360.0	16786.0	16992.0	75138.0 $\pm$ 0.03
A1589	5580	7070	6840	19490	16293.6	5952.9	6101.3	28347.8 $\pm$ 0.05
A2163	4280	6750	6300	17330	27477.6	13905.0	12978.0	54360.6 $\pm$ 0.07
A2717	20000	23800	23300	67100	62400.0	21681.8	22601.0	106682.8 $\pm$ 0.03
A3112	7610	10400	10200	28210	82949.0	35256.0	35700.0	153905.0 $\pm$ 0.06
A3827	9110	11000	10500	30610	66594.1	24970.0	24045.0	115609.1 $\pm$ 0.05
A3911	11700	14000	13500	39200	50895.0	18340.0	17955.0	87190.0 $\pm$ 0.04
A3921	193	16200	15400	31793	1003.6	26082.0	25718.0	52803.6 $\pm$ 0.18
E1455+2232	22900	30400	29600	82900	46487.0	18088.0	18233.6	82808.6 $\pm$ 0.02
PKS0745-19	5910	9050	8720	23680	58686.3	30227.0	30345.6	119258.9 $\pm$ 0.07
RXJ1347-1145	25000	30100	29800	84900	64500.0	23327.5	23959.2	111786.7 $\pm$ 0.02
Sersic159-3	35600	44000	42200	121800	342828.0	127160.0	127022.0	597010.0 $\pm$ 0.03
ZW3146	38300	45100	44000	127400	121411.0	43115.6	43120.0	207646.6 $\pm$ 0.02
A2597	300	8800	8320	17420	2418.0	21736.0	21299.2	45453.2 $\pm$ 0.17
A1775	10500	12900	12500	35900	47670.0	17544.0	17500.0	82714.0 $\pm$ 0.04
A1837	19100	23600	22800	65500	50615.0	19234.0	18582.0	88431.0 $\pm$ 0.03
RXCJ0014.3-3022	9150	13500	13400	36050	14823.0	6966.0	7035.0	28824.0 $\pm$ 0.03
RXCJ1131.9-1955	7970	11300	11200	30470	9962.5	4034.1	4155.2	18151.8 $\pm$ 0.03

Columns: (1) Cluster name; (2)-(5) Total exposure times in seconds after cleaning for each detector (columns 2-4)) and after combining them (5); (6)-(9) Total counts obtained within  $r_{500}$  for each detector (columns 6-8) and after combining them (9).

Table 6.6: continued.

Cluster name (1)	Total exposure time [s]				Total counts [ $r_{500}$ ]			
	pn (2)	MOS1 (3)	MOS2 (4)	all (5)	pn (6)	MOS1 (7)	MOS2 (8)	all (9)
A1651	2780	4520	4380	11680	26910.4	13379.2	13271.4	53561.0 $\pm$ 0.10
A133	5580	7810	6250	19640	44249.4	18587.8	15500.0	78337.2 $\pm$ 0.06
A2626	13300	16700	15900	45900	65569.0	25050.0	25122.0	115741.0 $\pm$ 0.03
A2065	5680	8180	7650	21510	50495.2	21513.4	20808.0	92816.6 $\pm$ 0.07
A1689	18600	23300	22300	64200	109368.0	42406.0	41924.0	193698.0 $\pm$ 0.03
RXCJ0547.6-3152	11300	15100	14400	40800	31979.0	12819.9	12585.6	57384.5 $\pm$ 0.03
RXCJ0645.4-5413	6470	8730	8290	23490	25880.0	10737.9	10362.5	46980.4 $\pm$ 0.05
RXCJ0958.3-1103	3650	6560	5960	16170	10877.0	5897.4	5584.5	22358.9 $\pm$ 0.05
RXCJ2218.6-3853	7970	14900	14200	37070	29249.9	15943.0	14910.0	60102.9 $\pm$ 0.04
RXCJ0003.8+0203	11500	15500	14400	41400	23345.0	9377.5	8928.0	41650.5 $\pm$ 0.03
RXCJ0006.0-3443	875	3130	2970	6975	2511.3	2641.7	2417.6	7570.6 $\pm$ 0.09
RXCJ0020.7-2542	7320	10500	9960	27780	17860.8	7402.5	7380.4	32643.7 $\pm$ 0.04
RXCJ0049.4-2931	9290	13700	12700	35690	14678.2	6425.3	6235.7	27339.2 $\pm$ 0.03
RXCJ0145.0-5300	4900	7990	7700	20590	13916.0	6647.7	6606.6	27170.3 $\pm$ 0.05
RXCJ0345.7-4112	4320	9860	9520	23700	11102.4	7444.3	7654.1	26200.8 $\pm$ 0.04
RXCJ0605.8-3518	9340	15800	14500	39640	34558.0	18170.0	16965.0	69693.0 $\pm$ 0.04
RXCJ0616.8-4748	2400	8030	7670	18100	3360.0	3541.2	3505.2	10406.4 $\pm$ 0.05
RXCJ0821.8+0112	2220	3740	3450	9410	2686.2	1256.6	1273.0	5215.9 $\pm$ 0.07
RXCJ1044.5-0704	12800	18700	17700	49200	46080.0	20196.0	20001.0	86277.0 $\pm$ 0.03
RXCJ1141.4-1216	15100	19700	18500	53300	36844.0	14262.8	13653.0	64759.8 $\pm$ 0.02
RXCJ1236.7-3354	1960	5370	4980	12310	3606.4	2878.3	2778.8	9263.6 $\pm$ 0.06
RXCJ1302.8-0230	9510	14300	13600	37410	18924.9	8351.2	8282.4	35558.5 $\pm$ 0.03
RXCJ1516.3+0005	13500	16900	16100	46500	32400.0	12151.1	11640.3	56191.4 $\pm$ 0.03
RXCJ2014.8-2430	10900	16400	15300	42600	56571.0	26896.0	25398.0	108865.0 $\pm$ 0.04
RXCJ2023.0-2056	4290	8090	6420	18800	8794.5	4829.7	4179.4	17803.7 $\pm$ 0.05
RXCJ2048.1-1750	12800	17300	15800	45900	24704.0	9826.4	9385.2	43915.6 $\pm$ 0.03
RXCJ2129.8-5048	6510	11600	11100	29210	15428.7	8178.0	7881.0	31487.7 $\pm$ 0.04
RXCJ2149.1-3041	12400	17500	16300	46200	29884.0	12582.5	12045.7	54512.2 $\pm$ 0.03
RXCJ2157.4-0747	8070	11300	8940	28310	14929.5	6361.9	5077.9	26369.3 $\pm$ 0.04
RXCJ2217.7-3543	12000	17000	13000	42000	26760.8	11543.0	8814.0	47117.0 $\pm$ 0.03
RXCJ0211.4-4017	16100	21700	19900	57700	15166.2	6119.4	5691.4	26977.0 $\pm$ 0.02
RXCJ2319.6-7313	4220	6840	6320	17380	9874.8	4336.6	4316.6	18527.9 $\pm$ 0.04
RXCJ0225.1-2928	8620	10500	8140	27260	14395.4	5250.0	4078.1	23723.5 $\pm$ 0.04
RXCJ1516.5-0056	14400	19300	18600	52300	21888.0	8685.0	8072.4	38645.4 $\pm$ 0.02
RXCJ2234.5-3744	8580	12600	9200	30380	40583.4	18144.0	13064.0	71791.4 $\pm$ 0.04

Columns: (1) Cluster name; (2)-(5) Total exposure times in seconds after cleaning for each detector (columns 2-4)) and after combining them (5); (6)-(9) Total counts obtained within  $r_{500}$  for each detector (columns 6-8) and after combining them (9).

Table 6.7: Values for  $r_{500}$  in Mpc, arcminutes and pixels (1 pixel=4 arcseconds).  $r_{500}$  was provided for REXCESS (Pratt et al. 2009) and LoCuSS (Zhang et al. 2008). For all other clusters the relation of Arnaud et al. (2005) was used:  $r_{500}[\text{Mpc}] = 1.104 h_{70}^{-1} (kT/5\text{keV})^{0.57} [\Omega_M(1+z)^3 + \Omega_\Lambda]^{-1/2}$ .

Cluster name (1)	$r_{500}$ [Mpc] (2)	$r_{500}$ ['] (3)	$r_{500}$ [pixel] (4)
RXCJ0307.0-2840	1.14	4.72	70.8
RXCJ0516.7-5430	1.19	4.49	67.4
RXCJ0528.9-3927	1.19	4.60	69.0
RXCJ0532.9-3701	1.13	4.47	67.1
RXCJ0658.5-5556	1.42	5.33	78.0
RXCJ0945.4-0839	1.27	7.94	119.1
RXCJ2129.6+0005	1.06	4.71	70.7
RXCJ2308.3-0211	1.24	4.64	69.6
RXCJ2337.6+0016	1.43	5.65	84.8
A68	1.21	5.05	75.8
A115	1.07	5.45	81.8
A209	1.15	5.59	83.9
A267	1.06	4.78	71.7
A383	0.98	5.20	78.0
A773	1.33	6.28	94.2
A963	1.14	5.60	84.0
A1413	1.18	7.80	117.0
A1763	1.12	5.09	76.3
A1914	1.71	9.75	146.3
A2390	1.29	5.76	86.4
A2667	1.19	5.37	80.6
A2204	1.17	7.35	110.3
A2218	1.07	5.96	89.4
RXCJ0232.2-4420	1.30	5.02	75.3
A13	0.95	8.32	124.7
A520	1.32	6.80	102.0
A665	1.33	7.30	109.5
A1068	1.00	6.43	96.4
A1589	0.88	10.68	160.2
A2163	1.87	9.32	139.8
A2717	0.74	12.34	185.0
A3112	0.98	11.83	177.4
A3827	1.21	11.35	170.3
A3911	1.16	10.85	162.7
A3921	1.08	10.51	157.6
E1455+2232	0.98	4.07	61.1
PKS0745-19	1.38	12.61	189.1
RXJ1347-1145	1.23	3.71	55.7
Sersic159-3	0.69	10.44	156.6
ZW3146	1.23	4.78	71.6
A2597	0.89	9.82	147.2
A1775	0.91	10.60	159.1
A1837	0.79	10.37	155.5
RXCJ0014.3-3022	1.43	5.23	78.4

Columns: (1) Cluster name; (2)  $r_{500}$  in Mpc.  $r_{500}$  in Mpc was provided for REXCESS (Pratt et al. 2009) and LoCuSS (Zhang et al. 2008). For all other clusters the relation of Arnaud et al. (2005) was used:  $r_{500}[\text{Mpc}] = 1.104 \cdot h_{70}^{-1} (kT/5\text{keV})^{0.57} [\Omega_M(1+z)^3 + \Omega_\Lambda]^{-1/2}$ . The standard  $\Lambda$ CDM cosmology was used:  $H_0=70$ ,  $\Omega_\Lambda=0.73$ ,  $\Omega_M=0.27$ ; (3)  $r_{500}$  in arcminutes; (4)  $r_{500}$  in pixel, where 1 pixel=4 arcseconds.

Table 6.7: continued.

Cluster name (1)	$r_{500}$ [Mpc] (2)	$r_{500}$ ['] (3)	$r_{500}$ [pixel] (4)
RXCJ1131.9-1955	1.35	4.95	74.2
A1651	1.22	12.74	192.0
A133	0.92	13.80	207.0
A2626	0.75	11.78	176.6
A2065	1.05	12.63	189.5
A1689	1.44	7.11	106.7
RXCJ0547.6-3152	1.32	7.27	109.1
RXCJ0645.4-5413	1.28	7.54	113.1
RXCJ0958.3-1103	0.76	4.40	65.9
RXCJ2218.6-3853	1.13	7.56	113.4
RXCJ0003.8+0203	0.88	8.48	127.2
RXCJ0006.0-3443	1.06	8.46	126.9
RXCJ0020.7-2542	1.05	6.99	104.9
RXCJ0049.4-2931	0.81	6.78	101.6
RXCJ0145.0-5300	1.09	8.57	128.5
RXCJ0345.7-4112	0.69	9.83	147.5
RXCJ0605.8-3518	1.05	7.08	106.2
RXCJ0616.8-4748	0.94	7.41	111.2
RXCJ0821.8+0112	0.76	8.13	121.9
RXCJ1044.5-0704	0.93	6.50	97.6
RXCJ1141.4-1216	0.89	6.83	102.4
RXCJ1236.7-3354	0.75	8.34	125.2
RXCJ1302.8-0230	0.84	8.81	132.2
RXCJ1516.3+0005	0.99	7.71	115.7
RXCJ2014.8-2430	1.16	7.19	107.8
RXCJ2023.0-2056	0.74	11.25	168.7
RXCJ2048.1-1750	1.08	6.94	104.2
RXCJ2129.8-5048	0.90	9.96	149.4
RXCJ2149.1-3041	0.89	6.89	103.4
RXCJ2157.4-0747	0.75	11.15	167.3
RXCJ2217.7-3543	1.02	6.55	98.3
RXCJ0211.4-4017	0.69	6.13	92.0
RXCJ2319.6-7313	0.78	7.12	106.9
RXCJ0225.1-2928	0.69	9.90	148.5
RXCJ1516.5-0056	0.93	7.13	107.0
RXCJ2234.5-3744	1.28	8.11	121.7

Columns: (1) Cluster name; (2)  $r_{500}$  in Mpc.  $r_{500}$  in Mpc was provided for REXCESS (Pratt et al. 2009) and LoCuSS (Zhang et al. 2008). For all other clusters the relation of Arnaud et al. (2005) was used:  $r_{500}[\text{Mpc}] = 1.104 \cdot h_{70}^{-1} (\text{kT}/5\text{keV})^{0.57} [\Omega_M(1+z)^3 + \Omega_\Lambda]^{-1/2}$ . The standard  $\Lambda$ CDM cosmology was used:  $H_0=70$ ,  $\Omega_\Lambda=0.73$ ,  $\Omega_M=0.27$ ; (3)  $r_{500}$  in arcminutes; (4)  $r_{500}$  in pixel, where 1 pixel=4 arcseconds.

Table 6.8: Cluster properties in the 0.5-2 keV band. Redshift,  $N_{\text{H}}$ , Temperature and  $M_{500}$  were taken from the References.  $L[0.5\text{-}2\text{ keV}]$  was calculated as described in section 3.2.

Cluster name (1)	$z$ (2)	$N_{\text{H}}$ (3)	T (4)	M (5)	$L[0.5\text{-}2\text{ keV}]$ (6)	References (7)
RXCJ0307.0-2840	0.26	0.0136	$7.10 \pm 0.40$	$5.47 \pm 2.01$	$4.76 \pm 0.05$	1,3
RXCJ0516.7-5430	0.29	0.0686	$6.70 \pm 0.50$	$6.40 \pm 1.83$	$5.07 \pm 0.10$	1,3
RXCJ0528.9-3927	0.28	0.0212	$6.60 \pm 0.50$	$6.40 \pm 1.87$	$5.92 \pm 0.08$	1,3
RXCJ0532.9-3701	0.27	0.0290	$7.70 \pm 0.60$	$5.40 \pm 1.59$	$5.04 \pm 0.06$	1,3
RXCJ0658.5-5556	0.30	0.0653	$10.70 \pm 0.20$	$10.99 \pm 5.31$	$14.35 \pm 0.07$	1,3
RXCJ0945.4-0839	0.15	0.0359	$5.30 \pm 0.50$	$6.73 \pm 1.95$	$1.95 \pm 0.03$	1
RXCJ2129.6+0005	0.24	0.0428	$6.30 \pm 0.20$	$4.33 \pm 1.27$	$5.48 \pm 0.03$	1
RXCJ2308.3-0211	0.30	0.0122	$7.60 \pm 0.70$	$7.42 \pm 2.28$	$3.23 \pm 0.14$	1,3
RXCJ2337.6+0016	0.28	0.0382	$7.50 \pm 0.50$	$10.95 \pm 3.22$	$4.65 \pm 0.06$	1,3
A68	0.25	0.0493	$7.30 \pm 0.30$	$6.51 \pm 1.93$	$3.55 \pm 0.03$	1,3
A115	0.20	0.0543	$6.20 \pm 0.10$	$4.23 \pm 1.14$	$5.50 \pm 0.02$	1
A209	0.21	0.0164	$7.10 \pm 0.30$	$5.33 \pm 1.71$	$4.53 \pm 0.03$	1,3
A267	0.23	0.0280	$6.20 \pm 0.10$	$4.29 \pm 1.30$	$3.15 \pm 0.03$	1
A383	0.19	0.0392	$4.70 \pm 0.20$	$3.17 \pm 0.94$	$3.05 \pm 0.02$	1,3
A773	0.22	0.0144	$8.30 \pm 0.40$	$8.30 \pm 2.45$	$3.92 \pm 0.03$	1,3
A963	0.21	0.0140	$6.50 \pm 0.20$	$5.19 \pm 1.52$	$3.83 \pm 0.02$	1
A1413	0.14	0.0219	$6.60 \pm 0.10$	$5.38 \pm 1.57$	$2.21 \pm 0.13$	1,3,4
A1763	0.23	0.0936	$5.80 \pm 0.30$	$4.96 \pm 1.46$	$5.72 \pm 0.05$	1
A1914	0.17	0.0095	$8.80 \pm 0.30$	$16.76 \pm 4.87$	$6.92 \pm 0.03$	1,3
A2390	0.23	0.0680	$11.60 \pm 0.60$	$7.67 \pm 2.28$	$10.24 \pm 0.06$	1
A2667	0.22	0.0165	$7.00 \pm 0.30$	$6.02 \pm 1.74$	$6.92 \pm 0.03$	1,3
A2204	0.15	0.0567	$8.30 \pm 0.20$	$5.31 \pm 1.52$	$9.31 \pm 0.04$	1,3,4
A2218	0.17	0.0324	$6.60 \pm 0.30$	$4.18 \pm 1.27$	$3.19 \pm 0.02$	1,3
RXCJ0232.2-4420	0.28	0.0250	$6.60 \pm 0.30$	$8.43 \pm 2.48$	$7.94 \pm 0.07$	1,3
A13	0.10	0.0240	$4.16 \pm 0.18$	$0.00 \pm 0.00$	$0.88 \pm 0.00$	3
A520	0.19	0.0680	$8.00 \pm 0.55$	$0.00 \pm 0.00$	$4.05 \pm 0.02$	3
A665	0.18	0.0427	$7.94 \pm 0.28$	$0.00 \pm 0.00$	$4.81 \pm 0.04$	3
A1068	0.14	0.0170	$4.67 \pm 0.11$	$3.87 \pm 0.28$	$2.74 \pm 0.01$	3,4
A1589	0.07	0.0170	$3.56 \pm 0.26$	$0.00 \pm 0.00$	$0.55 \pm 0.00$	3
A2163	0.20	0.1100	$14.77 \pm 1.31$	$0.00 \pm 0.00$	$13.23 \pm 0.08$	3
A2717	0.05	0.0120	$2.56 \pm 0.06$	$1.10 \pm 0.12$	$0.27 \pm 0.00$	3,4
A3112	0.07	0.0200	$4.27 \pm 0.15$	$0.00 \pm 0.00$	$2.08 \pm 0.01$	3
A3827	0.10	0.0230	$6.34 \pm 0.31$	$0.00 \pm 0.00$	$2.53 \pm 0.01$	3
A3911	0.10	0.0130	$5.84 \pm 0.36$	$0.00 \pm 0.00$	$1.46 \pm 0.01$	3
A3921	0.09	0.0250	$5.16 \pm 0.19$	$0.00 \pm 0.00$	$1.66 \pm 0.05$	3
E1455+2232	0.26	0.0880	$5.04 \pm 0.36$	$0.00 \pm 0.00$	$7.00 \pm 0.03$	3
PKS0745-19	0.10	0.0415	$7.97 \pm 0.28$	$7.27 \pm 0.75$	$4.18 \pm 0.02$	3,4
RXJ1347-1145	0.45	0.0260	$9.67 \pm 0.92$	$0.00 \pm 0.00$	$24.30 \pm 0.10$	3
Sersic159-3	0.06	0.0148	$2.26 \pm 0.04$	$0.00 \pm 0.00$	$1.08 \pm 0.00$	3
ZW3146	0.28	0.0265	$7.59 \pm 0.46$	$0.00 \pm 0.00$	$10.96 \pm 0.03$	3
A2597	0.09	0.0248	$3.67 \pm 0.09$	$2.22 \pm 0.22$	$2.20 \pm 0.04$	3,4
A1775	0.08	0.0105	$3.78 \pm 0.18$	$0.00 \pm 0.00$	$0.92 \pm 0.00$	3
A1837	0.07	0.0440	$2.93 \pm 0.10$	$0.00 \pm 0.00$	$0.45 \pm 0.00$	3
RXCJ0014.3-3022	0.31	0.0160	$10.10 \pm 0.30$	$7.40 \pm 2.90$	$6.46 \pm 0.06$	2
RXCJ1131.9-1955	0.31	0.0450	$9.20 \pm 0.40$	$5.20 \pm 3.00$	$5.46 \pm 0.06$	2
A1651	0.08	0.1600	$6.30 \pm 0.00$	$0.00 \pm 0.00$	$3.65 \pm 0.02$	5

Columns: (1) Cluster name; (2)  $z$ : Redshift; (3)  $N_{\text{H}}$ : hydrogen column density; (4) T: Temperatures obtain in different apertures in keV. Details given in Table 3.1; (5) M: Mass within  $r_{500}$  in  $10^{14} M_{\odot}$ ; (6)  $L[0.5\text{-}2\text{ keV}]$ : 0.5-2 keV band luminosity in the  $r < r_{500}$  region in  $10^{44}$  erg/s; (7) References: 1-Zhang et al. (2008), 2-Zhang et al. (2006), 3-Snowden et al. (2008), 4-Arnaud et al. (2005), 5-Buote & Tsai (1996), 6-REXCESS: Pratt et al. (2009),  $M_{500}$ : Pratt et al. (2010).

Table 6.8: continued.

Cluster name (1)	z (2)	$N_{\text{H}}$ (3)	T (4)	M (5)	L[0.5-2 keV] (6)	References (7)
A133	0.06	0.0160	$3.82 \pm 0.17$	$0.00 \pm 0.00$	$0.93 \pm 0.00$	3
A2626	0.05	0.0410	$2.67 \pm 0.13$	$0.00 \pm 0.00$	$0.57 \pm 0.00$	3
A2065	0.07	0.0205	$4.85 \pm 0.17$	$0.00 \pm 0.00$	$1.73 \pm 0.01$	3
A1689	0.18	0.0182	$8.91 \pm 0.08$	$8.41 \pm 0.08$	$7.62 \pm 0.02$	1,3,6
RXCJ0547.6-3152	0.15	0.0285	$6.02 \pm 0.07$	$4.98 \pm 0.09$	$2.48 \pm 0.01$	1,6
RXCJ0645.4-5413	0.16	0.0651	$6.95 \pm 0.13$	$7.38 \pm 0.14$	$4.81 \pm 0.03$	1,6
RXCJ0958.3-1103	0.17	0.0540	$5.34 \pm 0.21$	$4.17 \pm 0.19$	$3.64 \pm 0.03$	1,6
RXCJ2218.6-3853	0.14	0.0138	$5.84 \pm 0.11$	$4.92 \pm 0.11$	$2.78 \pm 0.02$	1,6
RXCJ0003.8+0203	0.09	0.0265	$3.85 \pm 0.09$	$2.11 \pm 0.04$	$0.66 \pm 0.00$	6
RXCJ0006.0-3443	0.11	0.1760	$5.03 \pm 0.15$	$3.95 \pm 0.12$	$2.14 \pm 0.04$	6
RXCJ0020.7-2542	0.14	0.0294	$5.69 \pm 0.15$	$3.84 \pm 0.06$	$1.94 \pm 0.02$	6
RXCJ0049.4-2931	0.11	0.0248	$3.09 \pm 0.10$	$1.62 \pm 0.04$	$0.72 \pm 0.01$	6
RXCJ0145.0-5300	0.12	0.1100	$5.53 \pm 0.12$	$4.37 \pm 0.08$	$1.88 \pm 0.02$	6
RXCJ0345.7-4112	0.06	0.0115	$2.19 \pm 0.05$	$0.97 \pm 0.02$	$0.33 \pm 0.00$	6
RXCJ0605.8-3518	0.14	0.0550	$4.56 \pm 0.05$	$3.87 \pm 0.06$	$3.09 \pm 0.02$	6
RXCJ0616.8-4748	0.12	0.0105	$4.22 \pm 0.10$	$2.70 \pm 0.06$	$0.70 \pm 0.01$	6
RXCJ0821.8+0112	0.08	0.0440	$2.68 \pm 0.09$	$1.31 \pm 0.11$	$0.33 \pm 0.01$	6
RXCJ1044.5-0704	0.13	0.0340	$3.41 \pm 0.03$	$2.27 \pm 0.02$	$2.63 \pm 0.01$	6
RXCJ1141.4-1216	0.12	0.0330	$3.31 \pm 0.03$	$2.27 \pm 0.02$	$1.39 \pm 0.01$	6
RXCJ1236.7-3354	0.08	0.0560	$2.70 \pm 0.05$	$1.33 \pm 0.02$	$0.48 \pm 0.01$	6
RXCJ1302.8-0230	0.08	0.0170	$2.97 \pm 0.06$	$1.89 \pm 0.03$	$0.52 \pm 0.00$	6
RXCJ1516.3+0005	0.12	0.0460	$4.51 \pm 0.06$	$3.28 \pm 0.06$	$1.38 \pm 0.01$	6
RXCJ2014.8-2430	0.15	0.0740	$4.78 \pm 0.05$	$5.38 \pm 0.07$	$5.64 \pm 0.02$	6
RXCJ2023.0-2056	0.06	0.0560	$2.71 \pm 0.09$	$1.21 \pm 0.03$	$0.26 \pm 0.00$	6
RXCJ2048.1-1750	0.15	0.0480	$4.65 \pm 0.10$	$4.32 \pm 0.07$	$1.79 \pm 0.01$	6
RXCJ2129.8-5048	0.08	0.0230	$3.81 \pm 0.15$	$2.26 \pm 0.06$	$0.56 \pm 0.01$	6
RXCJ2149.1-3041	0.12	0.0350	$3.26 \pm 0.04$	$2.25 \pm 0.03$	$1.36 \pm 0.01$	6
RXCJ2157.4-0747	0.06	0.0300	$2.46 \pm 0.08$	$1.29 \pm 0.03$	$0.23 \pm 0.00$	6
RXCJ2217.7-3543	0.15	0.0110	$4.86 \pm 0.09$	$3.61 \pm 0.05$	$1.88 \pm 0.01$	6
RXCJ0211.4-4017	0.10	0.0140	$2.07 \pm 0.10$	$1.00 \pm 0.02$	$0.36 \pm 0.00$	6
RXCJ2319.6-7313	0.10	0.0190	$2.22 \pm 0.03$	$1.56 \pm 0.03$	$0.85 \pm 0.01$	6
RXCJ0225.1-2928	0.06	0.0170	$2.47 \pm 0.07$	$0.96 \pm 0.04$	$0.22 \pm 0.00$	6
RXCJ1516.5-0056	0.12	0.0550	$3.55 \pm 0.07$	$2.59 \pm 0.05$	$0.93 \pm 0.01$	6
RXCJ2234.5-3744	0.15	0.0120	$7.78 \pm 0.15$	$7.36 \pm 0.09$	$4.11 \pm 0.02$	6

Columns: (1) Cluster name; (2) z: Redshift; (3)  $N_{\text{H}}$ : hydrogen column density; (4) T: Temperatures obtain in different apertures in keV. Details given in Table 3.1; (5) M: Mass within  $r_{500}$  in  $10^{14} M_{\odot}$ ; (6) L[0.5-2 keV]: 0.5-2 keV band luminosity in the  $r < r_{500}$  region in  $10^{44}$  erg/s; (7) References: 1-Zhang et al. (2008), 2-Zhang et al. (2006), 3-Snowden et al. (2008), 4-Arnaud et al. (2005), 5-Buote & Tsai (1996), 6-REXCESS: Pratt et al. (2009),  $M_{500}$ : Pratt et al. (2010).

Table 6.9: Power ratios and measurement errors obtained within  $r_{500}$  in the 0.5-2 keV energy range.

Cluster name (1)	P2/P0 (2)	error (3)	P3/P0 (4)	error (5)	P4/P0 (6)	error (7)
RXCJ0307.0-2840	$0.6145 \cdot 10^{-7}$	$0.8926 \cdot 10^{-7}$	$0.6036 \cdot 10^{-8}$	$0.1480 \cdot 10^{-7}$	$0.6383 \cdot 10^{-8}$	$0.9132 \cdot 10^{-8}$
RXCJ0516.7-5430	$0.2394 \cdot 10^{-4}$	$0.2687 \cdot 10^{-5}$	$0.6814 \cdot 10^{-6}$	$0.3088 \cdot 10^{-6}$	$0.1779 \cdot 10^{-6}$	$0.9129 \cdot 10^{-7}$
RXCJ0528.9-3927	$0.1381 \cdot 10^{-6}$	$0.1181 \cdot 10^{-6}$	$0.1836 \cdot 10^{-6}$	$0.8017 \cdot 10^{-7}$	$0.3947 \cdot 10^{-8}$	$0.7626 \cdot 10^{-8}$
RXCJ0532.9-3701	$0.1789 \cdot 10^{-5}$	$0.4430 \cdot 10^{-6}$	$0.8847 \cdot 10^{-7}$	$0.4919 \cdot 10^{-7}$	$0.1960 \cdot 10^{-7}$	$0.1565 \cdot 10^{-7}$
RXCJ0658.5-5556	$0.1890 \cdot 10^{-5}$	$0.2201 \cdot 10^{-5}$	$0.1599 \cdot 10^{-6}$	$0.3806 \cdot 10^{-7}$	$0.5636 \cdot 10^{-8}$	$0.6727 \cdot 10^{-8}$
RXCJ0945.4-0839	$0.2901 \cdot 10^{-5}$	$0.7066 \cdot 10^{-6}$	$0.1107 \cdot 10^{-6}$	$0.3390 \cdot 10^{-7}$	$0.3235 \cdot 10^{-6}$	$0.8916 \cdot 10^{-7}$
RXCJ2129.6+0005	$0.1634 \cdot 10^{-5}$	$0.1803 \cdot 10^{-6}$	$0.1448 \cdot 10^{-7}$	$0.7289 \cdot 10^{-8}$	$0.4111 \cdot 10^{-9}$	$0.1607 \cdot 10^{-8}$
RXCJ2308.3-0211	$0.8535 \cdot 10^{-6}$	$0.1303 \cdot 10^{-5}$	$0.3184 \cdot 10^{-6}$	$0.4369 \cdot 10^{-6}$	$0.3724 \cdot 10^{-6}$	$0.2041 \cdot 10^{-6}$
RXCJ2337.6+0016	$0.7995 \cdot 10^{-5}$	$0.1034 \cdot 10^{-5}$	$0.1336 \cdot 10^{-6}$	$0.6735 \cdot 10^{-7}$	$0.1126 \cdot 10^{-6}$	$0.4730 \cdot 10^{-7}$
A68	$0.2648 \cdot 10^{-5}$	$0.4101 \cdot 10^{-6}$	$0.1324 \cdot 10^{-6}$	$0.4811 \cdot 10^{-7}$	$0.6345 \cdot 10^{-7}$	$0.2283 \cdot 10^{-7}$
A115	$0.1128 \cdot 10^{-3}$	$0.2042 \cdot 10^{-5}$	$0.1707 \cdot 10^{-4}$	$0.4812 \cdot 10^{-6}$	$0.5287 \cdot 10^{-5}$	$0.1652 \cdot 10^{-6}$
A209	$0.3026 \cdot 10^{-5}$	$0.3539 \cdot 10^{-6}$	$0.8832 \cdot 10^{-7}$	$0.2771 \cdot 10^{-7}$	$0.3516 \cdot 10^{-7}$	$0.1308 \cdot 10^{-7}$
A267	$0.5198 \cdot 10^{-5}$	$0.6523 \cdot 10^{-6}$	$0.2169 \cdot 10^{-6}$	$0.7700 \cdot 10^{-7}$	$0.4051 \cdot 10^{-7}$	$0.2219 \cdot 10^{-7}$
A383	$0.2353 \cdot 10^{-6}$	$0.7072 \cdot 10^{-7}$	$0.1891 \cdot 10^{-7}$	$0.1021 \cdot 10^{-7}$	$0.1020 \cdot 10^{-7}$	$0.4798 \cdot 10^{-8}$
A773	$0.2711 \cdot 10^{-6}$	$0.1384 \cdot 10^{-6}$	$0.1133 \cdot 10^{-7}$	$0.2661 \cdot 10^{-7}$	$0.3850 \cdot 10^{-7}$	$0.4175 \cdot 10^{-7}$
A963	$0.4670 \cdot 10^{-7}$	$0.4219 \cdot 10^{-7}$	$0.1955 \cdot 10^{-7}$	$0.1487 \cdot 10^{-7}$	$0.6928 \cdot 10^{-8}$	$0.5711 \cdot 10^{-8}$
A1413	$0.1101 \cdot 10^{-5}$	$0.9295 \cdot 10^{-6}$	$0.3000 \cdot 10^{-6}$	$0.2616 \cdot 10^{-6}$	$0.1978 \cdot 10^{-6}$	$0.1844 \cdot 10^{-6}$
A1763	$0.1927 \cdot 10^{-4}$	$0.1570 \cdot 10^{-5}$	$0.4006 \cdot 10^{-6}$	$0.1212 \cdot 10^{-6}$	$0.1855 \cdot 10^{-6}$	$0.4126 \cdot 10^{-7}$
A1914	$0.5079 \cdot 10^{-7}$	$0.1930 \cdot 10^{-7}$	$0.3487 \cdot 10^{-7}$	$0.1096 \cdot 10^{-7}$	$0.5304 \cdot 10^{-8}$	$0.2084 \cdot 10^{-8}$
A2390	$0.1042 \cdot 10^{-5}$	$0.1881 \cdot 10^{-6}$	$0.5582 \cdot 10^{-7}$	$0.2127 \cdot 10^{-7}$	$0.8457 \cdot 10^{-8}$	$0.5383 \cdot 10^{-8}$
A2667	$0.3144 \cdot 10^{-6}$	$0.6123 \cdot 10^{-7}$	$0.2131 \cdot 10^{-8}$	$0.4059 \cdot 10^{-8}$	$0.5134 \cdot 10^{-8}$	$0.3021 \cdot 10^{-8}$
A2204	$0.1066 \cdot 10^{-6}$	$0.2570 \cdot 10^{-7}$	$0.1671 \cdot 10^{-7}$	$0.8980 \cdot 10^{-8}$	$0.1157 \cdot 10^{-9}$	$0.1613 \cdot 10^{-8}$
A2218	$0.5577 \cdot 10^{-5}$	$0.5132 \cdot 10^{-6}$	$0.1458 \cdot 10^{-6}$	$0.3978 \cdot 10^{-7}$	$0.1075 \cdot 10^{-7}$	$0.7624 \cdot 10^{-8}$
RXCJ0232.2-4420	$0.5981 \cdot 10^{-7}$	$0.4986 \cdot 10^{-7}$	$0.3159 \cdot 10^{-6}$	$0.7292 \cdot 10^{-7}$	$0.3774 \cdot 10^{-7}$	$0.1474 \cdot 10^{-7}$
A13	$0.8963 \cdot 10^{-6}$	$0.1689 \cdot 10^{-6}$	$0.3123 \cdot 10^{-6}$	$0.6576 \cdot 10^{-7}$	$0.4111 \cdot 10^{-7}$	$0.1477 \cdot 10^{-7}$
A520	$0.4637 \cdot 10^{-6}$	$0.6405 \cdot 10^{-6}$	$0.1654 \cdot 10^{-6}$	$0.4669 \cdot 10^{-7}$	$0.6451 \cdot 10^{-7}$	$0.6054 \cdot 10^{-8}$
A665	$0.1515 \cdot 10^{-5}$	$0.2971 \cdot 10^{-6}$	$0.2269 \cdot 10^{-6}$	$0.6320 \cdot 10^{-7}$	$0.6295 \cdot 10^{-7}$	$0.2347 \cdot 10^{-7}$
A1068	$0.1447 \cdot 10^{-5}$	$0.1145 \cdot 10^{-6}$	$0.1374 \cdot 10^{-7}$	$0.1026 \cdot 10^{-7}$	$0.4778 \cdot 10^{-8}$	$0.4340 \cdot 10^{-8}$
A1589	$0.4796 \cdot 10^{-5}$	$0.6570 \cdot 10^{-6}$	$0.7087 \cdot 10^{-7}$	$0.3738 \cdot 10^{-7}$	$0.2556 \cdot 10^{-7}$	$0.1921 \cdot 10^{-7}$
A2163	$0.4456 \cdot 10^{-6}$	$0.8115 \cdot 10^{-7}$	$0.1772 \cdot 10^{-6}$	$0.3235 \cdot 10^{-7}$	$0.1394 \cdot 10^{-6}$	$0.2790 \cdot 10^{-7}$
A2717	$0.1093 \cdot 10^{-6}$	$0.5544 \cdot 10^{-7}$	$0.7050 \cdot 10^{-7}$	$0.2747 \cdot 10^{-7}$	$0.8705 \cdot 10^{-7}$	$0.1964 \cdot 10^{-7}$
A3112	$0.1150 \cdot 10^{-5}$	$0.6965 \cdot 10^{-7}$	$0.1720 \cdot 10^{-6}$	$0.2039 \cdot 10^{-7}$	$0.4188 \cdot 10^{-7}$	$0.7845 \cdot 10^{-8}$
A3827	$0.5885 \cdot 10^{-7}$	$0.6635 \cdot 10^{-7}$	$0.8003 \cdot 10^{-7}$	$0.1932 \cdot 10^{-7}$	$0.2133 \cdot 10^{-8}$	$0.4763 \cdot 10^{-8}$
A3911	$0.8550 \cdot 10^{-5}$	$0.6097 \cdot 10^{-6}$	$0.2396 \cdot 10^{-6}$	$0.6675 \cdot 10^{-7}$	$0.1883 \cdot 10^{-7}$	$0.1891 \cdot 10^{-7}$
A3921	$0.2068 \cdot 10^{-4}$	$0.9847 \cdot 10^{-6}$	$0.1417 \cdot 10^{-5}$	$0.1538 \cdot 10^{-6}$	$0.3798 \cdot 10^{-6}$	$0.4064 \cdot 10^{-7}$
E1455+2232	$0.5572 \cdot 10^{-6}$	$0.1012 \cdot 10^{-6}$	$0.3906 \cdot 10^{-7}$	$0.1217 \cdot 10^{-7}$	$0.7546 \cdot 10^{-9}$	$0.1345 \cdot 10^{-8}$
PKS0745-19	$0.2194 \cdot 10^{-6}$	$0.2949 \cdot 10^{-7}$	$0.1290 \cdot 10^{-8}$	$0.6555 \cdot 10^{-8}$	$0.5761 \cdot 10^{-8}$	$0.6128 \cdot 10^{-8}$
RXJ1347-1145	$0.4420 \cdot 10^{-6}$	$0.6960 \cdot 10^{-7}$	$0.1701 \cdot 10^{-7}$	$0.7071 \cdot 10^{-8}$	$0.9350 \cdot 10^{-9}$	$0.1260 \cdot 10^{-8}$
Sersic159-3	$0.3876 \cdot 10^{-6}$	$0.1817 \cdot 10^{-7}$	$0.3107 \cdot 10^{-8}$	$0.8507 \cdot 10^{-9}$	$0.4818 \cdot 10^{-9}$	$0.4417 \cdot 10^{-9}$
ZW3146	$0.8425 \cdot 10^{-7}$	$0.1249 \cdot 10^{-7}$	$0.9456 \cdot 10^{-8}$	$0.2092 \cdot 10^{-8}$	$0.3035 \cdot 10^{-9}$	$0.7362 \cdot 10^{-9}$
A2597	$0.5043 \cdot 10^{-6}$	$0.1000 \cdot 10^{-6}$	$0.1453 \cdot 10^{-7}$	$0.1052 \cdot 10^{-7}$	$0.8776 \cdot 10^{-9}$	$0.1344 \cdot 10^{-8}$
A1775	$0.7149 \cdot 10^{-8}$	$0.3537 \cdot 10^{-7}$	$0.2016 \cdot 10^{-6}$	$0.3830 \cdot 10^{-7}$	$0.1990 \cdot 10^{-7}$	$0.1191 \cdot 10^{-7}$
A1837	$0.7957 \cdot 10^{-5}$	$0.4573 \cdot 10^{-6}$	$0.1469 \cdot 10^{-6}$	$0.3836 \cdot 10^{-7}$	$0.8695 \cdot 10^{-7}$	$0.1788 \cdot 10^{-7}$
RXCJ0014.3-3022	$0.5104 \cdot 10^{-5}$	$0.8083 \cdot 10^{-6}$	$0.1116 \cdot 10^{-5}$	$0.1784 \cdot 10^{-6}$	$0.1103 \cdot 10^{-7}$	$0.2577 \cdot 10^{-7}$
RXCJ1131.9-1955	$0.1029 \cdot 10^{-4}$	$0.1047 \cdot 10^{-5}$	$0.9780 \cdot 10^{-6}$	$0.1954 \cdot 10^{-6}$	$0.3572 \cdot 10^{-8}$	$0.1305 \cdot 10^{-7}$
A1651	$0.1002 \cdot 10^{-5}$	$0.1807 \cdot 10^{-6}$	$0.1141 \cdot 10^{-7}$	$0.1330 \cdot 10^{-7}$	$0.2832 \cdot 10^{-7}$	$0.5416 \cdot 10^{-8}$

Columns: (1) Cluster name; (2)-(3) P2/P0 and measurement error; (4)-(5) P3/P0 and measurement error; (6)-(7) P4/P0 and measurement error

Table 6.9: continued.

Cluster name (1)	P2/P0 (2)	error (3)	P3/P0 (4)	error (5)	P4/P0 (6)	error (7)
A133	$0.2426 \cdot 10^{-5}$	$0.2462 \cdot 10^{-6}$	$0.2472 \cdot 10^{-7}$	$0.1488 \cdot 10^{-7}$	$0.2136 \cdot 10^{-7}$	$0.1136 \cdot 10^{-7}$
A2626	$0.1544 \cdot 10^{-5}$	$0.1257 \cdot 10^{-6}$	$0.1503 \cdot 10^{-8}$	$0.3926 \cdot 10^{-8}$	$0.2475 \cdot 10^{-8}$	$0.4116 \cdot 10^{-8}$
A2065	$0.6053 \cdot 10^{-5}$	$0.3171 \cdot 10^{-6}$	$0.1254 \cdot 10^{-6}$	$0.2895 \cdot 10^{-7}$	$0.8241 \cdot 10^{-8}$	$0.3494 \cdot 10^{-8}$
A1689	$0.3742 \cdot 10^{-6}$	$0.4224 \cdot 10^{-7}$	$0.7819 \cdot 10^{-8}$	$0.3127 \cdot 10^{-8}$	$0.4294 \cdot 10^{-12}$	$0.3279 \cdot 10^{-9}$
RXCJ0547.6-3152	$0.1245 \cdot 10^{-5}$	$0.2378 \cdot 10^{-6}$	$0.1300 \cdot 10^{-6}$	$0.5295 \cdot 10^{-7}$	$0.7861 \cdot 10^{-7}$	$0.2840 \cdot 10^{-7}$
RXCJ0645.4-5413	$0.2006 \cdot 10^{-5}$	$0.3074 \cdot 10^{-6}$	$0.1425 \cdot 10^{-7}$	$0.1762 \cdot 10^{-7}$	$0.2241 \cdot 10^{-7}$	$0.1076 \cdot 10^{-7}$
RXCJ0958.3-1103	$0.3603 \cdot 10^{-5}$	$0.4182 \cdot 10^{-6}$	$0.2730 \cdot 10^{-7}$	$0.2126 \cdot 10^{-7}$	$0.1311 \cdot 10^{-8}$	$0.5755 \cdot 10^{-8}$
RXCJ2218.6-3853	$0.6079 \cdot 10^{-5}$	$0.4248 \cdot 10^{-6}$	$0.2107 \cdot 10^{-6}$	$0.4880 \cdot 10^{-7}$	$0.9879 \cdot 10^{-8}$	$0.6205 \cdot 10^{-8}$
RXCJ0003.8+0203	$0.1976 \cdot 10^{-5}$	$0.3736 \cdot 10^{-6}$	$0.2115 \cdot 10^{-7}$	$0.2345 \cdot 10^{-7}$	$0.3840 \cdot 10^{-7}$	$0.2131 \cdot 10^{-7}$
RXCJ0006.0-3443	$0.5027 \cdot 10^{-5}$	$0.1161 \cdot 10^{-5}$	$0.7611 \cdot 10^{-6}$	$0.2563 \cdot 10^{-6}$	$0.1512 \cdot 10^{-6}$	$0.9354 \cdot 10^{-7}$
RXCJ0020.7-2542	$0.1234 \cdot 10^{-5}$	$0.4301 \cdot 10^{-6}$	$0.1004 \cdot 10^{-7}$	$0.2721 \cdot 10^{-7}$	$0.2034 \cdot 10^{-7}$	$0.1120 \cdot 10^{-7}$
RXCJ0049.4-2931	$0.1289 \cdot 10^{-5}$	$0.4979 \cdot 10^{-6}$	$0.6050 \cdot 10^{-7}$	$0.5517 \cdot 10^{-7}$	$0.1100 \cdot 10^{-6}$	$0.5425 \cdot 10^{-7}$
RXCJ0145.0-5300	$0.1021 \cdot 10^{-4}$	$0.2295 \cdot 10^{-5}$	$0.1939 \cdot 10^{-6}$	$0.2042 \cdot 10^{-6}$	$0.1260 \cdot 10^{-6}$	$0.9044 \cdot 10^{-7}$
RXCJ0345.7-4112	$0.2062 \cdot 10^{-5}$	$0.3758 \cdot 10^{-6}$	$0.3217 \cdot 10^{-6}$	$0.9766 \cdot 10^{-7}$	$0.1357 \cdot 10^{-6}$	$0.4489 \cdot 10^{-7}$
RXCJ0605.8-3518	$0.9422 \cdot 10^{-6}$	$0.1171 \cdot 10^{-6}$	$0.7733 \cdot 10^{-8}$	$0.3782 \cdot 10^{-8}$	$0.1051 \cdot 10^{-7}$	$0.3086 \cdot 10^{-8}$
RXCJ0616.8-4748	$0.1233 \cdot 10^{-4}$	$0.2090 \cdot 10^{-5}$	$0.2412 \cdot 10^{-6}$	$0.1720 \cdot 10^{-6}$	$0.3713 \cdot 10^{-6}$	$0.1350 \cdot 10^{-6}$
RXCJ0821.8+0112	$0.6504 \cdot 10^{-6}$	$0.8990 \cdot 10^{-6}$	$0.1827 \cdot 10^{-6}$	$0.3307 \cdot 10^{-6}$	$0.6579 \cdot 10^{-6}$	$0.3797 \cdot 10^{-6}$
RXCJ1044.5-0704	$0.1319 \cdot 10^{-5}$	$0.1209 \cdot 10^{-6}$	$0.1506 \cdot 10^{-8}$	$0.1740 \cdot 10^{-8}$	$0.1272 \cdot 10^{-8}$	$0.2223 \cdot 10^{-8}$
RXCJ1141.4-1216	$0.6280 \cdot 10^{-6}$	$0.1136 \cdot 10^{-6}$	$0.2285 \cdot 10^{-7}$	$0.1525 \cdot 10^{-7}$	$0.9072 \cdot 10^{-8}$	$0.5169 \cdot 10^{-8}$
RXCJ1236.7-3354	$0.5018 \cdot 10^{-6}$	$0.3450 \cdot 10^{-6}$	$0.6252 \cdot 10^{-7}$	$0.9577 \cdot 10^{-7}$	$0.5175 \cdot 10^{-7}$	$0.6451 \cdot 10^{-7}$
RXCJ1302.8-0230	$0.6828 \cdot 10^{-5}$	$0.7773 \cdot 10^{-6}$	$0.1362 \cdot 10^{-6}$	$0.5633 \cdot 10^{-7}$	$0.1077 \cdot 10^{-6}$	$0.3836 \cdot 10^{-7}$
RXCJ1516.3+0005	$0.7745 \cdot 10^{-6}$	$0.2118 \cdot 10^{-6}$	$0.1702 \cdot 10^{-7}$	$0.1802 \cdot 10^{-7}$	$0.7079 \cdot 10^{-7}$	$0.2254 \cdot 10^{-7}$
RXCJ2014.8-2430	$0.4701 \cdot 10^{-6}$	$0.7397 \cdot 10^{-7}$	$0.2355 \cdot 10^{-7}$	$0.8520 \cdot 10^{-8}$	$0.5997 \cdot 10^{-8}$	$0.3078 \cdot 10^{-8}$
RXCJ2023.0-2056	$0.6398 \cdot 10^{-6}$	$0.3890 \cdot 10^{-6}$	$0.3474 \cdot 10^{-7}$	$0.5537 \cdot 10^{-7}$	$0.1348 \cdot 10^{-6}$	$0.6996 \cdot 10^{-7}$
RXCJ2048.1-1750	$0.8719 \cdot 10^{-5}$	$0.9179 \cdot 10^{-6}$	$0.5244 \cdot 10^{-6}$	$0.8862 \cdot 10^{-7}$	$0.1947 \cdot 10^{-6}$	$0.3289 \cdot 10^{-7}$
RXCJ2129.8-5048	$0.3529 \cdot 10^{-5}$	$0.4741 \cdot 10^{-6}$	$0.5361 \cdot 10^{-6}$	$0.1087 \cdot 10^{-6}$	$0.1144 \cdot 10^{-6}$	$0.2583 \cdot 10^{-7}$
RXCJ2149.1-3041	$0.9040 \cdot 10^{-7}$	$0.8902 \cdot 10^{-7}$	$0.1035 \cdot 10^{-6}$	$0.3323 \cdot 10^{-7}$	$0.1843 \cdot 10^{-7}$	$0.2330 \cdot 10^{-7}$
RXCJ2157.4-0747	$0.1218 \cdot 10^{-3}$	$0.4536 \cdot 10^{-4}$	$0.2449 \cdot 10^{-4}$	$0.6048 \cdot 10^{-5}$	$0.7446 \cdot 10^{-5}$	$0.1783 \cdot 10^{-5}$
RXCJ2217.7-3543	$0.4762 \cdot 10^{-6}$	$0.1835 \cdot 10^{-6}$	$0.8091 \cdot 10^{-7}$	$0.3103 \cdot 10^{-7}$	$0.1746 \cdot 10^{-7}$	$0.1225 \cdot 10^{-7}$
RXCJ0211.4-4017	$0.3094 \cdot 10^{-5}$	$0.5583 \cdot 10^{-6}$	$0.5516 \cdot 10^{-7}$	$0.4631 \cdot 10^{-7}$	$0.2102 \cdot 10^{-6}$	$0.6095 \cdot 10^{-7}$
RXCJ2319.6-7313	$0.5067 \cdot 10^{-5}$	$0.7104 \cdot 10^{-6}$	$0.1155 \cdot 10^{-7}$	$0.2509 \cdot 10^{-7}$	$0.2329 \cdot 10^{-7}$	$0.1517 \cdot 10^{-7}$
RXCJ0225.1-2928	$0.4277 \cdot 10^{-5}$	$0.9149 \cdot 10^{-6}$	$0.2263 \cdot 10^{-6}$	$0.1520 \cdot 10^{-6}$	$0.4233 \cdot 10^{-7}$	$0.3928 \cdot 10^{-7}$
RXCJ1516.5-0056	$0.5191 \cdot 10^{-5}$	$0.8135 \cdot 10^{-6}$	$0.9157 \cdot 10^{-6}$	$0.1800 \cdot 10^{-6}$	$0.1351 \cdot 10^{-6}$	$0.5450 \cdot 10^{-7}$
RXCJ2234.5-3744	$0.1955 \cdot 10^{-5}$	$0.1613 \cdot 10^{-6}$	$0.3195 \cdot 10^{-7}$	$0.1352 \cdot 10^{-7}$	$0.2111 \cdot 10^{-7}$	$0.5612 \cdot 10^{-8}$

Columns: (1) Cluster name; (2)-(3) P2/P0 and measurement error; (4)-(5) P3/P0 and measurement error; (6)-(7) P4/P0 and measurement error



Table 6.10: Morphological classification for 80 clusters by eye and using the classification scheme of Buote (2002).

Cluster name (1)	Disturbed (2)	Morphologies (3)
RXCJ0307.0-2840	undisturbed	1
RXCJ0516.7-5430	undisturbed	1
RXCJ0528.9-3927	undisturbed	1
RXCJ0532.9-3701	undisturbed	1
RXCJ0658.5-5556	disturbed	2
RXCJ0945.4-0839	undisturbed	1
RXCJ2129.6+0005	undisturbed	1
RXCJ2308.3-0211	undisturbed	1
RXCJ2337.6+0016	disturbed	3
A68	undisturbed	1
A115	disturbed	2
A209	undisturbed	1
A267	undisturbed	1
A383	undisturbed	1
A773	undisturbed	1
A963	undisturbed	1
A1413	undisturbed	1
A1763	undisturbed	1
A1914	undisturbed	1
A2390	undisturbed	1
A2667	undisturbed	1
A2204	undisturbed	1
A2218	undisturbed	1
RXCJ0232.2-4420	undisturbed	3
A13	undisturbed	1
A520	disturbed	4
A665	undisturbed	3
A1068	undisturbed	1
A1589	undisturbed	1
A2163	disturbed	3
A2717	undisturbed	1
A3112	undisturbed	1
A3827	undisturbed	1
A3911	undisturbed	1
A3921	disturbed	3
E1455+2232	undisturbed	1
PKS0745-19	undisturbed	1
RXJ1347-1145	undisturbed	1
Sersic159-3	undisturbed	1
ZW3146	undisturbed	1
A2597	undisturbed	1
A1775	disturbed	3
A1837	undisturbed	1
RXCJ0014.3-3022	disturbed	3
RXCJ1131.9-1955	disturbed	3
A1651	undisturbed	1

Columns: (1) Cluster name; (2) Classification by eye: disturbed (substructure visible) and undisturbed clusters (no visible substructure); (3) Classification using the classification scheme of Buote (2002): 1 single, 2 double, 3 complex, 4 primary with small secondary.

Table 6.10: continued.

Cluster name (1)	Disturbed (2)	Morphologies (3)
A133	undisturbed	1
A2626	undisturbed	1
A2065	undisturbed	1
A1689	undisturbed	1
RXCJ0547.6-3152	undisturbed	1
RXCJ0645.4-5413	undisturbed	1
RXCJ0958.3-1103	undisturbed	1
RXCJ2218.6-3853	undisturbed	1
RXCJ0003.8+0203	undisturbed	1
RXCJ0006.0-3443	undisturbed	1
RXCJ0020.7-2542	undisturbed	1
RXCJ0049.4-2931	undisturbed	1
RXCJ0145.0-5300	undisturbed	1
RXCJ0345.7-4112	undisturbed	1
RXCJ0605.8-3518	undisturbed	1
RXCJ0616.8-4748	undisturbed	1
RXCJ0821.8+0112	disturbed	4
RXCJ1044.5-0704	undisturbed	1
RXCJ1141.4-1216	undisturbed	1
RXCJ1236.7-3354	undisturbed	1
RXCJ1302.8-0230	undisturbed	1
RXCJ1516.3+0005	undisturbed	1
RXCJ2014.8-2430	undisturbed	1
RXCJ2023.0-2056	undisturbed	1
RXCJ2048.1-1750	undisturbed	1
RXCJ2129.8-5048	disturbed	3
RXCJ2149.1-3041	undisturbed	1
RXCJ2157.4-0747	disturbed	3
RXCJ2217.7-3543	undisturbed	1
RXCJ0211.4-4017	undisturbed	1
RXCJ2319.6-7313	undisturbed	1
RXCJ0225.1-2928	undisturbed	1
RXCJ1516.5-0056	undisturbed	3
RXCJ2234.5-3744	undisturbed	1

Columns: (1) Cluster name; (2) Classification by eye: disturbed (substructure visible) and undisturbed clusters (no visible substructure); (3) Classification using the classification scheme of Buote (2002): 1 single, 2 double, 3 complex, 4 primary with small secondary.

# Abstract

Clusters of galaxies are the largest known gravitationally bound objects in the Universe. Therefore, they are key laboratories to study properties of the Universe. The cluster mass is dominated by dark matter, while most of the baryons reside in a hot, fully ionized plasma, the intracluster medium (ICM), which can be observed through thermal bremsstrahlung emission in X-rays. The main assumptions made to estimate the cluster mass are hydrostatic equilibrium and spherical shape. However, observations reveal that hydrostatic equilibrium is often violated (due to merging, AGN-ICM interaction etc.) and that galaxy clusters deviate from a spherical shape. To quantify substructure in a cluster is therefore very important in order to estimate the deviation from the hydrostatic equilibrium and to produce realistic mass estimates.

We perform structural analysis of 80 clusters of galaxies taken from different surveys, including the most representative REXCESS sample. The employed method are power ratios as introduced in Buote & Tsai (1995). This method quantifies substructure in the ICM and thus provides a measure of the clusters' deviation from the hydrostatic equilibrium. Like Buote & Tsai (1996), we test the correlation between different power ratios. One goal of this project is to analyse this sample in detail and to investigate whether there are any physical correlations between the amount of substructure and cluster properties like luminosity, temperature or mass. We do not find any relations between the structure measure  $P3/P0$  and any cluster parameter, which is in good agreement with Böhringer et al. (2010). In addition, we test the L-T- and L-M-relation for relaxed and disturbed clusters (classified by eye, cool core properties and power ratios). We confirm the findings of previous studies (e.g. Fabian et al. 1994; Pratt et al. 2009) that cool-core (rather relaxed) clusters have in general higher luminosities at a given mass or temperature. The difference in the L-T- and L-M-relations however is within the errors and therefore not significant.

The main part of the thesis focuses on the power ratio method itself. This method is known for 15 years, but so far no fully consistent and tested estimate of the bias due to photon noise was presented. We therefore discuss and test the most promising method (proposed by Böhringer et al. 2010). In addition, we develop a method to simulate clusters and investigate the dependence of the method and the bias on different parameters like total counts, aperture size and absolute power ratio. We conclude that for low power ratios and low counts the obtained amount of structure photon noise modifies (mostly boosts) the power ratios. The reliability of this method increases with increasing amount of structure and increasing total counts. However, in its current state the method cannot be applied to high-redshift clusters because the effect of photon noise is too severe at such low counts. We thus introduce the use of the mean and  $\sigma$  of power ratios obtained in several aperture radii. This gives more reliable results than using a single aperture.



# Zusammenfassung

Galaxienhaufen sind die größten gravitativ gebundenen Systeme im Universum. Sie sind daher die besten Laboratorien, um die Zusammensetzung und Entwicklung des Universums zu studieren. Ihre Masse wird von Dunkler Materie dominiert, der Großteil der baryonischen Materie liegt in Form eines heißen Plasmas vor. Dieses heiße Gas wird Intracluster Medium (ICM) genannt und sendet aufgrund seiner hohen Temperatur thermische Bremsstrahlung aus, welche im Röntgenbereich beobachtet wird. Um die Haufenmasse zu bestimmen, werden hydrostatisches Gleichgewicht und Kugelform angenommen. Beobachtungen zeigen jedoch, dass sich viele Galaxienhaufen nicht im Gleichgewicht befinden und von der Kugelform abweichen (z.B. durch merging, AGN-ICM Wechselwirkungen). Die Bestimmung der Struktur in einem Haufen ist daher sehr wichtig, um die Abweichung vom hydrostatischen Gleichgewicht zu bestimmen und realistische Massenabschätzungen zu erhalten.

Im Zuge dieser Arbeit wird die Struktur von 80 Galaxienhaufen untersucht, die aus verschiedenen Surveys (z.B. REXCESS) stammen. Zur Strukturanalyse benutzen wir power ratios, die von Buote & Tsai (1995) eingeführt wurden. Diese Methode quantifiziert Substruktur im ICM und gibt ein Maß für die Abweichung vom hydrostatischen Gleichgewicht. Wie Buote & Tsai (1996) untersuchen wir den Zusammenhang zwischen verschiedenen power ratios. Ein Ziel dieser Arbeit ist die detaillierte Analyse des Samples und des physikalischen Zusammenhangs von power ratios und Haufenparametern (Leuchtkraft, Temperatur, Masse). Ebenso wie Böhringer et al. (2010) finden wir keine Beziehungen zwischen dem Strukturmaß  $P3/P0$  und Haufenparametern. Weiters untersuchen wir die L-T- und L-M-Relationen für relaxierte und gestörte Haufen (Klassifizierung per Auge, Cool core Eigenschaften und power ratios). Wir bestätigen die Resultate von früheren Studien (e.g. Fabian et al. 1994; Pratt et al. 2009), dass Cool-core (eher relaxierte) Haufen bei gleicher Masse und Temperatur höhere Leuchtkräfte aufweisen als gestörte Haufen. Die Unterschiede zwischen den L-T- und L-M-Relation sind auffällig, jedoch innerhalb der Fehlergrenzen und können daher nicht als signifikant angesehen werden.

Das Hauptaugenmerk dieser Arbeit liegt jedoch auf der power ratio Methode selbst. Diese Methode ist bereits seit 15 Jahren bekannt, bisher ist es aber noch niemandem gelungen das Photonrauschen (Bias) zu quantifizieren und einheitlich zu korrigieren. Wir diskutieren und testen deshalb die bis jetzt aussichtsreichste Methode, die von Böhringer et al. (2010) vorgeschlagen wurde. Weiters entwickeln wir eine Methode, um Haufen zu simulieren und um die Abhängigkeit der power ratios von Parametern wie counts, Aperturgröße und absolutem power ratio Wert zu untersuchen. Wir schlussfolgern, dass die gemessenen power ratios für niedrige power ratio Werte und niedrige counts durch Photonrauschen verfälscht werden. Die Zuverlässigkeit der Methode steigt jedoch mit mehr Struktur und mehr counts. In ihrem derzeitigen Zustand kann die power ratio Methode jedoch nicht bei hoch rotverschobenen Haufen angewendet werden, da die counts zu gering sind und daher das Photonrauschen zu stark ist. Wir schlagen deshalb vor, den

Mittelwert oder die Standardabweichung  $\sigma$  von power ratios, die in mehreren Aperturen berechnet werden, zu verwenden. Dies gibt zuverlässigere Resultate als die Benutzung einer einzelnen Apertur.

# Acknowledgements

I would like to say thank you to everybody who was involved in this thesis project for providing guidance, answering all of my questions and keeping up with my always changing and very tight schedule. A special thanks goes to my supervisor at the University of Vienna, Univ.-Prof. Gerhard Hensler, who always asked interesting questions and had an open ear whenever I was in Vienna. I want to express my gratitude towards Prof. Hans Böhringer, who invited me to stay at MPE for almost a year. He did not only provide a working space and the data I needed to finish my work but also a lot of knowledge and interesting ideas.

Robo, I really appreciated working with you. Thank you so much for guiding me through this project, for not getting annoyed by me and reading all the drafts I gave you. Without you this thesis would not have been possible. I also want to say thank you to my office mate, Gayoung. Thank you for all the interesting conversations and nice walks we had together and for showing me that it is fine to be lazy sometimes.

Martin, you know what I want to say to you. You kept me from freaking out whenever something was not going according to plan, you motivated me whenever I felt bad about my work and always made me smile. Thank you so much for your support during this year! Last but not least I want to thank my family for making this stay in Germany possible, both financially and emotionally. Thanks for taking care of Tara, Babs, without you this whole adventure would not have been possible.





# Alexandra Weißmann

---

Raimannstraße 3/51, A-1140 Vienna

Email: a.weissmann@gmx.at, Mobile: +43 6644315850

## Personal Data

Date of Birth: 26.08.1987

Place of Birth: Vienna, Austria

## Education

10/2009 - 05/2010

Master Thesis at Max-Planck Institute for extraterrestrial physics, Garching

Title: **Structural analysis of galaxy clusters in X-rays**

Supervisor: Univ.-Prof. Dr. Gerhard Hensler, in cooperation with Prof. Dr. Hans Böhringer (Max-Planck Institute for extraterrestrial physics, Garching bei München, Germany)

11/2008 - 07/2010 (expected)

**Master programme - Astronomy**, Institute of Astronomy, University of Vienna

Main topics:

- Extragalactic Astronomy
- Methods of Astronomy
- Computational Physics

11/2008

**Bakk. rer. nat.** in Astronomy, with honours

Title: **Structural analysis of clusters of galaxies with power ratios in X-Rays**

Supervisor: Univ.-Prof. Dr. Dieter Breitschwerdt, in cooperation with Prof. Dr. Hans Böhringer (Max-Planck Institute for extraterrestrial physics, Garching bei München, Germany)

10/2005 - 11/2008

**Bachelor programme - Astronomy**

Institute of Astronomy, University of Vienna

1997 - 2005

**Graduation:** June 2005, with honours

Privatgymnasium Friesgasse 4, A-1150 Vienna

## Scholarships and Awards

02/2009 and 02/2008

Performance Scholarship offered by the Federal Ministry (bm:bwk)

granted by University of Vienna for extraordinary achievements from 01.10.2007-30.09.2008 and 01.10.2006-30.09.2007 (respectively)

06/2008

Performance Scholarship offered by private institutions

granted by University of Vienna for extraordinary achievements from 01.1.2007-31.12.2007

03/2005

7th place in austrian-wide english competition

## Stays abroad for educational purposes

10/2009 - 05/2010

Visiting researcher for Master Thesis at Max-Planck Institute for extraterrestrial Physics, Garching bei München, Germany

02/2008 - 03/2008

Visiting researcher for Bachelor Thesis at Max-Planck Institute for extraterrestrial Physics, Garching bei München, Germany

04/2004

2-week Language course in Cambridge, UK

06/2003

1-week language course in Paris, France

## Teaching experiences

03/2009 - 06/2009

Teaching assistant for *Introduction to Astronomy 2*

10/2006 - 01/2007

Teaching assistant for *Introduction to Astronomy 1*

## Other activities

since 10/2009

Co-Organizer of IAYC (International Astronomical Youth Camp) 2010 in Germany (Working group leader)

08/2009, 07/08 2008, 07/08 2007 and 07/08 2006

Participant in IAYC (International Astronomical Youth Camp) in Poland, Czech Republic and Germany

09/2008

LOC (Local Organizing Committee) for JENAM 2008

University of Vienna

## Language Skills

German - native

English - fluent

French - good

Slovak - beginner

## Programming skills and languages

Linux, Windows XP, Windows Vista

Fortran77, Fortran 90/95, C++, IDL

LateX, gnuplot, Matlab, MS Office